

# On the Estimation of Bone Status

Rasmus Paulsen

June 30, 1998

# Preface

This thesis has been prepared at the Institute of Mathematical Modeling, Technical University of Denmark and at *Torsana Osteoporosis Diagnostics*.

The subject of this thesis is medical image analysis with special attention to X-ray images of the radius, performed on a set of female cadaveric specimens.

Lyngby, June 30, 1998

Rasmus Reinhold Paulsen

## Keywords

Osteoporosis, bone status, radius, contact radiographs, cortical geometry, endosteal resorption, image processing.

# Acknowledgements

I wish to thank the following people:

Assistant Professor Michael Grunkin, Professor Kaj Madsen and Associate Professor Bjarne Ersbøll, IMM,DTU for their valuable guidance through the project.

Anders Rosholm, Hans Henrik Thodberg, Lars Pedersen, Ulrik Olesen, Michael Edberg and Christian Lund at *Torsana* for their moral support, valuable comments, numerous interesting discussions and friendship.

Senior Registra, Dr. Med. Sci. Lars Hyldstrup, Department of Endokrinologi for his valuable comments and guidance through the medical society. Laboratory technician Lea Heine Jensen for helping me handling the bones. Radiographer Jens Søggaard for operating the x-ray machine and for his patience while I fumbled with the slices.

Associate professor Anni Vesterby and Laboratory technician Pernille Pedersen, Department of Forensic Medicine, University of Aarhus for helping me with the sectioning of the bones and for their moral support during the long hours in the autopsy room.

Associate Professor, M.D., Finn Boysen Møller, Department of Medical Anatomy, University of Copenhagen for supplying the bone material.

Charlotte Kjørup for her love and support.

# Summary

**Chapter 1** introduces the biological background and pathological framework relating to this thesis. The important concept of bone remodeling is introduced. A brief introduction to existing methods to assess bone quality is given.

**Chapter 2** gives a general view of the materials and methods used for producing contact radiographs of slices of the radius bone. The protocol explains how radius bones are sectioned and how digitized contact radiographs are acquired.

**Chapter 3** explains how the digitized contact radiographs are preprocessed. First a simple noise reduction method is explained. To separate the bone from the background a set of threshold methods have been implemented. In the resulting binary image it is necessary to locate the cortical shell, this is accomplished by a connected component algorithm. After that, the boundaries of the cortical shell is traced with a line tracing algorithm. In the next chapter the slices have to be aligned, therefore two alignment methods have been developed. One is a brute force general registration method, while the other is based on a shape description of the outer boundaries of the slices. The latter proves to be superior.

**Chapter 4** deals with the task of measuring geometric properties of the cortical shell. The cortical thickness and the area of the cortical shell is measured on the contact radiographs. The cortical thickness is measured by three different methods on the slices. The cortical thickness are also measured by a radiogrammetric algorithm developed by Torsana Osteoporosis Diagnostics. A *simulated* bone is made by simulated x-ray of the slices. The simulated bone is used as input to the radiogrammetry algorithm. Correlation between measured geometrical properties is examined. The bias between the cortical thickness measured on the slices and by radiogrammetry is tested for significance with a paired t-test.

**Chapter 5** explains developed methods of measuring the roughness of the inner boundary of the bone. Initially a method to generate a vector representation of the bone is explained. The vector representation is used to calculate a smoothness measure that describes the roughness of the boundary. A smooth approximation of the inner boundary is generated by a bandpass filtering of the polar coordinates of points on the boundary. By comparing the traced boundary and the approximated curve a set of smoothness measures have been generated. The scalloping measured by radiogrammetry is explained. Correlation between measured shape features is examined.

**Chapter 6** deals with measuring the area of endosteal resorption. The area where endosteal resorption is present is located by a set of active shape mod-

els. The outer boundary is located with an active net which is a simulated net used for locating and extraction of objects in images. The inner boundary is found with an active contour that inflates inside the medullary area. The inflation stops when the physical model reaches an equilibrium state. Correlation between measured shape features is examined.

**Kapitel 1** giver en introduktion til den biologiske og sygdomsmæssige baggrund for dette projekt. De knoglemæssige aspekter forklares, og der gives et overblik over eksisterende metoder til bestemmelse af knoglekvalitet.

**Kapitel 2** giver et overblik over datamaterialet. Den udviklede metode til fremstilling af kontakt-røntgenbilleder af knogleskiver forklares. Processen går fra at have ny udtagede knogler til at have digitaliserede røntgenbilleder.

**Kapitel 3** omhandler metoderne brugt til preprocessering af de digitaliserede røntgenbilleder. Først betragtes en simpel støjfjerningsmetode. For at separere knogle fra baggrund er forskellige *threshold* metoder udviklet. I det binære billede er det nødvendigt at udskille den kortikale skal af knoglen. Til det formål er der udviklet en såkaldt *connected component* algoritme, som kan arbejde med meget store billeder. Kanterne af den kortikale skal er derefter fundet ved en simpel kantfølge algoritme. For at kunne arbejde videre med skiverne, er det nødvendigt, at der ikke er en indbyrdes rotation. To metoder til at matche skivebilleder er udviklet, den ene er en meget generel registreringmetode. Den anden metode som er langt den bedste, er udviklet specielt til denne type billeder og baserer sig på et match af en formbeskrivelse af den ydre kant af skiverne.

**Kapitel 4** omhandler opmåling af geometriske egenskaber af den kortikale skal. Skaltykkelse og areal af skallen er målt på skiverne. Tre forskellige metoder er brugt til at måle skaltykkelsen på skiverne. Skaltykkelsen er også blevet målt på røntgenbillederne af radius knoglen ved hjælp af radiogrammetri algoritmerne udviklet på *Torsana Osteoporosis Diagnostics*. En simuleret knogle er konstrueret ved simuleret røntgen af knogleskiverne. Den simulerede knogle er blevet brugt som input til radiogrammetri modulet. Korrelationen mellem de målte værdier undersøges. Afvigelserne mellem den kortikale tykkelse målt på skiverne og ved radiogrammetri testes for signifikans ved parrede t-test.

**Kapitel 5** gennemgår en række metoder til opmåling af ujævnheden af den indre kant af knoglen. Først beskrives en metode til at generere en vektorrepræsentation af den fulgte indre kant. Vektorrepræsentation af den indre kant benyttes til at beregne et glathedsmål, der beskriver graden af fluktuationer af kanten. En glat approksimation af kanten er lavet ved hjælp af en Fourier transformation af de polære koordinater af punkter på den indre kant. Ved at sammenligne den fulgte kant med den glatte approksimation, kan et glathedsmål opnås. Korrelationen mellem de målte værdier undersøges.

**Kapitel 6** omhandler opmåling af arealet af området hvor der er endosteal resorption. Til at lokalisere de ydre og indre kanter af området er et sæt af aktive form modeller udviklet. Til at lokalisere de ydre kanter benyttes et aktivt net, som er et simuleret net der strammer sig omkring objekter i billeder. Til de indre kanter benyttes en aktiv kontur, som blæser sig op inden i knoglen, indtil den fysiske model er i ligevægt. Korrelationen mellem de målte værdier undersøges.

# Contents

<b>1</b>	<b>Introduction</b>	<b>2</b>
1.1	Osteoporosis . . . . .	2
1.2	The Skeleton . . . . .	2
1.2.1	The Radius . . . . .	3
1.3	Cortical Bone Remodelling . . . . .	3
1.3.1	The Bone Remodelling Unit . . . . .	4
1.3.2	Endosteal Resorption . . . . .	6
1.3.3	Periosteal Resorption . . . . .	7
1.3.4	Intracortical Resorption . . . . .	7
1.3.5	Trabeculization of the Endosteal Surface . . . . .	7
1.4	Methods for Quantitative Measure of Bone Quality . . . . .	7
1.4.1	Definition of Terms . . . . .	8
1.4.2	Radiogrammetry . . . . .	8
1.4.3	Radiographic Absorptiometry (RA) . . . . .	9
1.4.4	Single-Photon Absorptiometry (SPA) . . . . .	9
1.4.5	Dual Photon Absorptiometry (DPA) . . . . .	10
1.4.6	Dual X-ray Absorptiometry (DXA) . . . . .	10
1.4.7	Quantitative Computed Tomography (QCT) . . . . .	10
1.5	Motivation for the Study . . . . .	11
1.6	Previous Work . . . . .	11
1.7	Organization of the Study . . . . .	12
<b>2</b>	<b>Materials and Methods</b>	<b>14</b>
2.1	Cadaveric Data . . . . .	14
2.2	Panoramic Radiography . . . . .	14
2.2.1	Indication of Fix Point . . . . .	17

2.2.2	Perspective Distortion . . . . .	17
2.3	Sectioning of the Radius . . . . .	19
2.3.1	Materials and Methods . . . . .	19
2.3.2	Indication of Posterior and Distal Side . . . . .	19
2.3.3	Contact Radiographs . . . . .	21
2.3.4	Naming Convention used in the Analysis . . . . .	21
2.3.5	Placement of Slices when Radiograph is Taken . . . . .	21
2.3.6	Placement of Slices Relative to Fixpoint . . . . .	22
2.4	Digitizing of Radiographs . . . . .	22
<b>3</b>	<b>Preprocessing of Contact Radiographs</b>	<b>24</b>
3.1	Noise Reduction . . . . .	24
3.2	Thresholding . . . . .	24
3.2.1	Definition of Terms . . . . .	27
3.2.2	Iterative Optimal Threshold Selection . . . . .	27
3.2.3	Thresholds Based on a Global Objective Function . . . . .	28
3.2.4	Bimodal Histogram Thresholding, the Mode Method . . . . .	29
3.2.5	Results and Discussion . . . . .	29
3.3	Connected Component Labelling . . . . .	29
3.3.1	Creating a Connection Graph . . . . .	31
3.3.2	Determining Connected Components . . . . .	31
3.3.3	Results and Discussion . . . . .	31
3.4	Border Tracing . . . . .	34
3.4.1	Results and Discussion . . . . .	34
3.5	Alignment of Slices . . . . .	34
3.5.1	Polar Coordinate System of the Cortical Shell . . . . .	36
3.5.2	Global Optimization of Correlation using Steepest Descent . . . . .	36
3.5.3	Boundary Shape Representation Based Alignment . . . . .	39
3.5.4	Results and Discussion . . . . .	42
<b>4</b>	<b>Geometric Properties of the Cortical Shell</b>	<b>46</b>
4.1	Measuring the Geometric Properties of the Slices . . . . .	46
4.1.1	Cortical Thickness . . . . .	46
4.1.2	Cross-sectional Cortical Area . . . . .	51
4.2	Cortical Thickness Measured by Radiogrammetry . . . . .	55

4.3	Cortical Thickness Measured on a Simulated Radius . . . . .	55
4.4	Results and Discussion . . . . .	60
4.4.1	Cortical Geometry Measured on a Single Bone . . . . .	60
4.4.2	Comparison of the Cortical Geometry of all Bones . . . . .	65
<b>5</b>	<b>Measuring Endosteal Resorption</b>	<b>69</b>
5.1	Tracing the Endosteal Surface . . . . .	69
5.2	Polygonal Approximation . . . . .	70
5.2.1	A Suboptimal Line Fitting Algorithm . . . . .	70
5.2.2	A Simple Polygon Fitting Algorithm . . . . .	72
5.2.3	Results and Discussion . . . . .	72
5.3	Boundary Smoothness . . . . .	72
5.4	Bending Energy . . . . .	73
5.5	Boundary Fitting Using the Fast Fourier Transform . . . . .	74
5.5.1	Shape Features . . . . .	75
5.6	Results and Discussion . . . . .	76
5.6.1	Comparison of Shape Features from All Bones . . . . .	76
<b>6</b>	<b>Measuring the Endosteal Resorption Area</b>	<b>82</b>
6.1	Active Nets . . . . .	82
6.1.1	Matrix Representation . . . . .	82
6.1.2	Internal Energy . . . . .	83
6.1.3	External Energy . . . . .	84
6.1.4	Energy Minimization . . . . .	84
6.1.5	Results and Discussion . . . . .	85
6.2	Active Nets Used as a Balloon Model . . . . .	88
6.2.1	Spring Force and Inflation Force . . . . .	88
6.2.2	Internal Energy of the Balloon model . . . . .	88
6.2.3	Results and Discussion . . . . .	89
6.3	The Active Contour . . . . .	89
6.3.1	Vector Representation . . . . .	89
6.3.2	Spring Force and Inflation Force . . . . .	92
6.3.3	Internal Energy of the Contour . . . . .	92
6.3.4	External Energy of the Contour . . . . .	92
6.3.5	Energy Minimization . . . . .	93



6.3.6	Results and Discussion . . . . .	93
6.4	Calculating the Resorption Area . . . . .	93
6.5	Results and Discussion . . . . .	93
6.5.1	Comparison of Shape Features from All Bones . . . . .	93
<b>7</b>	<b>Conclusion</b>	<b>97</b>
<b>A</b>	<b>Photos</b>	<b>98</b>
<b>B</b>	<b>A Gallery of Slices</b>	<b>104</b>
<b>C</b>	<b>Graphs and Tables</b>	<b>122</b>
C.1	Cortical Thickness on a Single Bone . . . . .	122
C.1.1	Plots of cortical thickness . . . . .	122
C.1.2	Correlation between endpoint variables . . . . .	139
C.2	Comparison of features from all bones . . . . .	143
C.2.1	Correlation between endpoint variables . . . . .	143
C.2.2	Correlation plots . . . . .	148
<b>D</b>	<b>C++ image class library</b>	<b>160</b>
D.1	CImgLog . . . . .	160
D.1.1	Public member functions . . . . .	160
D.1.2	Example . . . . .	161
D.2	CImgExc . . . . .	162
D.2.1	Public member functions . . . . .	162
D.2.2	Public member variables . . . . .	162
D.2.3	Example . . . . .	162
D.3	CImgByte . . . . .	163
D.3.1	Public member functions . . . . .	163
D.3.2	Example . . . . .	164
D.4	CImgFloat . . . . .	165
D.4.1	Public member functions . . . . .	165
D.4.2	Example . . . . .	166
D.5	CImgInt . . . . .	167
D.5.1	Public member functions . . . . .	167
D.5.2	Example . . . . .	168

<b>E</b>	<b>Developed Software</b>	<b>169</b>
E.1	Thresholding . . . . .	170
	E.1.1 Source . . . . .	170
	E.1.2 Prototypes . . . . .	170
E.2	Connected Component Labeling . . . . .	171
	E.2.1 Source . . . . .	171
	E.2.2 Prototypes . . . . .	171
E.3	Boundary Tracing . . . . .	171
	E.3.1 Source . . . . .	171
	E.3.2 Prototypes . . . . .	172
	E.3.3 Point Class . . . . .	172
	E.3.4 Point Array Class . . . . .	173
E.4	Polygonal Approximation . . . . .	174
	E.4.1 Source . . . . .	174
	E.4.2 Prototypes . . . . .	174
E.5	Cubic Convolution . . . . .	174
	E.5.1 Source . . . . .	174
	E.5.2 Prototypes . . . . .	174
E.6	Alignment by Steepest Descent . . . . .	175
	E.6.1 Prototypes . . . . .	175
E.7	Alignment with Boundary Descriptions . . . . .	175
	E.7.1 Source . . . . .	175
	E.7.2 Prototypes . . . . .	175
E.8	Measuring Cortical Thickness . . . . .	175
	E.8.1 Source . . . . .	175
	E.8.2 Prototypes . . . . .	176
E.9	Simulated Radius . . . . .	176
	E.9.1 The Simulated Profile Class . . . . .	176
E.10	Boundary fitting by the Fast Fourier Transform . . . . .	179
	E.10.1 The Fourier Feature Class . . . . .	179
E.11	Active nets, Balloons and Contours . . . . .	182
	E.11.1 The Active Net Class . . . . .	182
	E.11.2 The Active Balloon Class . . . . .	184
	E.11.3 The Active Contour Class . . . . .	185

# Chapter 1

## Introduction

### 1.1 Osteoporosis

Osteoporosis is a common problem among the elderly, and is associated with a high incidence of skeletal fractures. Especially women are predisposed for developing osteoporosis. In the United States and Northern Europe, the lifetime risk of getting a proximal femur-, vertebra-, or distal forearm fracture at the age of 50 years is 40 % in women and 13 % in men [15], [21].

Through life, women lose about 35 % of their cortical bone and 50 % of their cancellous bone, whereas men lose about two thirds of these amounts [15].

On Average, bone mass peaks at about age 30 to 35 and declines steadily thereafter. Loss of bone mass in women is accelerated after the menopause.

### 1.2 The Skeleton

The main constituent of the human skeletal system is bone tissue. Bone tissue consists of bone cells (osteoclasts, osteoblasts, osteocysts, and lining cells) and intercellular substance, which is a specialized connective tissue composed of collagen fibers and ground substance impregnated with mineral.

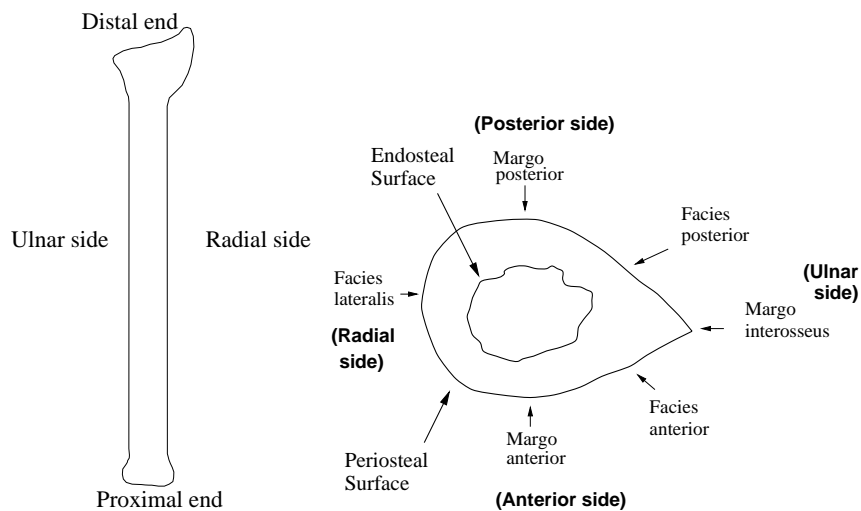
There are two different structural types of bone in the adult skeleton, cortical and trabecular. Cortical bone appears as a compact and dense bone usually with a porosity less than 10 %, whereas cancellous bone consist of a three dimensional lattice of branching trabeculae. About 80 % of total bone mass is cortical bone, this is mainly found in the shafts of the long bones, but also constituting the outer wall of all other bones. The remaining 20 % of total bone mass is cancellous mainly localized in the axial skeleton [15]. It continues with the inner side of the cortex, and usually has a porosity of more than 75 %. In this thesis only the cortical shell of the radius bone is examined.

### 1.2.1 The Radius

In this thesis some anatomical terms are used for the different parts of the radius.

A radius bone has two ends, a proximal end which is close to the body and a distal end which is away from the body. In this thesis a slice of the radius is considered having four sides; the anterior side, the posterior side, the ulnar side and the radial side. The anatomically correct terms are seen in figure 1.1.

The inner surface of the bone is denoted the endosteal surface and the outer surface is denoted the periosteal surface.



(a) A Radius has two ends, a proximal end which is close to the body and a distal end which is away from the body. It has two sides, a radial side and an ulnar side, the ulnar side is the side of the bone which is connected to the ulna.

(b) A slice of a radius. The outer surface is the periosteal surface and the inner surface is the endosteal surface. The anatomical names of the edges and surfaces are shown. The names of the four sides used in this thesis is shown in braces.

Figure 1.1: The anatomical terms used in this thesis. This radius is from a left hand seen with the palm facing downward.

## 1.3 Cortical Bone Remodelling

Throughout life old bone is continuously being renewed by new bone, a process called remodelling. This process occurs in anatomically discrete foci. The specialized groups of cells which accomplish one quantum of bone turnover is called a *bone remodelling unit* [15]. In this section the different types of cortical

resorption are explained. The expected manifestation of the types of resorption on a contact radiograph are seen on figure 1.2. The phenomena are seen on a slice of the radius in figure 1.3. The decrease in cortical bone is the result of two processes: cortical thinning and an increase in cortical porosity. Porosity increases due to a variety of age-related changes, including an increase in haversian canal diameter [19]. Cortical thinning is a product of endosteal resorption while porosity is a product of intracortical resorption. The outer diameter of many tubular bones increases with age but the medullary width increases faster than the outer diameter resulting in decreasing cortical thickness [26].

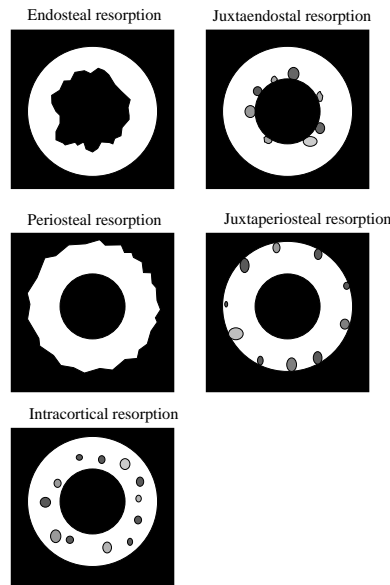


Figure 1.2: Expected manifestation of endosteal, juxtaendosteal, periosteal, juxta-periosteal and intracortical resorption on a contact radiograph of a slice of bone.

### 1.3.1 The Bone Remodelling Unit

A bone remodelling unit consists of osteoclasts (cutting cones) and osteoblasts (closing cones). The osteoclasts eat through the bone in the longitudinal direction. This is called the resorptive phase and lasts about a month where approximately  $0.1 \text{ mm}^3$  bone is removed. After the resorptive phase comes a period of about four months where the osteoblasts form new bone in the resorption cavity. A resorption space is a cavity about  $200\text{-}400 \mu\text{m}$  in diameter and with a length usually from 1 to 2 mm [25], [29]. In one end of the resorption space is a cluster of osteoclasts drilling in the direction of the long axis of the bone. Behind the osteoclasts the tunnel is filled with connective tissue and blood vessels. In the opposite end of the cavity is the osteoblasts which form new bone by producing osteoid. The space is not closed perfectly and ends as a haversian canal after the remodelling [29], [15]. In conditions of high bone turnover, there exists an increased number of resorptive spaces. This is a result of the balance between

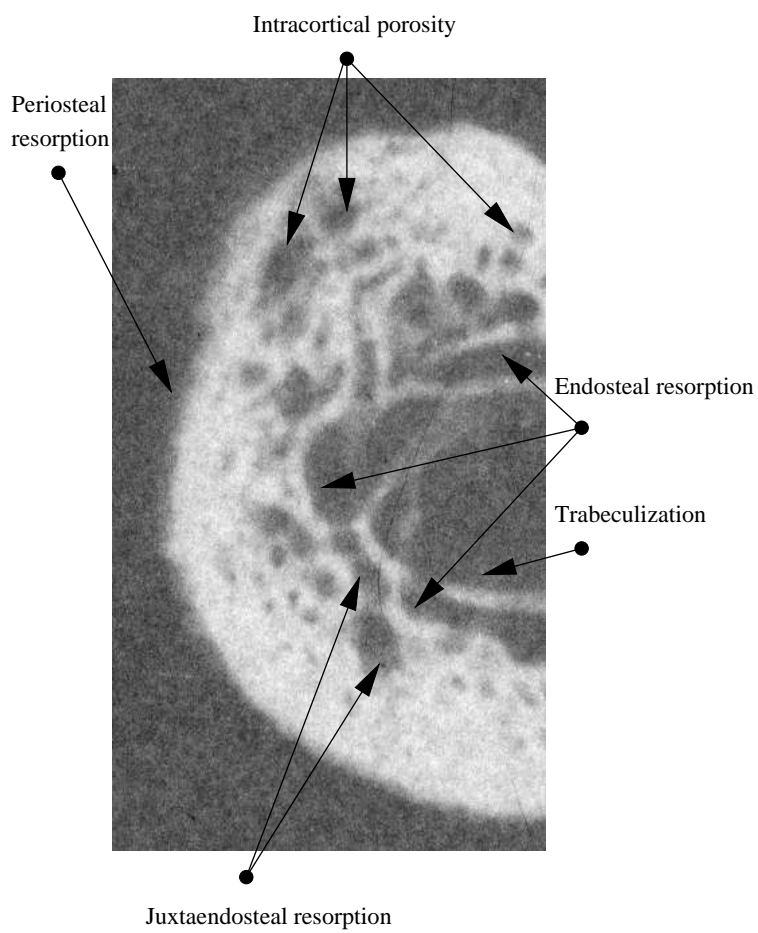


Figure 1.3: The different phenomena influencing the shape of a slice of bone.

osteoclastic resorption and osteoblastic formation. On figure 1.4 the dimension of an active bone remodelling unit is seen.

It is estimated that, in the mature adult, approximately 25 % of cancellous bone and about 3 % of cortical bone is renewed annually [19]. In the mature skeleton, about 2 % of cortical bone volume is occupied by Haversian canals [29].

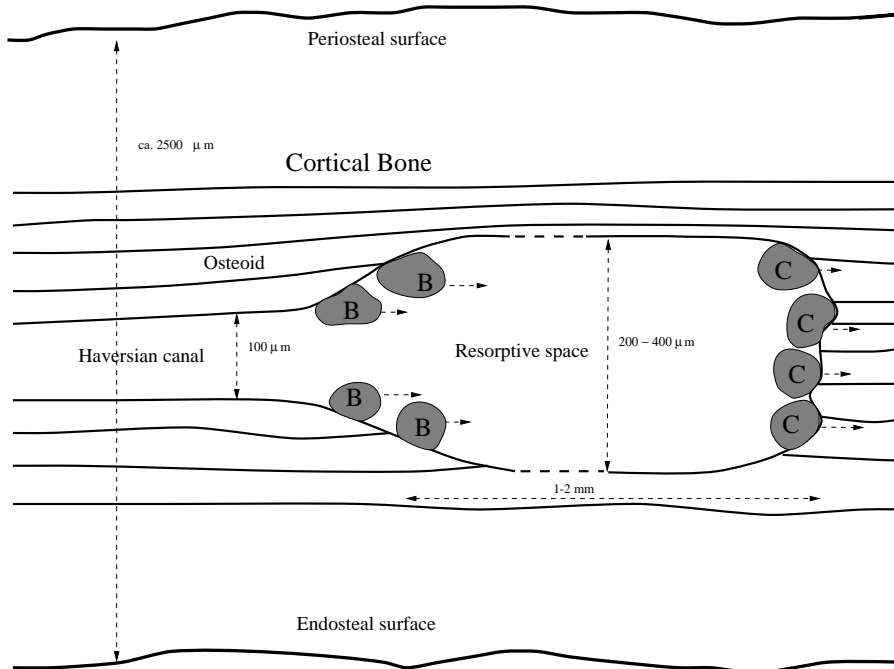


Figure 1.4: The dimensions of a bone remodelling unit. Osteoblasts are marked with **B** and osteoclasts with a **C**.

### 1.3.2 Endosteal Resorption

Endosteal resorption is the most important factor in the development of post-menopausal osteoporosis [25]. Endosteal resorption causes thinning of the cortices from the inside while the outer diameter remains nearly constant. Unlike the periosteal surface the endosteal surface is not always sharply defined because of the roughness caused by endosteal resorption. For a healthy patient under  $\approx 35$  years of age there is no endosteal bone loss. After the age of 50 endosteal bone loss is normal, but more rapid for osteoporotic patients.

#### Juxtaendosteal Resorption

Juxtaendosteal resorption is defined as intracortical resorption spaces near the endosteal surface. If there is a communication between a juxtaendosteal resorption space and the medullary area, the juxtaendosteal resorption space is normally considered as a part of the medullary area [24].

### 1.3.3 Periosteal Resorption

Periosteal and juxtaperiosteal resorption when present are characteristic of hyperparathyroidism [22],[25]. Periosteal resorption has been examined by microradioscopy of the phalanges by meema [25]. There are two manifestations of periosteal resorption. 1) a fuzziness of the periosteal surface. 2) Resorptive cavities close to the periosteal surface, also called juxtaperiosteal resorption. Meema introduces a grading system from 0 to 3+ for periosteal resorption. Grade 0 is when the periosteal surface of the middle phalanges is smooth and grade 3+ is where bones, other than the phalanges, show evidence of periosteal resorption [25]. Periosteal resorption is not examined further in this thesis.

### 1.3.4 Intracortical Resorption

Intracortical resorption is when there is an increment in size and number of intracortical resorption spaces. Intracortical resorption leads to intracortical porosity. Intracortical resorption has been investigated by use of microradioscopy of the second, third and fourth metacarpal midshaft [25]. A grading system for the severity of intracortical resorption exists. The grades vary from 0 (normal) to 3+ (marked striations of the entire cortex) [25].

The average length and width of the metacarpal and phalangeal intracortical resorption spaces (IRS) has been measured using a digitizing table at x8 magnification by Meema. Also the per cent metacarpal and phalangeal porosity was calculated. The results suffered from a very poor interobserver error (28-45 %) [24].

### 1.3.5 Trabeculization of the Endosteal Surface

A negative bone balance due to enhanced resorption depth on the endosteal surface results in progressive *cancellization* of the inner cortex. The resorption cavities near the endosteal surface increase in size due to osteoblastic insufficiency, and resorption cavities on the endosteal surface increase in depth due to excessive osteoclastic activity. Where there was once dense cortical bone, new trabeculae is created, allowing invasion of the marrow [19].

## 1.4 Methods for Quantitative Measure of Bone Quality

In this section different methods for assessment of bone mass are briefly reviewed. The bone mass is for the Bone Densitometric methods (RA, SPA, DPA, SXA, DXA) measured as the bone mineral density (BMD). A high correlation between bone mass and bone strength tested *in vitro* can be seen in bone tissue as well as whole bones [9].



### 1.4.1 Definition of Terms

#### Bone Mineral Content and Bone Mineral Density

The Bone Mineral Content (BMC) is the mineral content of a scanned bone (normally grams of calcium). Bone Mineral Density (BMD) is BMC divided by the scanned area (normally in  $cm^2$ ) [6].

$$\text{BMD} = \frac{\text{BMC}}{\text{Area}} \quad (1.1)$$

#### Accuracy, Precision and Sensitivity

*Accuracy* means the ability of the system to measure the same bone mineral content of an object as measured by another independent method. *Precision* reflects the ability of an instrument to reproduce the same results in repeated measurements. *Diagnostics sensitivity* refers to the capacity of a measurement to distinguish between normal and osteoporotic individuals and to measure age- and disease related bone loss [6].

### 1.4.2 Radiogrammetry

Radiogrammetry is the art of measuring the geometric properties of a bone on a radiograph.

Since the endosteal resorption is considered the main factor in osteoporosis, some radiogrammetric methods of measuring this, have been developed.

Measurements of the cortical width are commonly made at the second metacarpal and the radius. The place of measurement of the metacarpal is at the mid point of its length. On the radius the measurements are normally measured where the outer diameter is at minimum. The most widely used measurement is the combined cortical width [22],

$$\text{CCW} = D - d \quad (1.2)$$

or the metacarpal index (MCI),

$$\text{MCI} = \frac{D - d}{D} \quad (1.3)$$

, where  $D$  is the outer diameter and  $d$  is the medullary width.

On the (incorrect) assumption that the bones are tubular, the cortical area (CA) can be calculated by subtraction (eliminating  $\pi$ ),

$$\text{CA} = D^2 - d^2 \quad (1.4)$$

and may be expressed as a proportion of bone area, i.e. relative cortical area (RCA),

$$\text{RCA} = \frac{D^2 - d^2}{D^2} \quad (1.5)$$

The projection of a tubular bone on a radiograph is shown in figure 1.5. The values that can be directly measured are  $D$ ,  $d$  and the ulnar and radial cortical thickness  $d_1$  and  $d_2$ .

Radiogrammetry is an inexpensive and practical method for measuring an approximate value of the bone mass.

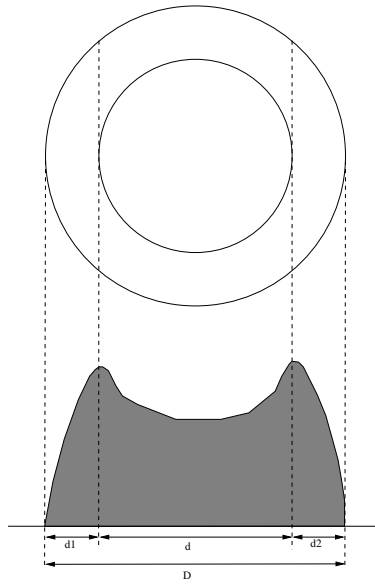


Figure 1.5: Values that can be measured from a summation radiograph. The outer diameter  $D$ , the width of the medullary area  $d$  and the radial and ulnar thickness  $d_1$  and  $d_2$ . Figure redrawn from [11]

### 1.4.3 Radiographic Absorptiometry (RA)

RA is performed with a standard X-ray unit. A standard X-ray image of the hand is used for calculating the BMD of the middle phalanges of the second, third and fourth digits [21]. The optical densities of the bone are calculated by an automated computer system, including some kind of scanning device. For grey level calibration purposes an aluminum wedge is placed on the radiograph when it is taken. RA is a practical and inexpensive method way of determining BMD with a minimal radiation exposure. Its accuracy is 5-6 % and precision error is approximately 2 % [21], [1].

The correlation between RA and BMD measured by dual- and single-photon absorptiometry has been found moderate to high [1].

### 1.4.4 Single-Photon Absorptiometry (SPA)

Single-Photon absorptiometry has been available for more than thirty years and was used to measure bone mass at peripheral sites, most commonly the radius

and calcaneus [9], [6]. A single radiation source is used, normally iodine 125, but more recently an x-ray source has been substituted (SXA). The part of the body to be measured is wrapped in a tissue-equivalent substance or immersed in water to obtain constant soft tissue thickness. Since there is a different photon absorption in tissue than in bone the bone mineral in the path of the beam can be calculated. The advantage of the method is the low radiation dose. The disadvantage is that bone mineral density can not be measured at the spine and the hip and that the theory requires that only two components are present—bone and homogeneous soft-tissue. The method also suffers from a scan time of 15 minutes.

#### 1.4.5 Dual Photon Absorptiometry (DPA)

Dual-energy photon absorptiometry also utilizes a radionuclide source (gadolinium 153), but two energy peaks allow measurements of sites with uneven soft tissue coverage [9]. The sites of measurement are lumbar spine, hip and forearm. Depending on the software any skeletal site can be measured.

The measurement are expressed as grams of mineral per unit area scanned ( $g/cm^2 = \text{area bone mineral density [BMD]}$ ).

With the introduction of DXA the interest for DPA has fallen due to faster scan times, better precision of DXA and the high cost of isotope replacement for DPA. DPA instruments are no longer produced [6].

#### 1.4.6 Dual X-ray Absorptiometry (DXA)

DXA systems employ two X-rays beams, one at higher energy and one at lower. The known differences in absorption of high-energy and low-energy X-rays between bone and soft tissue provide the information required to calculate BMD after subtracting the soft-tissue absorption [21]. DXA has become the gold standard in noninvasive bone mass measurements and the results are used as reference in many studies of alternate techniques.

The precision of DXA is for the spine 0.8–1.5 % and for other sites 1.5–3.0 %. The accuracy is 4–6 % [6].

#### 1.4.7 Quantitative Computed Tomography (QCT)

Quantitative Computed Tomography is currently the only method to measure the three dimensional structure of *in vivo* bone. QCT of the axial skeleton can be obtained with a standard CT scanner but more specialized devices for measuring the peripheral skeleton have been developed (pQCT). X-rays are collected with an electronic detector and as a result thin transverse slices through the body are imaged. Measurements, usually from a single-energy x-ray source, are compared with a standard reference material (such as  $K_2HPO_4$ ) to calculate bone mineral equivalents. Results are expressed as milligrams of  $K_2HPO_4$  per cubic centimeter of bone volume ( $g/cm^3$ ), thereby reflecting three-dimensional bone density rather than the two-dimensional area density of DPA and DXA [9].

A major advantage of QCT is the possibility to distinguish trabecular and cortical bone. The disadvantages are the high radiation dose and the cost of the equipment.

The precision is 2-6 % and the accuracy is 5-15 % [6].

New results indicate that MR scanners can be used.

## 1.5 Motivation for the Study

A radiogrammetric method is developed at Torsana Osteoporosis Diagnostics. The method is able to measure the usual BMD equivalences; radial and ulnar cortical thickness of radius, ulna and the metacarpals. The method also has the ability to quantify cortical resorption.

The correlation between the measured BMD equivalences and BMD measured by DEXA is generally good. The ability to quantify cortical resorption is difficult to validate since no previous methods can be used as reference.

In this thesis a number of methods of measuring the geometric properties of slices of bone are developed. Shape description of the slices that provides intuitive measures of intracortical porosity and endosteal resorption are also quantified by several different approaches.

The found results are used in a validation of the existing radiogrammetric method.

The major result in thesis is not the validation of the existing methods, but that the found methods can be used to evaluate future radiogrammetric methods.

## 1.6 Previous Work

A brief introduction to previous work related to this thesis, is given in this section.

MCI measured on the metacarpals has previously been used in investigations of bone quality and osteoporosis [24],[25] and [5]. Meema has measured the combined cortical thickness at the midshaft of the second metacarpal with a 6 to 7 times measuring magnifier [25].

In a study of the correlation between the combined cortical thickness (CCT) and SPA, CCT of the midpart of the second metacarpal was automatically calculated by image processing. The correlation between CCT and SPA of the proximal and midforearm was satisfactory ( $r = 0.62$  and  $r = 0.50$ ) [10].

The difference between the ulnar and radial cortical thickness has been investigated. The ulnar and radial cortical thickness of the second metacarpal was manually measured. For young patients, the radial cortical thickness proved to be greater than the ulnar thickness, while after the menopause the radial cortical thickness decreased more rapidly [8].

In another study MCI was measured by a digital image processing system and an estimated photodensitometric value  $\sum GS/D$  (the integrated bone mineral density of cortical thickness and trabecular bone on a cross section in the middle of the second metacarpal bone) was calculated.  $\sum GS/D$  is the gray area shown in figure 1.5. Grey level calibration is done by placing an aluminum scale on the radiograph [11].

According to Kanis the estimated cortical area is the most accurate, and correlates closely to estimations of ash weight of the metacarpals [22].

In a study of the relationship between structural parameters on contact radiographs of mandibular slices and texture parameters on periapical radiographs of the mandible the conclusion was that it is meaningful to use texture analysis for assessing bone quality of the mandible [31].

In a study where fracture loads of the radius, femur and lumbar vertebrae of 20 cadavers were compared to the geometric properties of the cortical shell of the bone, a correlation between the geometric properties at the distal radius were highly correlated with the fracture load at the same skeletal site ( $R = 0.89$ ). The geometric properties of the distal radius were also used to estimate the fracture risk at the lumbar vertebrae ( $R = 0.75$ ) and at the femoral neck ( $R = 0.87$ ). The structural properties and the mineral densities of the radius and femora were acquired with peripheral quantitative computer tomography (pQCT).

The conclusion is that radiogrammetry is a relative old technology which have been used by many people with varying results. Unfortunately the traditional, manual method of measuring radiogrammetric properties of a bone suffers from a poor precision, since the edges of the bones are not easily located with the eye. Some rather primitive automated radiogrammetric methods have been tested with varying results.

Also it can be concluded that it is believed that structural properties of the bone yields valuable information in the assessment of fracture risks.

## 1.7 Organization of the Study

A flowchart of the work which has been carried out during the project period, can be seen in figure 1.6.

## 2.1 Radius bone

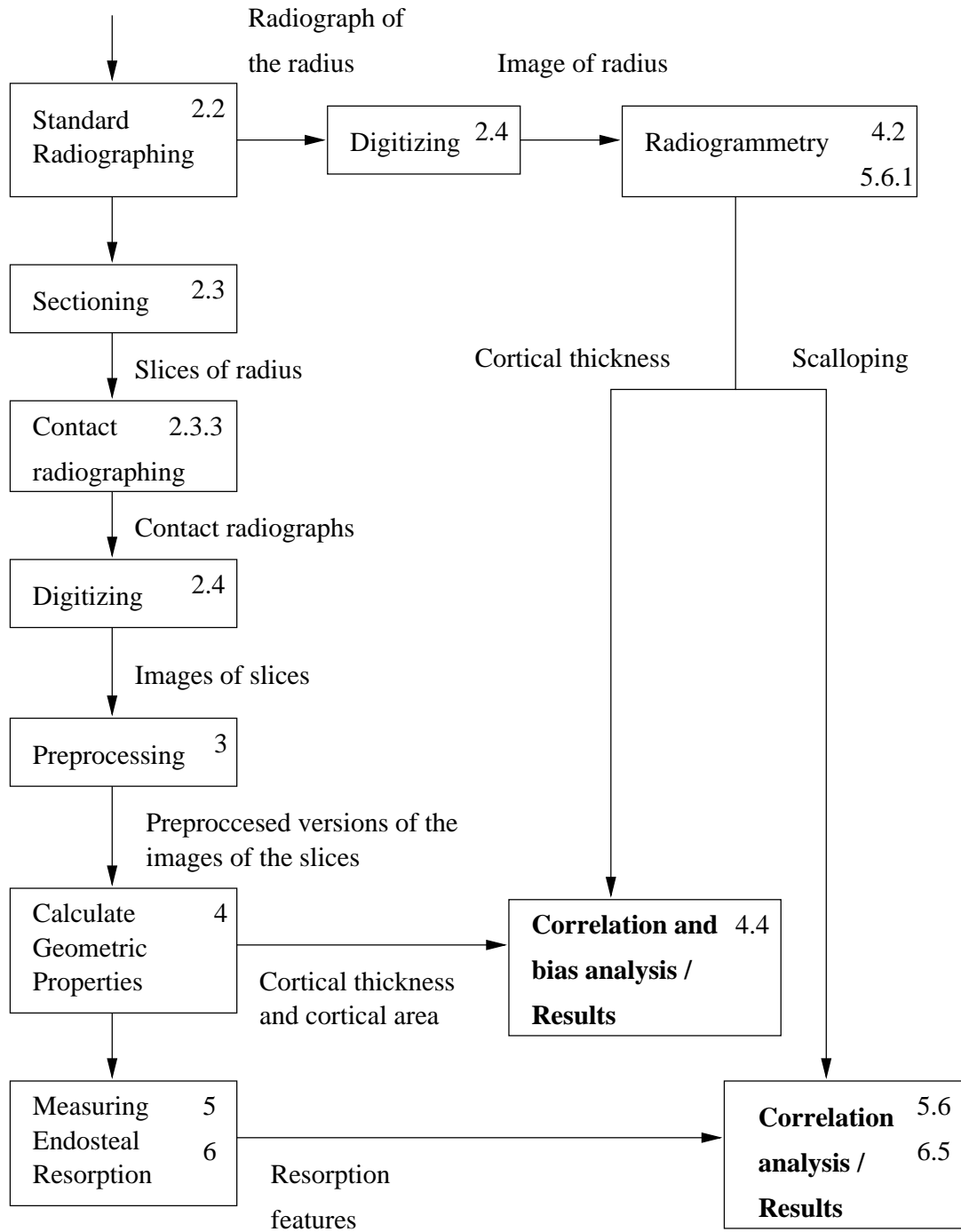


Figure 1.6: The organization of the study. The numbers refer to the section or chapter of the thesis in which the subject is treated.

## Chapter 2

# Materials and Methods

### 2.1 Cadaveric Data

For this study the distal radius from 24 cadavers were made available from the Department of Medical Anatomy, University of Copenhagen. Furthermore 3 ulnas and 3 metacarpals were available. In table 2.1 the material data is summarized.

As seen in table 2.1 only the left arm of female subjects were used in the main study due to the limited time available.

A photograph of some of the used material can be seen in figure A.1, p. 98.

Bones from subject **S1,S2** and **S3** were used in a pilot study where the sectioning and radiographic methods were developed. The remaining bones were used in a main study in which the developed protocol was used. There is a slight difference between the protocol used in the pilot study and the protocol used in the main study.

For the pilot study the periapical radiographs were taken anterior-posterior and in the main study they were taken as posterior-anterior, this is the standard placement of the arm when radiographs are taken.

Bones from 17 subjects were used in the analysis. From each bone a 22–27 slices were cut. The total image material consists of more than 350 images.

### 2.2 Panoramic Radiography

Panoramic radiographs<sup>1</sup> of the radius were obtained with a Siemens Gigantic-Automatic X-ray machine (see photo in figure A.6). The film used is a single coated Trimax FM mammography film. The voltage settings were 46-48 kV and 8 mAs. Film focus distance 100 cm and fine focus 0.6 cm. The used projection were posterior-anterior (PA) (except for bone **r-s1,r-s2** and **r-s3**), which is with the palm downwards. On figure 2.1 an example radiograph of the radius is shown.

---

<sup>1</sup>also called summation radiographs, peripheral radiographs or periapical radiographs.

<b>Radius bone</b>			
Specimen ID	Sex	Age	Side used
S1	?	?	L
S2	?	?	L
S3	?	?	L
S4	F	75	L
S5	M	66	-
S6	M	80	-
S7	F	96	L
S8	M	75	-
S9	F	76	L
S10	F	88	L
S11	F	87	L
S12	F	79	L
S13	F	85	L
S14	F	91	L
S15	F	63	L
S16	M	?	-
S17	M	73	-
S18	M	82	-
S19	F	92	L
S20	M	67	-
S21	F	77	L
S22	F	86	L
S23	F	76	L
S24	F	73	L

Table 2.1: Cadaveric data. Each cadaver is assigned an ID which is shown in the first column. The age of death of the specimen is also shown. As seen is only the left arm of female cadavers used. A minus sign indicates that the specimen is not used in the analysis.



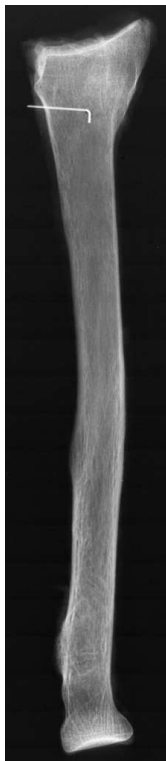


Figure 2.1: Radiograph of the radius. Flesh remaining from the cleansing of the bone causes blurring at the edges. (radius from specimen S19)

### 2.2.1 Indication of Fix Point

To be able to locate the position of the slices on the panoramic radiograph a fix point was made. The fix point is generated by a metal pin going through the bone at a certain position. The hole for the metal pin was drilled with a standard 1 mm drill, while the bone was kept in the exact same position as when the panoramic radiographs were taken (see figure 2.2). To be able to identify the ends of the metal pin on the radiograph the posterior end of the pin (the upward end of the pin when the radiograph was taken) was bend in a 90° angle perpendicular to the bone orientation.

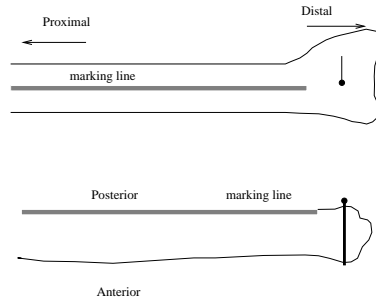


Figure 2.2: Location of metal pin and marking line. The hole for the metal pin was drilled with a standard 1 mm drill, while the bone was kept in the exact same position as when the panoramic radiographs were taken. To be able to identify the ends of the metal pin on the radiograph the posterior end of the pin (the upward end of the pin when the radiograph was taken) was bend in a 90° angle perpendicular to the bone orientation as seen on the upper part of the figure.

### 2.2.2 Perspective Distortion

A distortion factor is introduced on a panoramic radiography due to the physics of an x-ray machine. As seen on figure 2.3 the projection of the metal pin makes the posterior end of the pin the outermost end on the radiograph. Since the slices were cut with the posterior side upwards this mark was used as a fix point in the sectioning of the bone. On the radiograph on figure 2.4 the projection of the metal pin is easily seen. With a film focus distance (FFD) of 100 cm and a distance from the focus point (DF) of 10 cm a pin of 2 cm length ( $d_2$ ) lifted 1 cm ( $d_1$ ) from the film is projected with a length of (see figure 2.3):

$$DD = \text{FFD} \left( \frac{\text{DF}}{\text{FFD} - d_1 - d_2} - \frac{\text{DF}}{\text{FFD} - d_1} \right) \quad (2.1)$$

$$= 100 \left( \frac{10}{97} - \frac{10}{99} \right) = 0.2 \text{ cm} \quad (2.2)$$

This is in agreement with the observations. It will probably have some influence on the results found by radiogrammetry. If the exact position of the bone during the radiographing was recorded, a correction factor could probably be calculated. Perspective distortion and the anisotropy introduced with this phenomenon is out of the scope of this thesis and is not examined further.

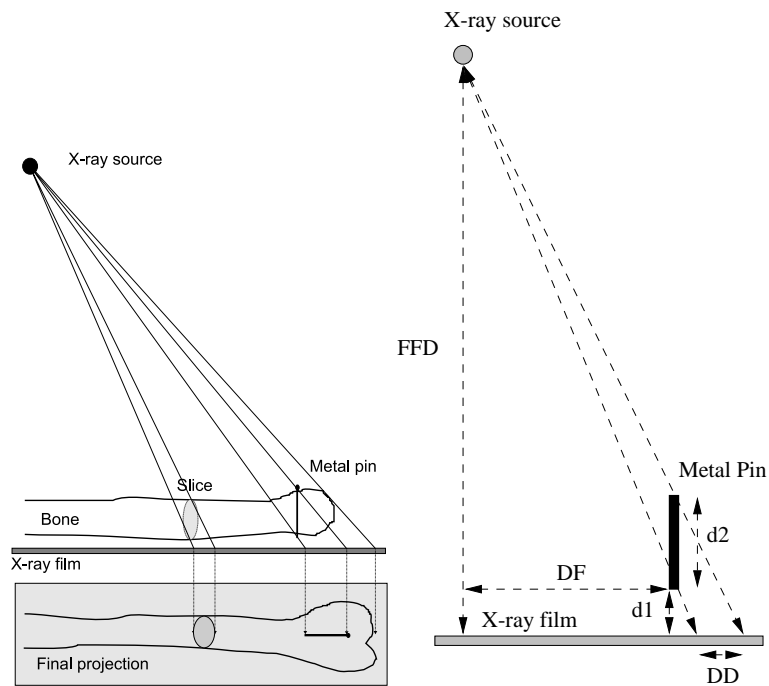


Figure 2.3: Perspective distortion. A distortion factor is introduced on a panoramic radiography due to the physics of an x-ray machine. As seen in the figure, the projection of the metal pin makes the posterior end of the pin the outermost end on the radiograph.



Figure 2.4: Distal end of a radius. The perspective distortion is easily seen. The horizontal bright line is the bend end of the pin (the posterior end). The vertical part is induced by the perspective distortion. (radius from specimen S19)

## 2.3 Sectioning of the Radius

Several different methods have been tested for determining the optimal thickness and placement of the slices. In conclusion it proved extremely difficult to obtain radiographs with a sufficient contrast, if the slices were under 2 mm thick. It was also determined that an optimal placement of the slices was one in which all the slices were cut close to each other.

### 2.3.1 Materials and Methods

The saw used is an Exakt Diamond Saw. The saw is able to cut slices of bone as thin as  $100\ \mu\text{m}$ . The saw itself removes  $350\ \mu\text{m}$  of bone per slice because of the width of the saw blade. The saw can mount a piece of bone of with a maximum length of 3.5 cm. It takes about 1 minute to cut one slice. A photo of the saw in action can be seen on figure A.2, p. 99.

Because of the limited length of bone that can be mounted in the saw (3.5 cm) the region of interest is split into two, a distal (D) segment and a proximal (P) segment. The saw used for splitting the bone was a standard hobby wood saw and it made quite rough cuts (see photo A.3, p. 100), therefore the first slice of each segment is often not used in the analysis. From each segment 11 slices, including the end slice, were cut. Each slice was 2 mm thick, and since the saw blade has a width of  $350\ \mu\text{m}$  there was a distance of  $2350\ \mu\text{m}$  between the slices. The placement of slices can be seen figure in 2.5 and in table 2.4, p. 23.

The advantage of this method is that it is quite easy to take good radiographs of the slices and that the total length of sliced bone is about 6 cm.

### Naming Convention Used While Sectioning the Bone

To easy the manipulation of slices when they are cut, an appropriate naming system is used. Slices cut from the distal segment are assigned even numbers and slices from the proximal segment odd numbers. Slices are named as seen in table 2.2 (from midbone to end). For example is the fourth slice cut from the proximal segment from subject S4 is called R-S4-P-5.

Proximal segment	end, 1, 3, 5, 7, 9,11,13,15,17,19
Distal segment	end, 0, 2, 4, 6, 8,10,12,14,16,18

Table 2.2: Naming of slices when they are cut (from midbone to end).

### 2.3.2 Indication of Posterior and Distal Side

To be able to locate the posterior side of the slices after the sectioning, the posterior side of the bone was marked with a waterproof marker when the summation radiograph was taken as seen in figure 2.2,p. 17. This resulted in a visible spot on the edge of each slice as seen on figure 2.6. When a slice is cut,

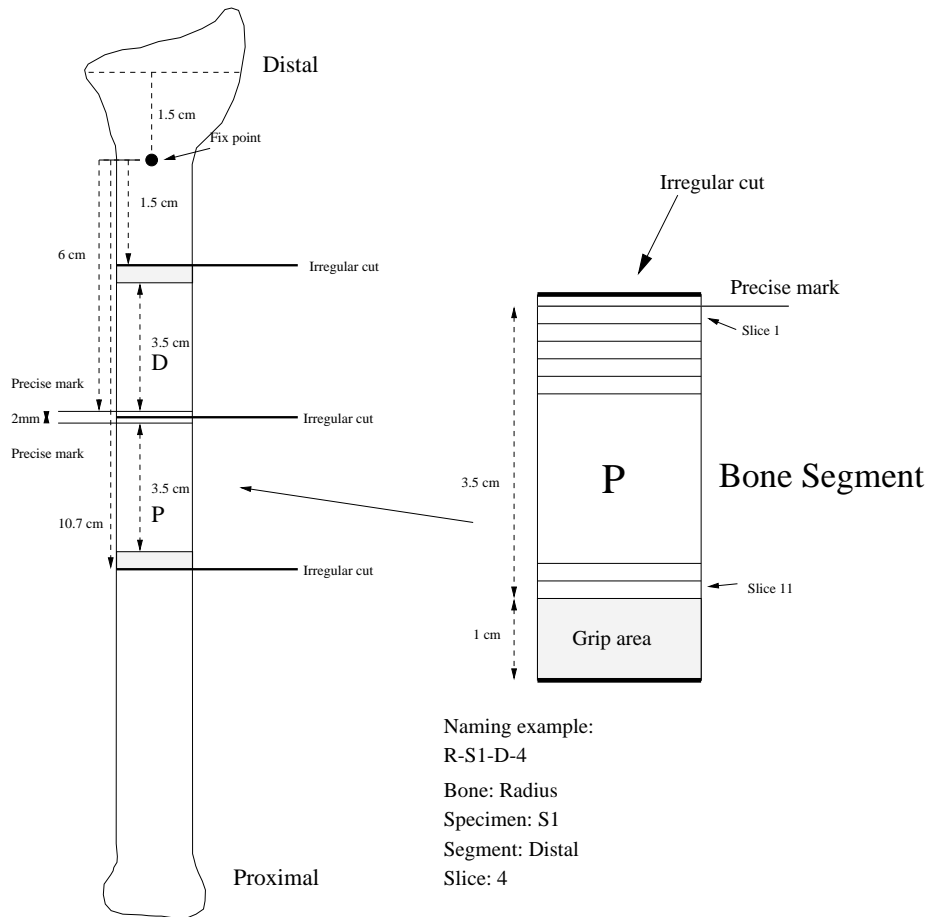


Figure 2.5: Placement of slices. The bone is split into a proximal and a distal segment. From each segment 11 slices are cut. Each slice is  $2000 \mu\text{m}$  thick.

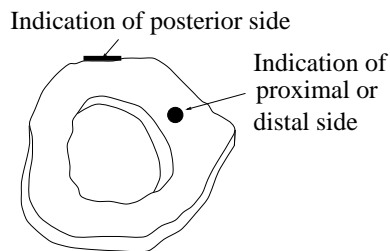


Figure 2.6: On each slice the posterior side is marked with a mark on the edge of the slice. The proximal or distal side is marked with a dot, depending upon which segment the slice belongs to.

the side of the slice away from the mount point is marked with a water proof marker. When a slice is cut from the distal segment the proximal side is marked and when a slice is cut from the proximal segment the distal side is marked (see figure 2.6).

This way the proximal and distal side of all slices can be located.

### 2.3.3 Contact Radiographs

Experiments were performed with different voltage settings during the time of the radiographs. The conclusion is that the best image of a 2 mm thick slice is achieved with a voltage setting of 40 mAs and 40 kV. The used film is a *Trimax FM mammographic*, which is single faced, fine grained film.

### 2.3.4 Naming Convention used in the Analysis

In the study two different naming conventions are used, one is used when the slices are sectioned and the other one is used in the analysis of the radiographs. The reason being that when the bone is sectioned it is split into a proximal and a distal part and the slices from each part are named and marked differently. The second naming method gather the slices into one continuous number format. The lowest number being the most distal of the slices. In table 2.4 the two name conventions and their mutual conversions are shown. For example is slice R-S4-P-5 also named R-S4-17, and this convention is used in the rest of the thesis. As seen the numbers start from 3 and end with 24, this is a result of the pilot study in which more slices are cut from each segment.

### 2.3.5 Placement of Slices when Radiograph is Taken

When the contact radiograph is taken all slices are placed directly on the film with their distal side upwards. Slices from the distal segment are placed with the dot<sup>2</sup> down and slices from the proximal segment are placed with the dot downwards, also the slices are placed with the indication of the posterior side in the same direction. This direction is marked on the radiograph using a small metal object. Table 2.3 shows the placement of slices when the radiograph is taken. The placement of slices on the film can be seen on a photo in figure A.5, p. 102.

3	4	5	6	7	8
9	10	11	12	13	14
15	16	17	18	19	20
21	22	23	24		

Table 2.3: Placement of slices when contact radiograph is taken. The numbers are the ID's of the slices. If the slices were from specimen 15, the slice in the upper left hand corner would be r-s15-03.

---

<sup>2</sup>The waterproof mark made when the slices were cut.

### 2.3.6 Placement of Slices Relative to Fixpoint

The location of each slice relative to the fixpoint is seen in table 2.4. All slices from subject S2 are shifted 3 mm due to a minor measurement error.

Distance from fixpoint is calculated as:

$$n < 13 : b = D - 2.35(12 - n), t = b - 2 \quad (2.3)$$

$$n > 14 : t = D + 2 + 2.35(n - 15), b = t + 2 \quad (2.4)$$

, where  $n$  is the slice number,  $b$  is the placement of the lower part of the slice, and  $t$  the top. The distance from the fixpoint to the indication of the distal segment  $D = 60$  is mm for all bones except S2 where  $D = 63$  mm (see figure 2.5).

## 2.4 Digitizing of Radiographs

Contact radiographs and summation radiographs were digitized using an Eskoscan 2024 scanner. The Eskoscan 2024 is intended for the graphics and pre-press market with high demands for resolution and colour depth. The maximum resolution is 2000 lpc for line art (black and white) and 1000 lpc for grey tone images. The maximum colour depth is 11 bit (= 2048 levels) internally.

The used film, Trimax FM has according to the data sheets a maximal resolution of 10 linepairs per millimeter, which is equal to 20 lines per millimeter [20]. According to Nyquists sampling theorem the minimum required scanning resolution must be twice the source resolution. The minimum resolution for getting all details in the radiograph is then 40 lines per millimeter which is equal to 400 lpc.

The contact radiographs of the slices are scanned in a resolution of 500 lpc, and the summation radiographs are scanned in 250 lpc. The summation radiographs are scanned in a lower resolution to reduce the amount of data and also because the details on the smallest levels are unimportant.

In a resolution of 500 lpc, 1 mm is 50 lines and  $1 \text{ mm}^2$  equals 2500 pixels. In a resolution of 250 lpc, 1 mm is 25 lines and  $1 \text{ mm}^2$  equals 625 pixels.

Naming		Position from fixpoint/mm			
		S1-S24 except S2		S2	
new	old	top	bottom	top	bottom
0	D-24	29.8	31.8	32.8	34.8
1	D-22	32.15	34.15	35.15	37.15
2	D-20	34.5	36.5	37.5	39.5
3	D-18	36.85	38.85	39.85	41.85
4	D-16	39.2	41.2	42.2	44.2
5	D-14	41.55	43.55	44.55	46.55
6	D-12	43.9	45.9	46.9	48.9
7	D-10	46.25	48.25	49.25	51.25
8	D-8	48.6	50.6	51.6	53.6
9	D-6	50.95	52.95	53.95	55.95
10	D-4	53.3	55.3	56.3	58.3
11	D-2	55.65	57.65	58.65	60.65
12	D-0	58	60	61	63
13	D-e	60	61	63	64
14	P-e	61	62	64	65
15	P-1	62	64	65	67
16	P-3	64.35	66.35	67.35	69.35
17	P-5	66.7	68.7	69.7	71.7
18	P-7	69.05	71.05	72.05	74.05
19	P-9	71.4	73.4	74.4	76.4
20	P-11	73.75	75.75	76.75	78.75
21	P-13	76.1	78.1	79.1	81.1
22	P-15	78.45	80.45	81.45	83.45
23	P-17	80.8	82.8	83.8	85.8
24	P-19	83.15	85.15	86.15	88.15
25	P-21	85.5	87.5	88.5	90.5
26	P-23	87.85	89.85	90.85	92.85
27	P-25	90.2	92.2	93.2	95.2

Table 2.4: Names of slices and position relative to fixpoint. The first column is the naming convention used for the slices in the analysis, the second is the naming convention used while sectioning the bone. The positions are the upper (top) and lower (bottom) edge of the slice. There is a distance of  $350 \mu\text{m}$  between the slices, which is the width of the saw blade. Due to a minor measurement error, all slices from specimen S2 is shifted 3 mm.



## Chapter 3

# Preprocessing of Contact Radiographs

Some basic preprocessing of the digitized radiographs is needed before the more advanced algorithms are used. The steps performed in the preprocessing of the digitized radiographs are seen in figure 3.1.

Noise reduction is explained in section 3.1. Automated thresholding is explained in section 3.2. The connected component algorithm is explained in section 3.3. The boundary tracing algorithm is presented in section 3.4. The used alignment method utilizes some of the other methods explained in this chapter and is therefore explained in the last part of the chapter (section 3.5).

### 3.1 Noise Reduction

There is some high frequency noise present in the images, due to the granularity of the film and the fact that they are scanned in a very high resolution. Furthermore the x-ray images were taken with a very low radiation dose and therefore the background is not black but greyish.

A simple filtering technique is used. Initially the image is filtered with a median filter with kernel size  $3 \times 3$ , which removes high frequency noise. Secondly a mean filter with a kernel size of  $3 \times 3$  is applied, which smoothes the histogram. The histogram of a slice is seen before and after the filtering together with the original image in figure 3.2. The histogram after the filtering is bimodal with two peaks nicely separated.

### 3.2 Thresholding

Because of the good contrast in the X-ray images, the histograms of the slices always have two sharply defined peaks, one representing the background and

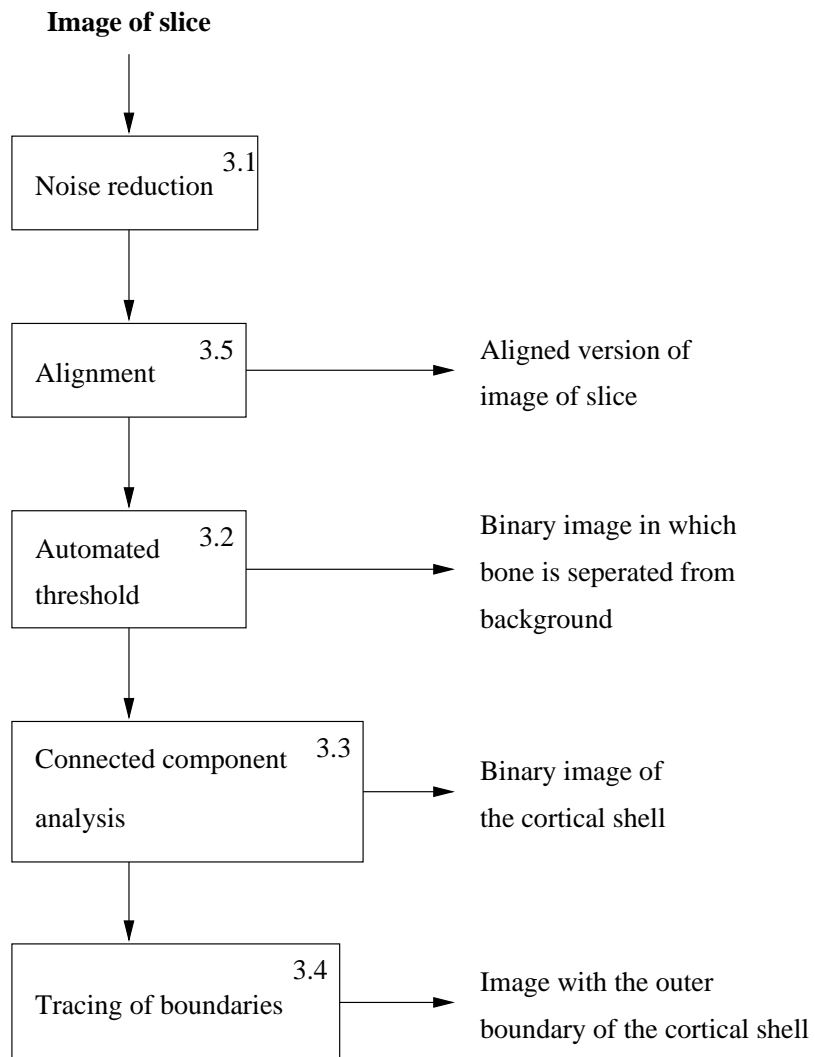
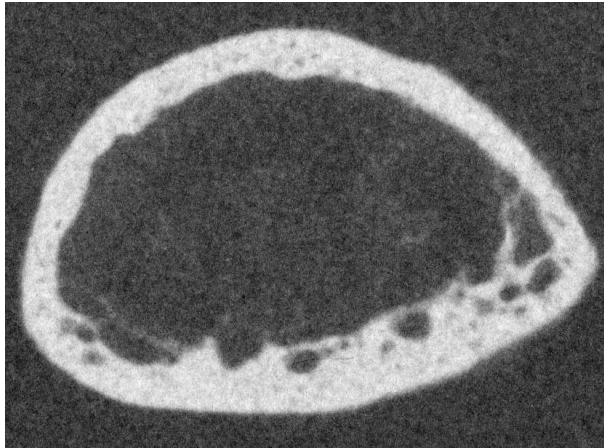
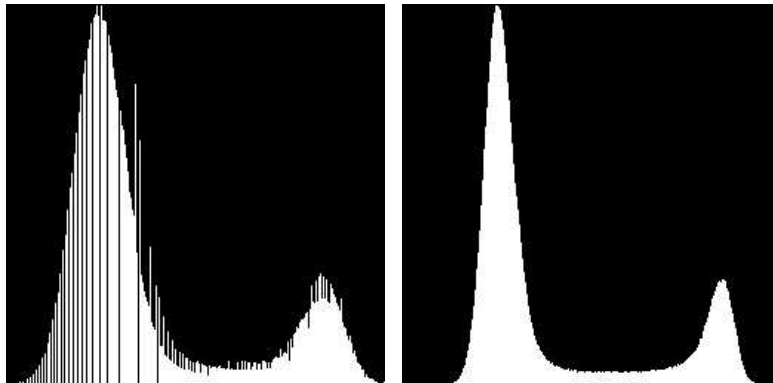


Figure 3.1: The steps performed during the preprocessing of the digitized contact radiographs. The resulting images are also described on the figure. The numbers refer to the section where the subject is explained.



(a) Slice r-s13-04.



(b) Histogram of slice r-13-04. Left peak represents the background, right peak the foreground.

(c) Histogram of slice r-13-04 after filtering. Left peak represents the background, right peak the foreground

Figure 3.2: A slice and its histogram before and after filtering. The image of the slice after the filtering is not shown, since there is no visual difference between the original and the filtered image. (slice r-s13-04)

one for the bone tissue. An optimal threshold must therefore lie between these two peaks.

Four different methods for determining the optimal threshold have been tested. One is an iterative optimal threshold method that finds a threshold in a bimodal histogram. The two of them minimize global objective functions, which are minimum interclass variance and minimum interclass sum of squares respectively. Multiple thresholds can also be computed. The last method locates the two maxima in a bimodal histogram, the threshold is determined as the minimum between the two peaks.

### 3.2.1 Definition of Terms

Some important terms used in the threshold algorithms are introduced. A histogram  $H$  of the image is computed. Only grey-level byte images are considered hence, the histogram is a vector of length 256, each element representing the number of pixels with the current value. For example is  $H(117)$  the number of pixels with value 117.

With a series of  $m$  thresholds  $T_0, \dots, T_{m-1}$  the image pixels is divided into  $m+1$  bins  $b_0, \dots, b_m$  with pixelvalues:

$$[0, T_0[, [T_0, T_1[, \dots, [T_{m-2}, T_{m-1}[, [T_{m-1}, 255].$$

The number of pixels in bin  $k$  is:

$$N_k = \sum_{i \in b_k} H(i) \quad (3.1)$$

The sum of the values of all the pixels in bin  $k$  is:

$$S_k = \sum_{i \in b_k} i H(i) \quad (3.2)$$

The mean value of the pixelvalues in bin  $k$  is:

$$\mu_k = \frac{S_k}{N_k} \quad (3.3)$$

The sum of squares of the pixelvalues in bin  $k$  is:

$$SS_k = \sum_{i \in b_k} H(i)(i - \mu_k)^2 \quad (3.4)$$

The variance of the pixelvalues in bin  $k$  is:

$$\sigma_k^2 = \frac{SS_k}{N_k} \quad (3.5)$$

### 3.2.2 Iterative Optimal Threshold Selection

A method based on approximation of the histogram of an image using a weighted sum of two or more probability densities with normal distribution is called

optimal thresholding. The following method described in [23, p.116–119] sets a threshold based on the shape of the histogram. This method assumes that regions of two main grey levels are present in the image, thresholding of a white bone on black background being an example. The algorithm is iterative, a new threshold generated each iteration. The iteration stops when two successive thresholds are equal.

The first step is to calculate the histogram since all grey level moments of the image can be calculated from this. An initial guess for the threshold  $T_0$  is generated (in this thesis  $T_0 = 127$ ).

At each iteration  $t$  the mean of the background (pixels with value less than the threshold)  $\mu_0^t$  and the mean of the foreground (pixels with value greater than or equal to the threshold)  $\mu_1^t$  are calculated. The mean values are calculated as explained in section 3.2.1 with bin  $b_0$  as the pixelvalues representing the background pixels and bin  $b_1$  for the foreground pixels.

A new threshold for the next iteration is determined from the calculated means:

$$T^{t+1} = \frac{\mu_0^t + \mu_1^t}{2} \quad (3.6)$$

The iteration stops when  $T^{t+1} = T^t$ .

### 3.2.3 Thresholds Based on a Global Objective Function

Another method for locating optimal thresholds have been developed. Multiple thresholds are detected by minimizing a global objective function. Two objective functions have been implemented, namely minimum variance and minimum sum of squares. A series of thresholds  $\mathbf{T} = (T_0, \dots, T_{m-1})$  are computed, which minimize the objective function  $\mathcal{F}$ .

When minimizing the sum of squares, the objective function is:

$$\mathcal{F} = \sum_{i=0}^{i=m+1} SS_i \quad (3.7)$$

,where  $SS_i$  is defined in equation 3.4.

When minimizing the variance, the objective function is:

$$\mathcal{F} = \sum_{i=0}^{i=m+1} \sigma_i^2 \quad (3.8)$$

,where  $\sigma_i^2$  is defined in equation 3.5.

The number of thresholds to be found is supplied to the algorithm, since there is no simple way determining the optimal number of thresholds. The optimal number of thresholds requires prior knowledge of the image.

The algorithm inserts one threshold at a time by finding the most optimal placement, that is the placement yielding the largest decrease in the objective function. This is done by examining all possible places. When a threshold is

added the remaining thresholds are adjusted so the objective function always are at minimum. The adjustment is recursively applied to the neighbours, when a threshold is added, or if a threshold is moved.

The objective functions have been chosen on the assumption that the histogram would be a sum of two or more gaussian distributions.

### 3.2.4 Bimodal Histogram Thresholding, the Mode Method

An algorithm for computing a threshold in an image with a bimodal histogram has been developed. The threshold is determined as the grey level that has a minimum histogram value between the two peaks. The algorithm finds the highest maxima first and detects the threshold as a minimum between them; this technique is called the *mode method* [23, p.117]. To avoid detection of two local maxima belonging to the same global maximum, a minimum distance in grey levels between these maxima is required. In this thesis a minimum distance of 30 grey levels is used.

### 3.2.5 Results and Discussion

The threshold routines were developed using the pilot study (explained in section 2.1,p.14). The quality of the main study could not be assumed to be as good as the pilot study due to the fact that great care were taken and several adjustments to the settings of the x-ray machine were done during the pilot study. Because of that the advanced algorithms were developed. It turned out that the quality of the main study was so good that the simple threshold algorithm explained in section 3.2.4 gives very satisfying results.

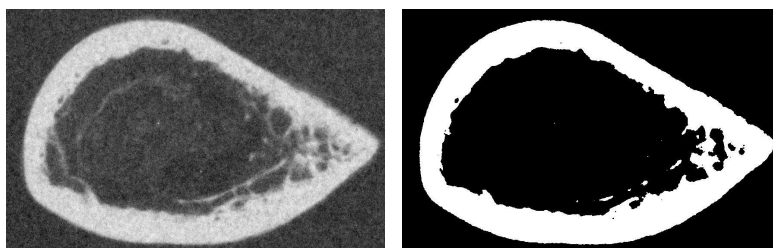
A thresholded image and its histogram is seen in figure 3.3. The result is very satisfactory.

The prototypes for the threshold algorithms are in appendix E.1.

## 3.3 Connected Component Labelling

A method for determining the connected components in a binary image is a recursive flood-fill algorithm. The recursive algorithm is easy to implement but for larger images the computational cost grows and the memory of the computer is heavily loaded.

Therefore a more advanced two pass labelling algorithm that uses deep first search of a graph to find the connected components has been developed. The algorithm returns the labelled image together with a sorted array with component id's and sizes. If the largest component of an image is wanted one just have to mask the output image with the component id of the largest component. The algorithm is able use both 4- and 8-connectivity.



(a) Slice  $r-s9-05$ .

(b) Slice  $r-s9-05$  after thresholding.



(c) The histogram of slice  $r-s9-05$ . The threshold applied to figure 3.3(b) is shown.

Figure 3.3: Slice  $r-s9-05$  its thresholded version and the histogram of the original image.

### 3.3.1 Creating a Connection Graph

An undirected graph is used. The graph is implemented in a *adjacency-list representation*, further details can be seen in [2, p. 465–468]. Each node in the graph represents a label in the image, and the vertices connection between the labels.

In the first sweep of the image all pixels are given an initial label. The labelling starts at the upper left hand corner of the image and continues row by row to the bottom of the image. For each pixel the neighbourhood pixels as shown for 4- and 8-connectivity in figure 3.4 is examined, if one or more pixels in the neighbourhood already have been assigned a label, the pixel is assigned the lowest of these labels. If two neighbours of a pixel have different labels it is called a collision and the labels are added to the connection graph as two nodes connected by a vertex. The labelling concept is adapted from [16, p.189–190].

The labelling of a set of pixels after the first sweep can be seen in figure 3.5(a). The connection graph created from the first sweep is seen in figure 3.5(b). As seen on the figure, pixels with label 5 is connected with pixels with labels 2,6,9 and 10. In the graph this is represented by vertices connecting node 5 with node 2,6,9 and 10.

### 3.3.2 Determining Connected Components

To determine the connected components of the image a translation of labels from the first sweep to the final labels is needed. In table 3.1 the translation of labels from the graph in figure 3.5(b) can be seen.

The translation of labels is found by doing a deep first search of the connection graph.

1. For each non-visited node a new label is created and a deep first search determines all nodes connected to this node.
2. The labels of the nodes found to be connected by the deep first search are entered into the translation table with the same destination label.

A good explanation of deep first searches of graphs is found in [2, p.477–485].

When the translation table is made all pixels in the image are labelled according to the table. In this process pixels with the same label are counted. The result is an image with the connected components each being coloured according to their label, and a vector of number of pixels in each component.

### 3.3.3 Results and Discussion

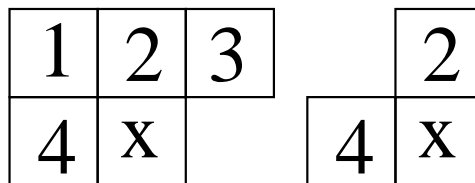
The largest connected component of a thresholded image is seen in figure 3.6. The algorithm works satisfactorily.

The prototype for the algorithm is in appendix E.2.



First label	Final label
1	1
2	1
3	1
4	2
5	1
6	1
7	1
8	2
9	1
10	1

Table 3.1: Translation of labels from graph seen in figure 3.5(b)



(a) The mask used when labelling pixels in 8-connectivity

(b) The mask used when labelling pixels in 4-connectivity

Figure 3.4: The neighbourhood used when labelling components.

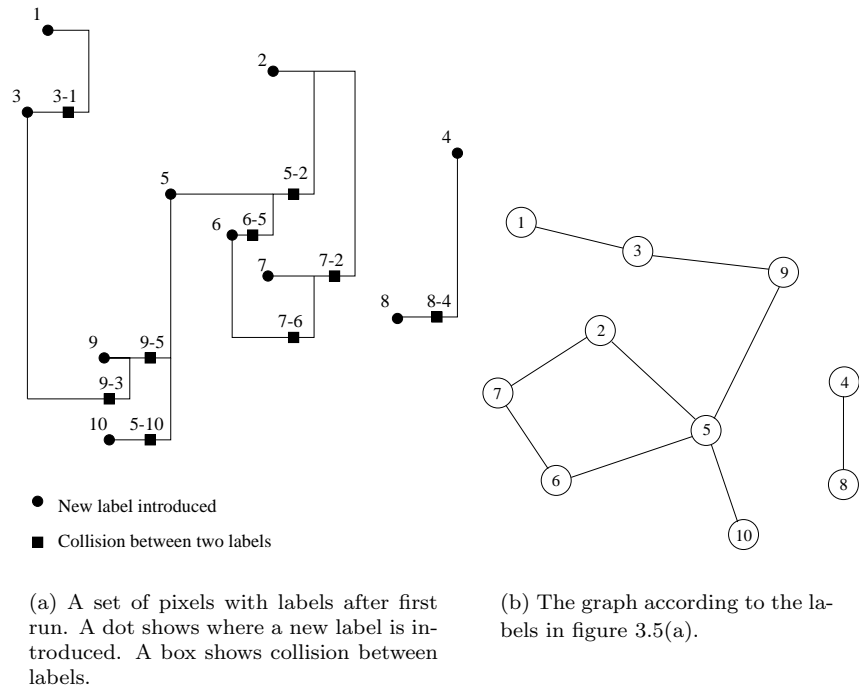


Figure 3.5: A set of pixels labeled after the first run and the graph according to the labels. As seen on the figure, pixels with label 5 is connected with pixels with labels 2,6,9 and 10. In the graph this is represented by vertices connecting node 5 with node 2,6,9 and 10.



Figure 3.6: The largest connected component found in image 3.3(b)

## 3.4 Border Tracing

A method for tracing the boundaries of objects in binary images has been adapted from [23, p.129–132]. The boundary tracer uses 8-connectivity.

Initially an object pixel is found by searching the image from top left. This pixel  $P_0$  is the leftmost pixel of the upper row of pixels belonging to the found object. Pixel  $P_0$  is the starting pixel in the border tracing. A variable  $d$  which stores the direction of the previous move along the border is defined. Initially  $d$  has value 7. The numbered directions are shown in figure 3.7(a).

In each step the 3x3 neighbourhood of the current pixel is searched in an anti-clockwise direction, beginning the neighbourhood search with pixel positioned in the direction:

- $(d + 7) \bmod 8$  if  $d$  is even.
- $(d + 6) \bmod 8$  if  $d$  is odd.

The first object pixel found is a new boundary element  $P_n$ . Before the next iteration  $d$  is updated. An example of a neighbourhood search can be seen in figure 3.7(b).

The tracing is complete when the current boundary element  $P_n$  is equal to the second border element  $P_1$  and the previous border element  $P_{n-1}$  is equal to  $P_0$ . The found boundary, which as seen in figure 3.7(c) is the outer pixels of the object, is stored in an array of points  $P_0, \dots, P_{n-2}$ .

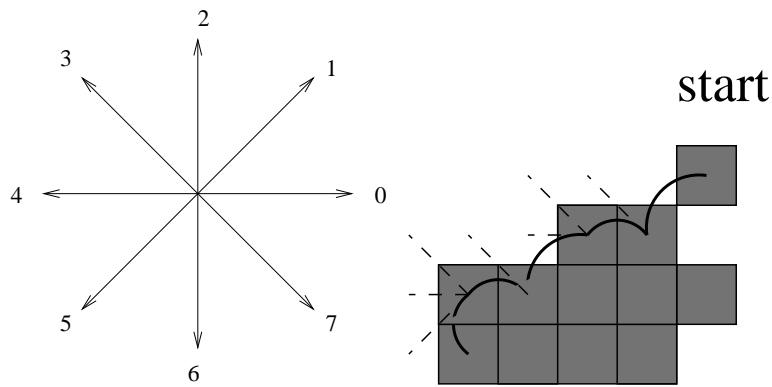
### 3.4.1 Results and Discussion

The boundary tracing is used to trace the boundaries of the cortical shell of the slices. The traced outer boundary of the cortical shell of a slice is seen in figure 3.8. The result is satisfactory.

The prototype for the algorithm is in appendix E.3. A C++ class `parray` which is an array of points has been developed, the class is explained in appendix E.3.4.

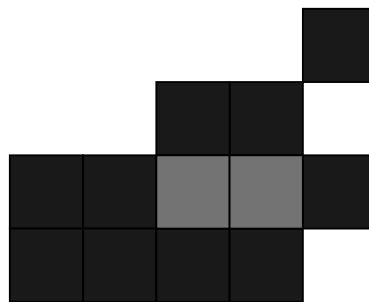
## 3.5 Alignment of Slices

When the radiographs of the slices were taken the slices were manually placed on the X-ray film. This creates an uncertainty of the alignment of the slices. When measuring the cortex width it is necessary to locate the point of measurement precisely on all slices. The mutual translation of the slices is not critical since the width is measured relative to the center of mass of the slice. The rotation is critical since it is necessary to know the exact position of the anterior and posterior side of the slice. In the following two alignment methods are described. First a polar coordinate system of the slices is introduced.



(a) The numbered direction used in boundary tracing.

(b) Example of boundary tracing. The tested pixels is shown with dashed lines. (figure adapted from [23]).



(c) The found boundary of the object is shown with dark areas. It is seen that the boundary is part of the object.

Figure 3.7: Boundary tracing: The search directions and an example of a boundary tracing.

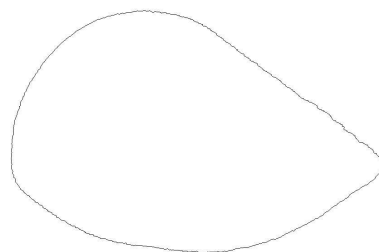


Figure 3.8: The outer boundary of slice r-s9-05. It is a result of tracing the outer boundary of the image seen in figure 3.6,p.33.

### 3.5.1 Polar Coordinate System of the Cortical Shell

A polar coordinate system is defined for a slice. Origo of the polar coordinate system is chosen to be the center of mass of the traced outer boundary since this is the most robust shape description<sup>1</sup>. The polar coordinate system is seen on figure 3.9, where the drop shape of a typical slice is also seen. A point  $p$  in the image with row and column position  $(r_p, c_p)$  (origo upper left) have the coordinates  $(\rho, \varphi)$  in the polar coordinate system. The coordinates are<sup>2</sup>:

$$\rho = \|p - O\|, \quad \tan \varphi = \frac{c_p - c_o}{r_o - r_p} \quad (3.9)$$

, here  $O$  is origo with row and column position  $(r_o, c_o)$ . This is not the standard

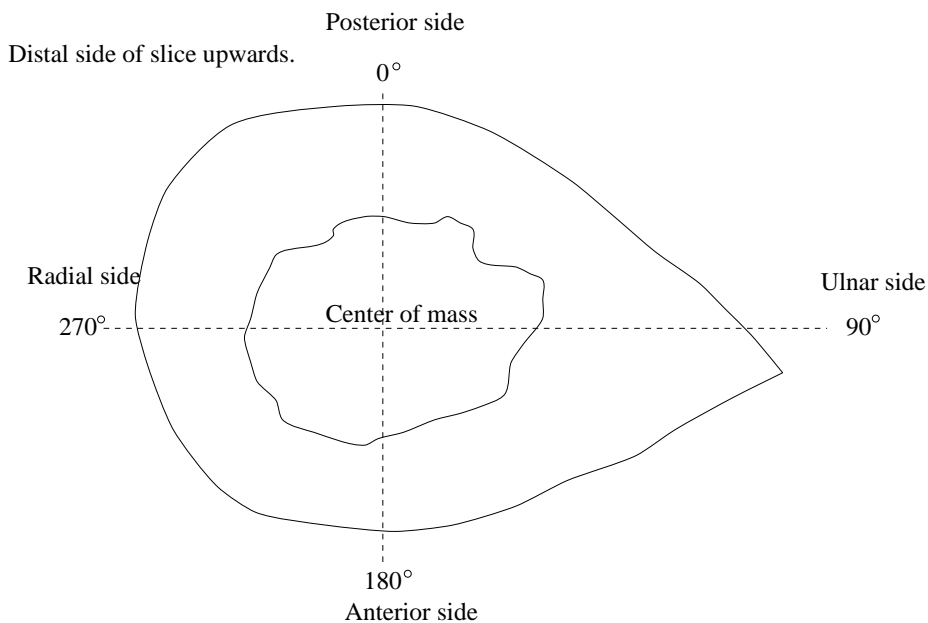


Figure 3.9: Polar coordinate system used.

polar coordinate system seen in the mathematics literature [12]. This system is used since the standard coordinate system used in images is inherited from the matrix row and column system and also because the x-ray hits the slices at angle 0.

### 3.5.2 Global Optimization of Correlation using Steepest Descent

An algorithm for alignment of two images has been developed. The goal is to align the images by a rigid transformation in order to maximize the correlation

<sup>1</sup>Some experiments have been performed to locate the optimal center of mass, currently the traced outer boundary of the slice is used in the calculation of the center of mass. If the center of mass of the whole slice is calculated the shape of the ill defined inner boundary has some influence, which must be avoided.

<sup>2</sup>Most angles in thesis is measured in degrees.

of the two images. A rigid transformation of an image consists of a translation  $\mathbf{t}^T = [t_x, t_y]$  and a rotation  $\theta$ .

The correlation of the reference image  $I$  and the transformed image  $J$  is maximized using the steepest descent algorithm.

This algorithm is designed to work on all images no matter which information the images contain. It is a brute force and very slow alignment method; because of the weaknesses of the steepest descent method this is no guarantee to find the optimal alignment.

### Resampling by Cubic Convolution

An algorithm that takes as input an image, an angle and a translation vector and outputs the transformed image is developed. The image is resampled using cubic convolution. Cubic convolution is an interpolation method that uses two cubic polynomials to define the weighting coefficients for the surrounding points, two to the left and two to the right [27].

The prototype for cubic convolution is in appendix E.5.

### Steepest Descent

The goal is to maximize the correlation of image  $I$  and the transformed image  $J$ . Because of the fact that steepest descent finds the minimizer of a function [7], the objective function is chosen to be the negative correlation:

$$f(\mathbf{t}; \theta) = -\text{cor}(I, J_{(\mathbf{t}; \theta)}) \quad (3.10)$$

Where  $J_{(\mathbf{t}; \theta)}$  is the warped image. The warping consists of a translation  $\mathbf{t}^T = [t_x, t_y]$  and a rotation  $\theta$ .

Steepest descent is an iterative method that produces a series of vectors which normally converges to a minimum. There is no simple method to ensure that the found minimum is a global minimum. The only possible way is trying several different starting points and compare the results. In each iteration a descent direction is chosen and a line search algorithm finds the local minima along this direction. A new iteration starts at the found point in another direction. According to [7, p.34] the steepest descent direction is the opposite of the gradient direction. This results in the fact that for each step the search direction is:

$$\mathbf{h}_{sd} = -\nabla f(\mathbf{t}; \theta) = -\left( \frac{\partial f}{\partial t_x}, \frac{\partial f}{\partial t_y}, \frac{\partial f}{\partial \theta} \right) \quad (3.11)$$

### Soft Line Search

The line search algorithm used is soft line search as described in [7, p.26–32].

The variation of the objective function  $f$  along the direction  $\mathbf{h}$  from the current position  $(\mathbf{t}; \theta)$  is:

$$\varphi(\alpha) = f((\mathbf{t}; \theta) + \alpha \mathbf{h}) \quad (3.12)$$

Since the line search shall stop with an value  $\alpha_s$  so that  $\varphi(\alpha) < \varphi(0)$  two stopping conditions are established. The first condition is:

$$\varphi(\alpha_s) < \lambda(\alpha_s) \quad (3.13)$$

with

$$\lambda(\alpha_s) = \varphi(0) + \alpha \varphi'(0) \delta \quad \text{with } 0 < \delta < 0.5 \quad (3.14)$$

This ensures that the value of  $\varphi(\alpha)$  is lesser than the initial value and that there is a useful decrease in the objective function. The parameter  $\delta$  is chosen to be 0.001.

Since there must be a decrease in function value along the direction  $\mathbf{h}$  at the starting point, the starting tangent to the curve must have a negative slope  $\varphi'(0) < 0$ . At the minimum of the curve the tangent slope must be zero;  $\varphi'(\alpha_{\min}) = 0$ . This gives the second stopping condition that ensures that the step length does not have a too small value.

$$\varphi'(\alpha_s) > \beta \varphi'(0) \quad \text{with } \delta < \beta < 1 \quad (3.15)$$

The parameter  $\beta$  is chosen to be 0.002.

### Approximation to the Gradient

Because the problem is numeric no symbolic gradient exists. The approximation of the gradient used is:

$$\frac{\partial f}{\partial t_x} = \frac{f(\mathbf{t} + (\Delta, 0); \theta) - f(\mathbf{t}; \theta)}{\Delta} \quad (3.16)$$

$$\frac{\partial f}{\partial t_y} = \frac{f(\mathbf{t} + (0, \Delta); \theta) - f(\mathbf{t}; \theta)}{\Delta} \quad (3.17)$$

$$\frac{\partial f}{\partial \theta} = \frac{f(\mathbf{t}; \theta + \Delta) - f(\mathbf{t}; \theta)}{\Delta} \quad (3.18)$$

The parameter  $\Delta$  is chosen to be 0.5 because of the nature of the data, namely images in which the spatial resolution sets a limit of the precision of the parameter estimation.

The approximation of  $\varphi'(\alpha)$  is:

$$\varphi'(\alpha) = \frac{\varphi(\alpha + \Delta) - \varphi(\alpha)}{\Delta} \quad (3.19)$$

The parameter  $\Delta$  is chosen to be 0.5.

### Results and Discussion

The registration has been tested on an image that was pre-translated and pre-rotated. The method could restore this misalignment with a precision of a pixel.

The image to be aligned is warped using cubic interpolation. Another possibility is to use bilinear interpolation. Both methods are available. Cubic interpolation

gives a visually more satisfactory result than bilinear interpolation, but some artifacts are introduced. This means that the final correlation between warped images is not 1.

More advanced optimization routines could be used instead of the very simple steepest descent method. Steepest descents major advantage is the easy implementation and good global behavior. The disadvantage is the linear final convergence that can make the method so slow that it is useless. Another major disadvantage is that the algorithm uses no prior image information.

Other possible optimization methods are Conjugate Gradient Methods and Newton-Type Methods.

In the next section a much more robust and fast alignment algorithm which uses prior knowledge of the shape of a slice is explained.

A prototype for the alignment algorithm can be seen in appendix E.6.

### 3.5.3 Boundary Shape Representation Based Alignment

The steps in this alignment method is shown in figure 3.10. It is seen that most of the methods described in chapter 3, are performed both before and after the alignment of the slices, due to the fact that the alignment method uses some preliminary results to calculate the needed information.

The best and most robust description of the shape of a slice is the outer boundary of the cortical shell. This varies little between neighbour slices though it changes some over greater distances because of the *extremity* on the ulnar side of radius. The traced outer boundary of a slice can be seen in figure 3.8, p. 35.

The goal of this alignment method is to calculate the needed parameters so an image can be warped in such a way that its shape description matches another image's shape description.

#### Boundary Shape Representation

A good shape representation of the outer boundary is the polar coordinate of the points forming the boundary. The polar coordinate system used is explained in section 3.5.1 p. 36. A point  $P$  on the boundary can be identified with the distance  $\rho$  from origo  $O$ , and the angle  $\varphi$  between the y-axis and the vector  $\vec{OP}$ . The distance  $\rho$  from origo to the outer boundary as function of angle  $\varphi$  of slice  $a$  can be seen in figure 3.11.

By discretizing the values of  $\varphi$  a series of polar coordinates of the outer boundary at discrete angles can be achieved.

$$X_i(t) = \rho(\varphi_t) \text{ with } \varphi_t = t \frac{360^\circ}{N} \quad (3.20)$$

, here index  $i$  denotes the slice number in the bone (as an example is  $i = 4$  for slice **r-s7-04**). The number of samples  $N$  is in this thesis 720. It is easily seen



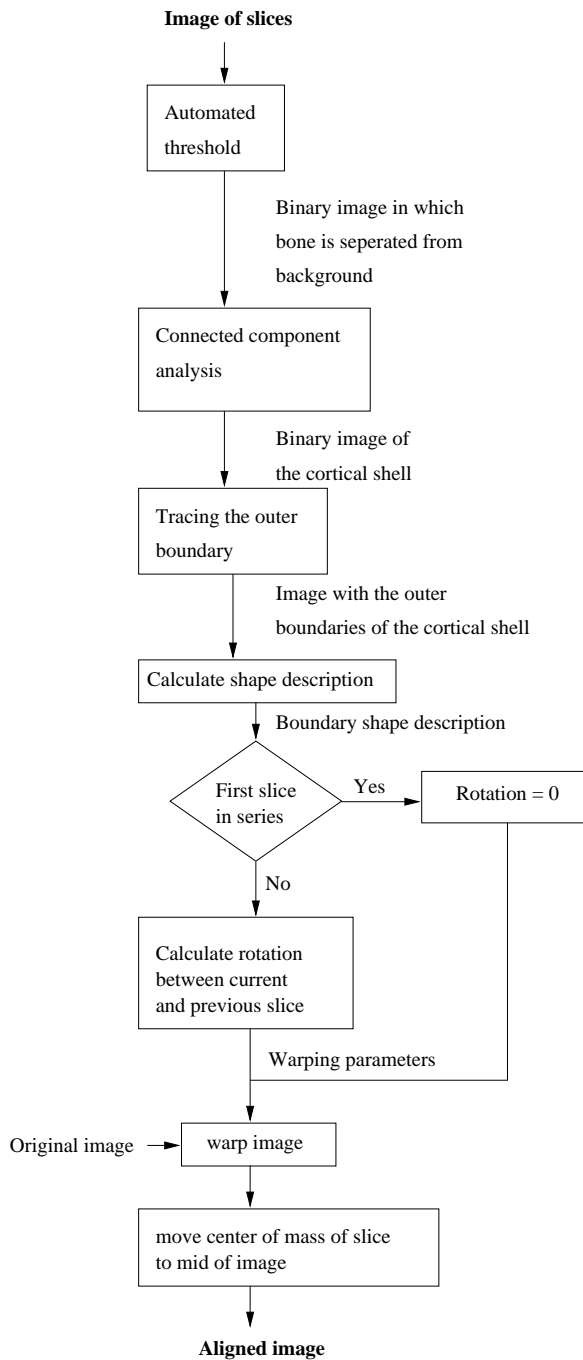


Figure 3.10: The steps performed during the alignment of the slices. It is seen that most of the methods described in chapter 3, are performed both before and after the alignment of the slices, due to the fact that the alignment method uses some preliminary results to calculate the needed information.

that the series of polar coordinates will be periodic with a periodicity of  $360^\circ$  or, in terms of discretization  $N$ . This gives:

$$X_i(t + N) = X_i(t) \quad (3.21)$$

Following [17] some relevant definitions can be made:

Mean and variance of  $X_i$  :

$$E[X_i(t)] = \mu_i \quad (3.22)$$

$$V[X_i(t)] = \sigma_i^2 \quad (3.23)$$

From equation 3.21 it is easily seen that these values are shift invariant.

If measurements  $X_i$  and  $X_j$  from two slices  $i$  and  $j$  are given, the cross covariance function is given as:

$$\gamma_{ij}(u) = \gamma_{X_i X_j}(u) \quad (3.24)$$

$$= \text{Cov}[X_i(t), X_j(t + u)] \quad (3.25)$$

$$= E[(X_i(t) - \mu_i)(X_j(t + u) - \mu_j)] \quad (3.26)$$

Here  $u$  is the lag between the two polar coordinate series.

Further the cross correlation function is given by:

$$\rho_{ij}(u) = \frac{\gamma_{ij}(u)}{\sigma_i \sigma_j} \quad (3.27)$$

### Maximizing the cross correlation

Given measurements from two neighbour slices with a mutual rotation of angle  $\alpha$ . The rotation can be found by finding at which lag  $u^*$  the correlation between  $X_i$  and  $X_j$  is at maximum:

$$u^* = \underset{u}{\text{Argmax}} \rho_{ij}(u) \quad (3.28)$$

Since  $N$ ,  $\mu_i$ ,  $\mu_j$ ,  $\sigma_i$  and  $\sigma_j$  are constant terms, equation 3.28 reduces to a simple summation:

$$u^* = \underset{u}{\text{Argmax}} \gamma_{ij}(u) \quad (3.29)$$

$$= \underset{u}{\text{Argmax}} E[(X_i(t) - \mu_i)(X_j(t + u) - \mu_j)] \quad (3.30)$$

$$= \underset{u}{\text{Argmax}} E[X_i(t) X_j(t + u)] - \mu_i \mu_j \quad (3.31)$$

$$= \underset{u}{\text{Argmax}} \sum_{t=0}^{N-1} X_i(t) X_j(t + u) \quad (3.32)$$

The last summation comes from equation 3.21.

The sought angle is in radians:

$$\alpha = \frac{u}{N} 2\pi \quad (3.33)$$

,or in degrees:

$$\alpha = \frac{u}{N} 360^\circ \quad (3.34)$$

### 3.5.4 Results and Discussion

Two neighbour slices taken from a radius are seen on figure 3.12.

On figure 3.13 the following polar coordinate series are shown:  $X_4(t)$  (slice **r-s1-04**),  $X_5(t)$  (slice **r-s1-05**) and  $X_5(t+u)$  (slice **r-s1-05** aligned). There is a very good correspondence between  $X_4(t)$  and  $X_5(t+u)$ .  $u$  is the lag found by maximizing the cross correlation between  $X_4(t)$  and  $X_5(t+u)$ . The angle corresponding to  $u$  is  $11^\circ$ .

The aligned slices are seen on figure 3.14. The resulting images are larger than the original ones, as the output size is determined so all slices from a bone can fit into it. All slice images end up with the same size.

The aligned images obtained with this method are very satisfactory.

The prototype for the algorithm is seen in appendix E.7, p. 175.

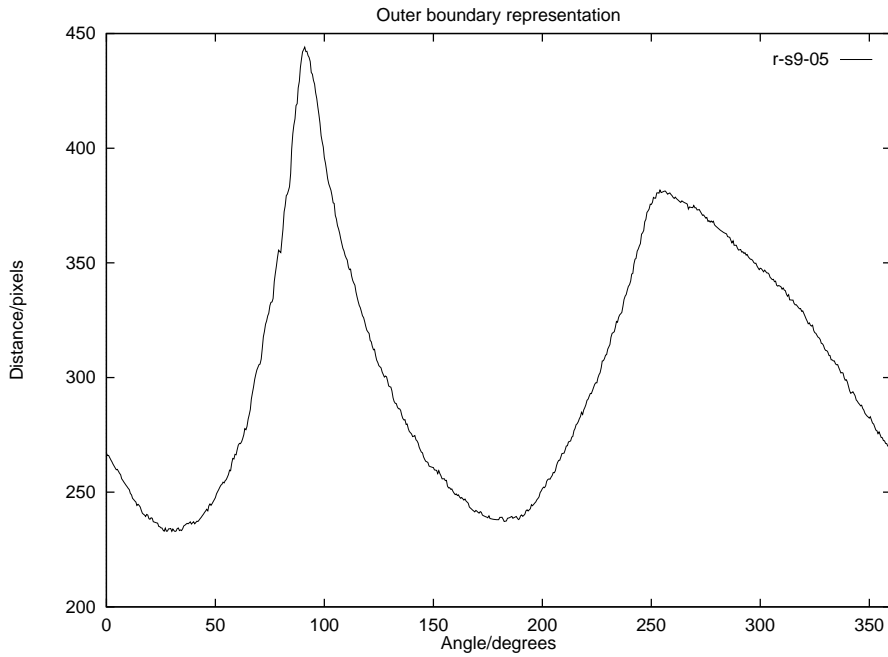
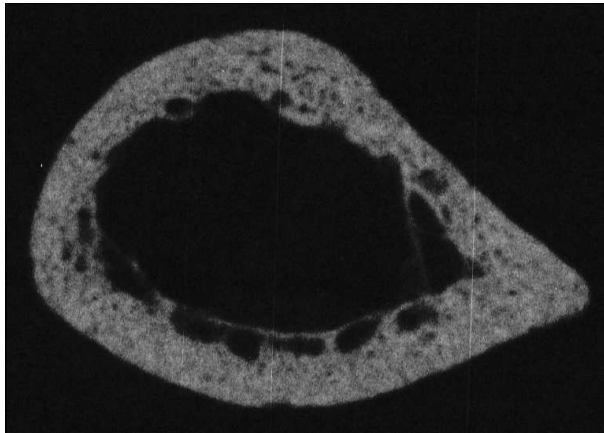
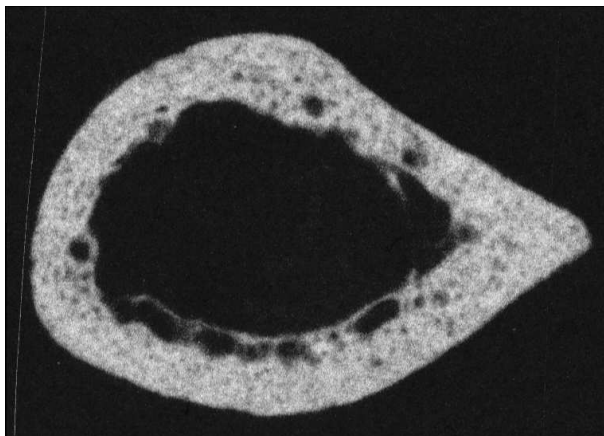


Figure 3.11: The boundary shape representation of slice **r-s9-05**. The ulnar side is represented by the peak at  $90^\circ$  and the radial side by the peak at  $270^\circ$ .



(a) Slice  $r-s1-04$ .



(b) Slice  $r-s1-05$ .

Figure 3.12: Slice  $r-s1-04$  and  $r-s1-05$ . There is a considerable mutual angle.

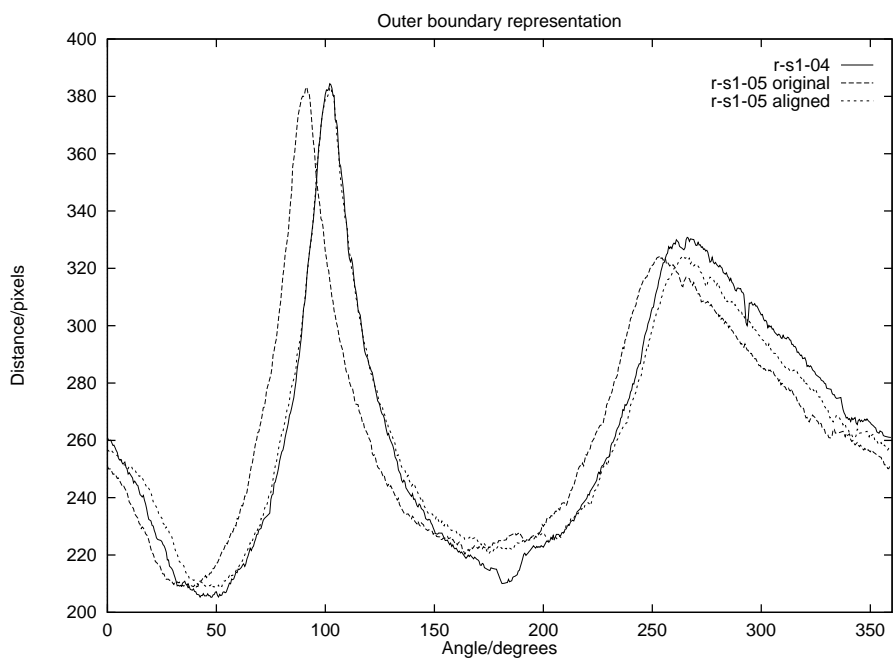
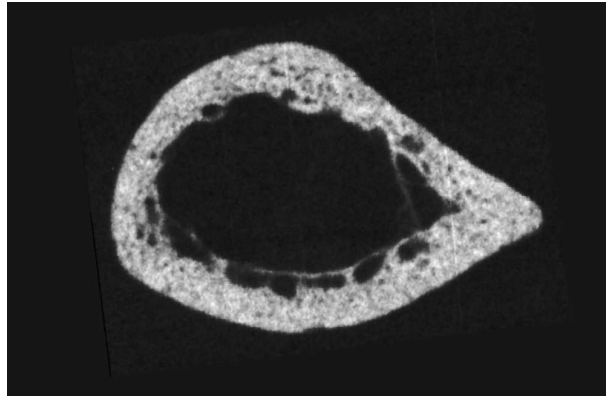
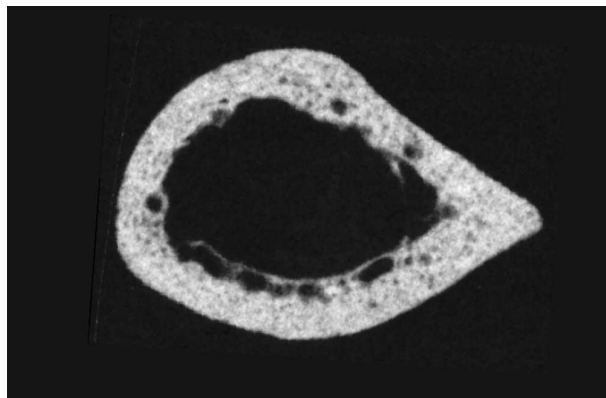


Figure 3.13: Plot of  $X_4(t)$  (slice r-s1-04),  $X_5(t)$  (slice r-s1-05) and  $X_5(t + u)$  (slice r-s1-05 aligned ). There is a very good correspondence between  $X_4(t)$  and  $X_5(t + u)$ .  $u$  is the lag found by maximizing the cross correlation between  $X_4(t)$  and  $X_5(t + u)$ . The angle corresponding to  $u$  is  $11^\circ$ .



(a) Slice  $r-s1-04$  after alignment.



(b) Slice  $r-s1-05$  after alignment.

Figure 3.14: The figure shows slice  $r-s1-04$  and  $r-s1-05$  after they have been aligned.

## Chapter 4

# Geometric Properties of the Cortical Shell

Radiogrammetric measurements of the cortical thickness are thought to be an important component in the assesment of skeletal status, with applications in the assesment of risk fracture and monitoring of treatment.

Torsana Osteoporosis Diagnostics has developed a device for measuring the cortical thickness of the radius, ulna and metacarpals. In this section, the kernel algorithm from this device is used to measure the cortical thickness of the radiuses from the cadaveric data.

A set of methods for measuring the geometric properties of cross-sectional slices of bones are also explained.

The measurements from the contact radiographs are used as an evaluation of the validity of the radiogrammetric measurements.

A correlation and bias analysis is made to estimate the accuracy of the radiogrammetric method.

### 4.1 Measuring the Geometric Properties of the Slices

#### 4.1.1 Cortical Thickness

On figure 4.1 the radial side of two slices from two different bones are shown. There is no resorption in the bone to the left and a lot in the bone to the righ. It is seen that the definition of cortical thickness is ambiguous for the slice with a lot of resorption. The trabeculization and the amount of endosteal resorption makes it hard to make a precise definition of the inner edge. The outer edge is sharply defined.

Three methods for measuring the cortical thickness have been developed. In all methods the polar coordinate system that was introduced in section 3.5.1,p. 36 is used. The results of these are shown in figure 4.4.

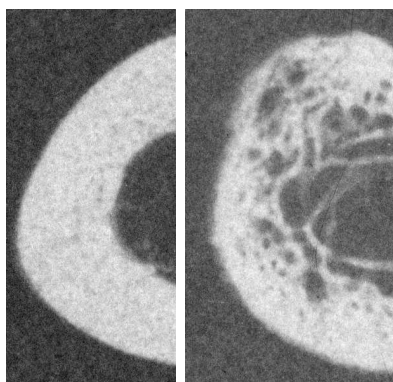


Figure 4.1: The radial side of slice r-s15-05 (left) and r-s24-24 (right). The definition of cortical thickness is ambiguous when there is a lot of resorption.

The first method is based on a tracking of the inner and outer boundaries. The steps are (original image seen in figure 4.2(a)):

- Image is thresholded as described in section 3.2. An example of a thresholded image is seen in figure 4.2(b).
- The cortical shell is located as the largest connected component in the image. The cortical shell of a slice is seen in figure 4.2(c).
- The outer boundary of the cortical shell is traced using the algorithm described in section 3.4.
- The image of the cortical shell is inverted and the two largest components are found, they are the background outside the shell and the medullary area (which is background inside the cortical shell). The medullary area is identified as the component which upper left hand corner has the greatest distance to the upper left hand corner of the image. The medullary area of the slice in figure 4.2(a) is seen in figure 4.3(a).
- The outer boundary of the medullary area is traced. The traced endosteal surface of a slice is seen in figure 4.3(b).

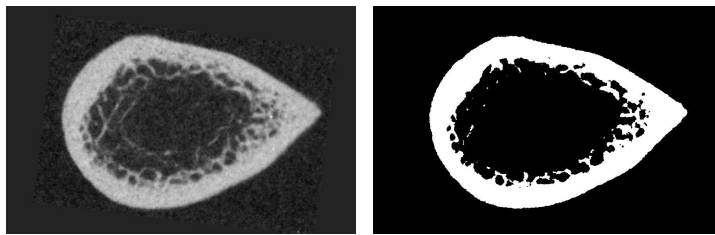
The found inner boundary is very dependent of the endosteal resorption. If a juxtaendosteal resorption space is connected to the endosteal surface, the surface of the resorption space will be considered the endosteal surface, even if the communication is only a few pixels wide. This concludes in an uncertainty of the found result. The measured width  $w_{\text{trace}}$  is found as the distance between the traced inner boundary and the traced outer boundary at a given angle.

The set of pixels forming cortex is denoted  $S$ . The outline of the inner boundary is denoted  $\partial_i S$  and of the outer boundary  $\partial_o S$ . The center of mass of the traced boundary of the cortical shell is denoted  $S_{cm}$ .

Consider a line  $l(\varphi)$  with start point  $S_{cm}$  and slope  $\tan \varphi^1$ . The first interception of  $\partial_i S$  and line  $l(\varphi)$  is called  $p_i(\varphi)$  and the first interception of  $\partial_o S$  and line  $l(\varphi)$

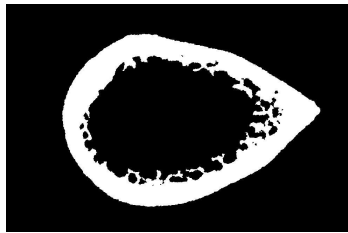
<sup>1</sup>The angle is based on the polar coordinate system introduced in 3.5.1.





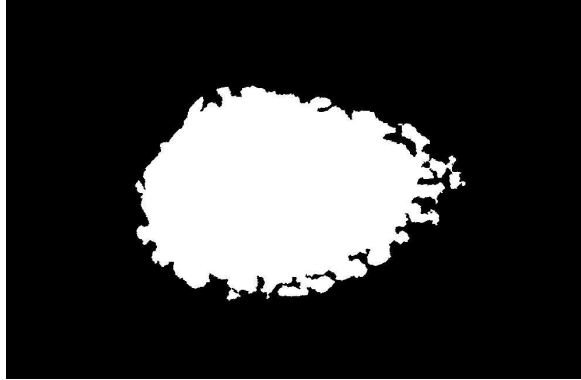
(a) Slice  $r$ -s11-15.

(b) The thresholded version of slice  $r$ -s11-15.

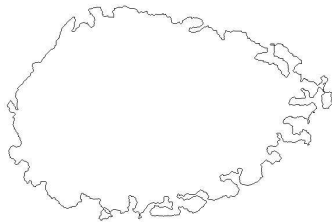


(c) The cortical shell of slice  $r$ -s11-15.

Figure 4.2: Slice  $r$ -s11-15. Original image (a), thresholded image (b) and largest connected component found in thresholded image (c).



(a) The medullary area of slice **r-s11-15**.



(b) The traced inner boundary of slice **r-s11-15**. It is seen that the shape of the boundary is dependent of the endosteal- and juxtaendosteal resorption spaces.

Figure 4.3: The medullary area of slice **r-s11-15** (a) and the traced outer boundary of the medullary area (b).

is called  $p_o(\varphi)$ . The cortical thickness at angle  $\varphi$  is then measured as:

$$w_{\text{trace}}(\varphi) = \|p_o(\varphi) - p_i(\varphi)\| \quad (4.1)$$

In the polar coordinate system,  $p_o(\varphi)$  has coordinates  $(\rho_o, \varphi)$  and  $p_i(\varphi)$  has coordinates  $(\rho_i, \varphi)$ . That gives  $w_{\text{trace}}(\varphi) = \rho_o - \rho_i$ .

In the second method the thresholded image with the cortical shell as single component is used (see figure 4.2(c) for an example). Here point  $p_i(\varphi)$  is the object pixel in the polar coordinate system with minimum distance from origo at angle  $\varphi$ . The outer boundary pixel is the object pixel with maximum distance from origo at angle  $\varphi$ . The points are found by examining a line with angle  $\varphi$  from origo to the outer boundary of the image. The cortical thickness at angle  $\varphi$  is then measured as:

$$w_{\text{hit}}(\varphi) = \rho_o - \rho_i \quad (4.2)$$

In the third method the thresholded image is used (see figure 4.2(b) for an example). For a given angle  $\varphi$  object pixels with polar coordinates  $(\rho, \varphi)$ ,  $\rho \in \mathcal{R}^+$  are counted and used as an approximation of the cortical thickness. This is equal to the bone mass passed by a beam from the center of mass to the outer boundary of the slice.

$$w_{\text{sum}}(\varphi) = \sum_{\rho \in \mathcal{R}^+} I(\rho, \varphi) \quad (4.3)$$

, here  $I(\rho, \varphi)$  is the pixel value at polar coordinates  $(\rho, \varphi)$ . The pixel value is 1 for objects and 0 for background.

The prototypes for the developed algorithms are in appendix E.8.

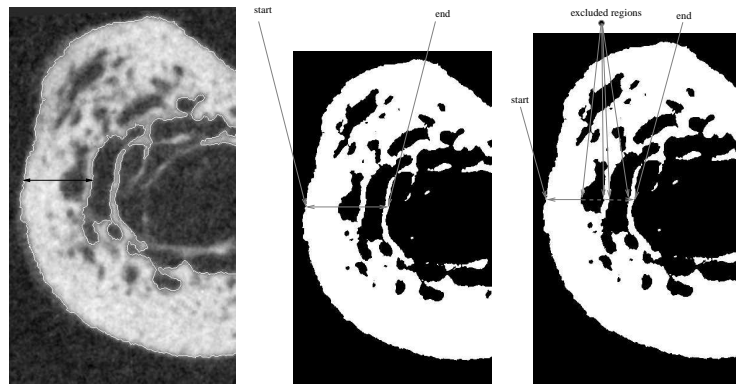
### Cortical Thickness Measured at Different Angles

The slices are all from the radius of left hand, and therefore four positions in the polar coordinate system introduced in section 3.5.1, p. 36 can be named.

The four different sides of the slice is placed at angles:

- The posterior side is at  $0^\circ$ .
- The ulnar side is at  $90^\circ$ .
- The anterior side is at  $180^\circ$ .
- The radial side is at  $270^\circ$ .

The cortical thickness has been measured with the three methods explained in the previous sections, at the four angles. An additional measurement, the maximum distance from origo to the outer boundary (on the ulnar side) is also measured. The sites of measurement are shown on a slice in figure 4.5. The measured values are average values computed over a set of angles which can be controlled by a parameter. The angle used in this thesis is  $10^\circ$ . The used angle resolution is  $0.5^\circ$  per sample.



(a) Method 1: Distance from traced inner and outer boundary.

(b) Method 2: Distance from first object pixel encountered to last pixel encountered.

(c) Method 3: Number of pixels encountered.

Figure 4.4: Three methods to measure the thickness of the cortical shell. In the first method the distance between the traced inner and outer boundary is measured. In the second method the distance between the innermost endosteal edge and the outer edge is measured. In the third method the approximate bone mass passed by a beam from the center of the slice is measured.

The total width of the slice is also measured. This is done by examining a thresholded image containing only cortex. The total width of the slice is measured as the horizontal distance between the object pixel to the outer left and the object pixel at the outer right.

The endpoint variables<sup>2</sup> are seen in table 4.1.

#### 4.1.2 Cross-sectional Cortical Area

Two methods to measure the cortical shell area have been developed. In the first method the thresholded image is used (see figure 4.2(b), p. 48 for an example). The cortical area  $A_{res}$  is measured as the number of object pixels divided by the square of the resolution of the image.

In the second method the area measured is the area of the slice when the intracortical resorption is neglected. The cortical shell with no intracortical resorption is found in the following way (original image of the slice used in the examples is seen in figure 4.6):

- An image with the traced inner and outer boundary is generating using the method that is described in section 4.1.1, p. 46. An example is seen in figure 4.7.

<sup>2</sup>An endpoint variable is a measured value used in the analysis.

Cortical thickness endpoint variables measured on slices		
The sum method	$w_{\text{sum,pos}}$ $w_{\text{sum,uln}}$ $w_{\text{sum,ant}}$ $w_{\text{sum,rad}}$ $w_{\text{sum,uln,max}}$	$w_{\text{sum}}$ at posterior side. $w_{\text{sum}}$ at ulnar side. $w_{\text{sum}}$ at anterior side. $w_{\text{sum}}$ at radial side. $w_{\text{sum}}$ at site where distance from center of mass to outer boundary at ulnar side is at max.
The hit method	$w_{\text{hit,pos}}$ $w_{\text{hit,uln}}$ $w_{\text{hit,ant}}$ $w_{\text{hit,rad}}$ $w_{\text{hit,uln,max}}$	$w_{\text{hit}}$ at posterior side. $w_{\text{hit}}$ at ulnar side. $w_{\text{hit}}$ at anterior side. $w_{\text{hit}}$ at radial side. $w_{\text{hit}}$ at site where distance from center of mass to outer boundary at ulnar side is at max.
The trace method	$w_{\text{trace,pos}}$ $w_{\text{trace,uln}}$ $w_{\text{trace,ant}}$ $w_{\text{trace,rad}}$ $w_{\text{trace,uln,max}}$	$w_{\text{trace}}$ at posterior side. $w_{\text{trace}}$ at ulnar side. $w_{\text{trace}}$ at anterior side. $w_{\text{trace}}$ at radial side. $w_{\text{trace}}$ at site where distance from center of mass to outer boundary at ulnar side is at max.
	$w_{\text{total}}$	The total slice width.

Table 4.1: Cortical thickness endpoint variables.

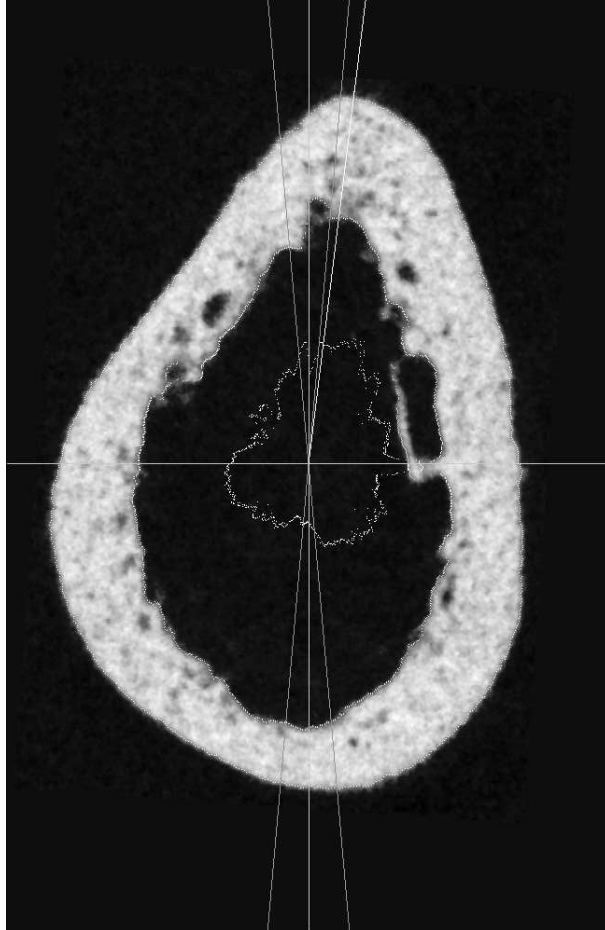


Figure 4.5: The sites of measurements of the cortical thickness are seen on a slice. The measured values are the average computed over a set of angles shown at the radial and the distal side. The angle where there is maximum distance from origo to the outer boundary is also shown. The sum of object pixels at all angles are shown with bright pixel each having the polar coordinates  $(w_{\text{sum}}(\varphi), \varphi)$ . Note that the image is rotated  $90^\circ$  anticlockwise. (Slice r-s4-04)

- The three largest components are found in the inverted image, they are the background outside the shell, the cortical shell and the medullary area (which is background inside the cortical shell). The medullary area is identified as the component which upper left hand corner has the greatest distance to the upper left hand corner of the image. The background area is found as the component which upper left hand corner has the smallest distance to the upper left hand corner of the image. The sought cortical area is the last of the three. The cortical area of figure 4.6 is seen in figure 4.8.

The cortical area  $A_{\text{nores}}$  is measured as the number of object pixels divided by the square of the resolution of the image.

The generated features are:

$A_{\text{res}}$  The area of the cortical shell.

$A_{\text{nores}}$  The area of the cortical shell when the intracortical porosity is neglected.

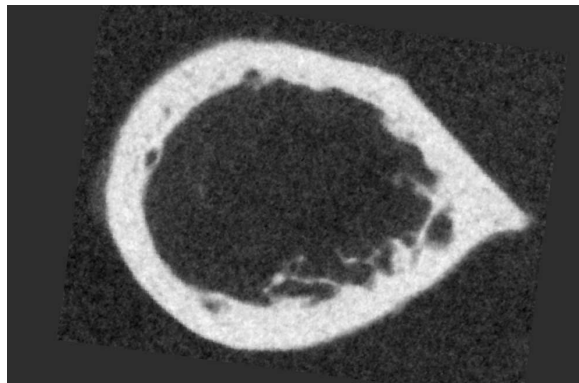


Figure 4.6: Slice r-s13-19.

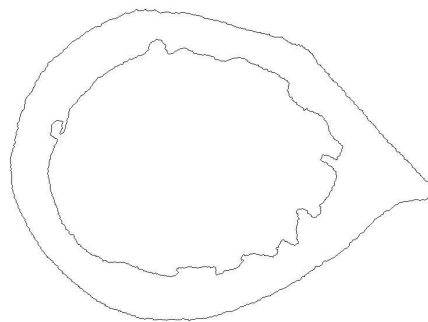


Figure 4.7: The inner and outer boundary of the cortical shell of slice r-s13-19.



Figure 4.8: The cortical area with filled resorption spaces of slice r-s13-19.

## 4.2 Cortical Thickness Measured by Radiogrammetry

The radiogrammetry module developed at Torsana Osteoporosis Diagnostics has been used to measure the cortical thickness. The values measured by radiogrammetry are shown in table 4.2. All measurements are made on extracted regions from radius. The measurements are indexed by their distance to the fix point on the summation radiograph. A feature vector containing measurements and their positions is computed.

The used region from a radius with the result returned by the radiogrammetry module is shown in figure 4.9, p. 56. The bright lines are from left to right: outer boundary at ulnar side, inner boundary at ulnar side, inner boundary at radial side and outer boundary at radial side. The bright region indicates where the cortical thickness are measured, it is where the outer diameter is at a minimum. The measured cortical thickness is an average value of the values measured in the area. The features returned from the radiogrammetry module are seen in table 4.2.

Cortical thickness endpoint variables measured by radiogrammetry	
$w_{\text{rad,RA}}$	Radial slice width.
$w_{\text{uln,RA}}$	Ulnar slice width.
$w_{\text{total,RA}}$	The total slice width.

Table 4.2: Cortical thickness endpoint variables. Measured by radiogrammetry.

## 4.3 Cortical Thickness Measured on a Simulated Radius

For each bone a simulated radius is produced using slices from the bone. The radius is created by simulated radiographing of the slices. The simulated radius



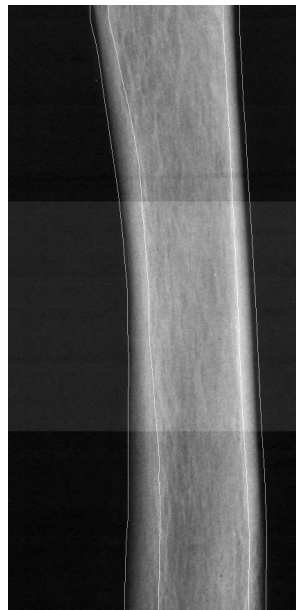


Figure 4.9: The result returned from the radiogrammetry. The bright lines are from left to right: outer boundary at ulnar side, inner boundary at ulnar side, inner boundary at radial side and outer boundary at radial side. The bright region indicates where the cortical thickness is measured, it is where the outer diameter is at minimum. The measured cortical thickness is an average of the values measured in the bright area. (The region is from radius  $r-s4$ )

is used as input to the radiogrammetry module in order to verify the performance on known data.

### X-ray Imaging

In this section the correspondence between bone thickness and the image intensity measured by the computer is established. The following is inspired by [28].

The object under examination attenuates the x-ray beam emitted from the x-ray source. The photons hits a amplifying screen which emits green light proportional to the quantity of photons. The green light exposes the x-ray film. Finally the x-ray film is developed and digitized.

From the x-ray source photons are emitted with intensity  $I_0$ . The attenuation formula when the x-ray beam hits an object is:

$$I = I_0 \exp(-\mu\rho w) \quad (4.4)$$

, where  $w$  [cm] is the thickness of the object,  $\rho$  [g/cm<sup>3</sup>] the mass density and  $\mu$  [cm<sup>2</sup>/g] the attenuation coefficient. The intensity of the beam after passing through the object is  $I$ .

In this section it is assumed that only bone is present and therefore this simple attenuation equation is sufficient. The parameters are generally unknown.

The relation between the optical density (OD) on a developed and digitized x-ray image is:

$$OD = \gamma \log(I \cdot t) + c \quad (4.5)$$

, here is  $\gamma$  and  $c$  unknown parameters and  $t$  the exposure time.

Assuming that digitizing is a linear transformation of optical densities into pixel values, combining equation 4.4 and 4.5 yields:

$$OD = \gamma \log(I_0 \cdot t) - \gamma\mu\rho w + c \quad (4.6)$$

$$= -\alpha w + \beta \quad (4.7)$$

The conclusion is that there is linear dependency between bone thickness and optical density.

If a wedge of isotropic material with linear increasing thickness was radiographed, the image intensities in the digitized radiograph should be linearly increasing.

### Simulated Slice Profile

From each slice a simulated profile is calculated. The profile is a simulation of an x-ray hitting the slice from the posterior side and continuing out of the anterior side and then hitting an x-ray film as seen in figure 4.10. Therefore the simulated projection is posterior-anterior<sup>3</sup>.

---

<sup>3</sup>Note, that with the used method there would be no difference if the projektion used was anterior-posterior.

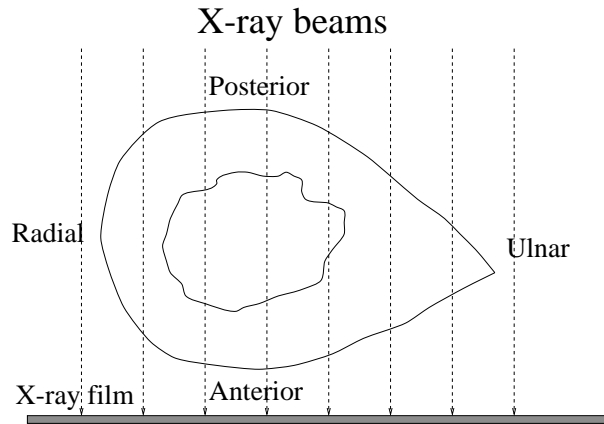


Figure 4.10: A simulated profile of a slice is computed by summing the object pixels in each column.

Since there has been no concerns regarding the grey-levels of the images they cannot be used as a measure of bone mass. If an aluminum reference wedge was placed near the slices when the contact radiograph was taken, the image of the wedge could be used to make a grey-level calibration. This is out of the scope of this thesis. Therefore only the shape of the slice has been used in the simulated profile. The shape used is the thresholded image where the cortical shell is found being the largest connected component as described in section 3.3, page 29, an example is seen in figure 4.11.

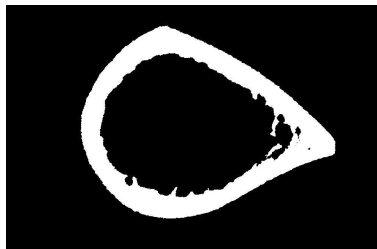


Figure 4.11: Image used in simulated profile. Slice r-19-09.

A matrix  $\mathbf{P} \in \mathcal{R}^{m \times n}$  of simulated profiles from all the slices from the bone is created. The number of slices is  $m$  and the number of columns of the simulated profile is  $n$ . The rows of  $\mathbf{P}$  is the simulated profiles of the  $m$  slices.

It is assumed that all slices are aligned so that there no mutual rotation and that all images have the same dimension.

For each slice the projection is calculated as the sum of object pixels per column. As explained in section 4.3, this a sound approximation of the physics of x-rays attenuated by bone.

$$p_{ij} = \sum_{k=0}^{N-1} I(k, j) \quad (4.8)$$

, here  $p_{ij}$  is element  $ij$  in  $\mathbf{P}$ ,  $i$  is the slice number,  $I(k, j)$  is the image value at position  $(k, j)$  (this is 1 or 0 since it is a binary image) and  $N$  is the number of rows in the input images. The profiles are aligned so their midpoints are at the mid of the image of the simulated projection. Values outside the image boundaries are assumed to be zero.

The simulated profile for the slice seen in figure 4.11 is seen in figure 4.12. Notice that the radial side is very clearly defined as a peak in the left side of the profile, while the ulnar side is much harder to detect. This is caused by the scalloping of the endosteal surface and because a cross-section of a bone is drop shaped. The radial side is nearly circular while the ulnar side is more elliptical.

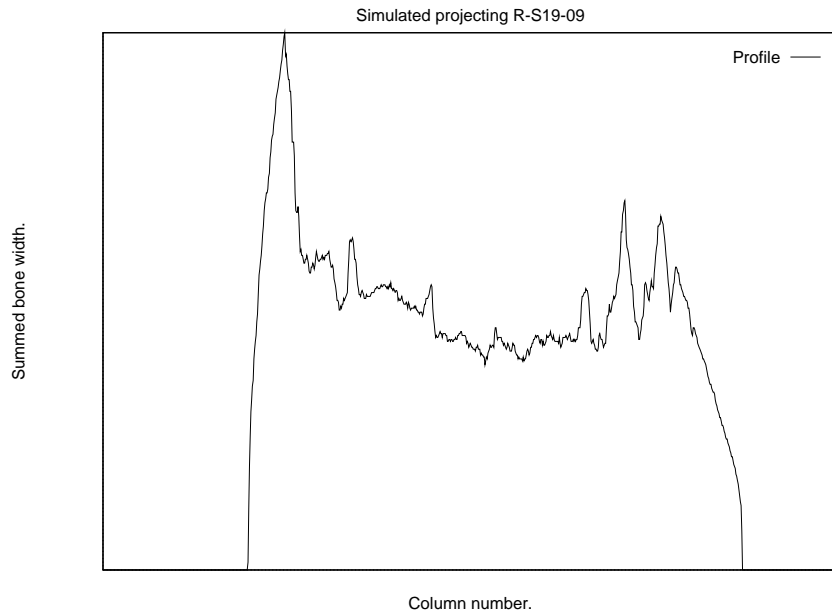


Figure 4.12: Simulated profile made from image 4.11 (slice r-s19-09). Note that the radial side is to the left and the ulnar side to the right.

### Creating a Simulated Radius

The simulated profiles of all the slices in a bone are used in the simulation of the radius. The vertical positions relative to the fix-point of the slices are stored in a vector  $v \in \mathcal{R}^m$ . The positions are stored in pixel coordinates with origo in the upper left hand corner of the output image.

Each pixel in the interpolated simulated radius is computed as:

$$I_p(r, c) = t_2 p_{ic} + t_1 p_{i+1c} \quad (4.9)$$

, here  $I_p(r, c)$  is the pixel value in the simulated radius at position  $(r, c)$ ,  $t_1$  and  $t_2$  are the interpolation weights determined by the distances of the point from the two nearest slices. For a given point  $p = (r, c)$  the neighbour slices are number  $i$  and  $i + 1$ , seen in figure 4.13. Their vertical distance is  $v_{i+1} - v_i$ . The

vertical distance from point  $p$  and slice  $i$  is  $r - v_i$ . Therefore the weights are calculated as:

$$t_1 = \frac{r - v_i}{v_{i+1} - v_i} \quad (4.10)$$

$$t_2 = 1 - t_1 \quad (4.11)$$

If  $p$  is located before the first slice or after the last slice, the output intensity is extrapolated from the nearest slices.

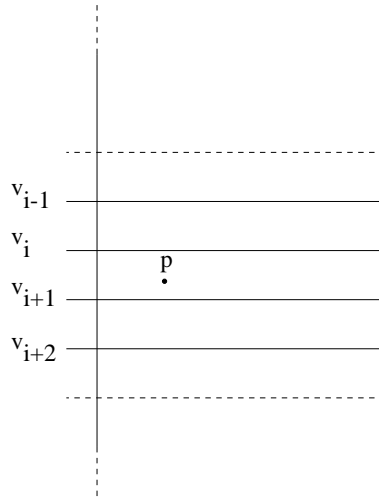


Figure 4.13: The pixel value at a point in the simulated radius is interpolated from the values of the profiles of the two nearest neighbor slices. For point  $p$  the nearest slices are number  $i$  and  $i + 1$  with vertical positions  $v_i$  and  $v_{i+1}$ .

A simulated profile made using the slices from bone **r-s7** is seen in figure 4.14 together with the real region.

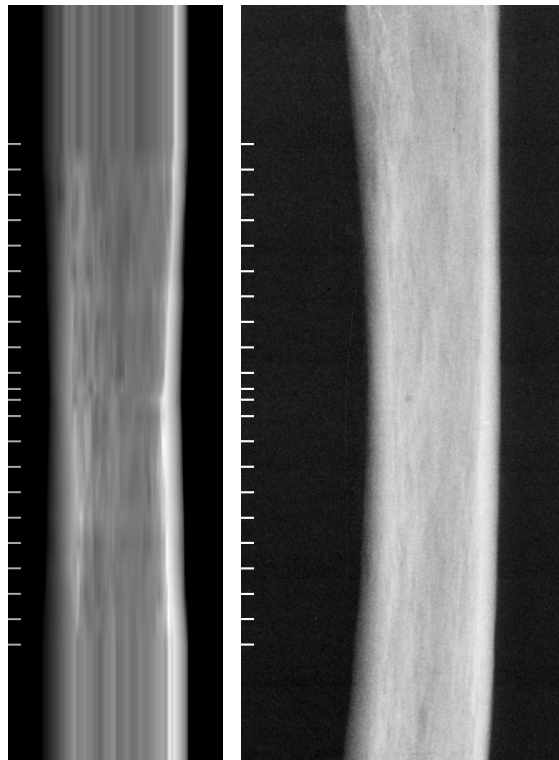
The developed simulated projection **C++** class is described in appendix E.9, page 176.

## 4.4 Results and Discussion

In this section the results achieved in chapter 4 are analysed.

### 4.4.1 Cortical Geometry Measured on a Single Bone

The mutual relations between various geometrical properties measured on a single bone are analyzed in this section.



(a) Simulated  
radius of bone  
r-s7.

(b) Real region from radius  
of bone r-s7.

Figure 4.14: Simulated radius made using slices from bone r-s7 is seen to the left. The real region extracted from the radius is seen to the right. The markings to the left are the vertical location of the slices. The pixel values at the outer ends of the simulated profile are extrapolated from the outermost slice. Note that the radial side is to the right and the ulnar side to the left.

## Graphs of Cortical Thickness

The cortical thickness measured by radiogrammetry and the cortical thickness measured on the slices are shown for each bone as a function of the distance to the fixpoint in figure C.1–C.17 on page 122–138. Cortical thickness at the radial and the ulnar side and the total slice width is also computed by radiogrammetry on the *simulated* region of the radius.

The measured values are the outer width of the bone and the ulnar and radial cortical thickness. The three different methods for measuring the cortical thickness on slices presented in section 4.1.1 are used. For the ulnar side the measurement is made where there is maximum distance from origo to the outer ulnar boundary. In figure 4.15 the radial and ulnar cortical thickness and the outer width of a bone are shown.

It is seen that there is a good agreement in the shape of the graphs, especially is the outer width measured satisfactorily. There is a bias in the results, since the cortical thickness measured by radiogrammetry tends to be higher than the thickness measured on the slices. This is examined more closely in section 4.4.2. On bone **r-s2** the radiogrammetry fails (of unknown reasons). The radial thickness is found satisfactory while the ulnar thickness and total width is not measured correctly.

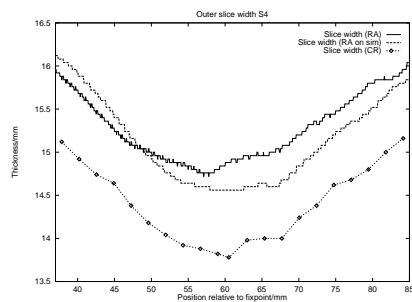
Of the three methods of measuring cortical thickness on the slices, the pixel sum method seems to be the most stable. The hit method is more sensitive for the trabeculization of the endosteal surface. On bone **r-s2, r-s9, r-s10** and others, the radial cortical thickness measured by the hit method is somewhat unstable, while the sum method is robust. The trace method is sensitive to juxtaendosteal resorption spaces. If a resorption space is considered a part of the endosteal surface, the trace method will regard the boundary of the resorption space as the inner boundary. An example of this is seen in bone **r-s9** on the radial side. The trace method calculates a less thickness than the other methods for some slices. If there is much intracortical porosity the sum method will underestimate the cortical thickness, as seen on bone **r-s23**.

The conclusion is, that the more resorption there is present in the bone, the less robust and coherent the three methods are. In a bone with no or little resorption (as in **r-s15**) there is a good agreement in the results from the three methods.

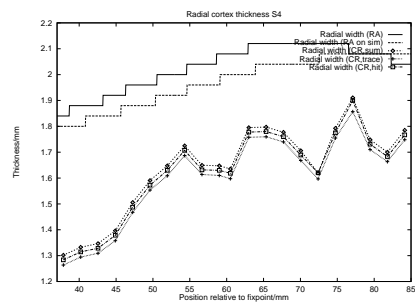
The minimum outer width is, except for bone **r-s3, r-s12, r-s22** and **r-s23**, found in the middle of the region of interest. This is satisfactory since the radiogrammetric measurements are made at this location.

## Correlation Analysis

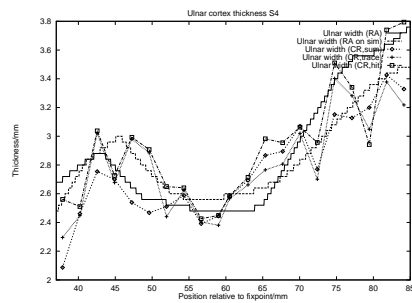
The symbols  $X_i$  and  $Y_i$  will in this section be used to denote two variables from the same *slice*. Index  $i$  denotes the slice number. As an example  $X$  could be the radial cortical thickness measured by the sum method ( $w_{\text{sum,rad}}$ ) and  $Y$  the ulnar cortical thickness measured by the hit method ( $w_{\text{hit,uln}}$ ).



(a) Outer width.



(b) Radial thickness.



(c) Ulnar thickness.

Figure 4.15: Cortical Thickness of slice r-s4.



The correlation coefficient (in the following called the correlation) between  $X_i$  and  $Y_i$  is defined as:

$$\text{cor}(X, Y) = \frac{E(X - \mu_x)(Y - \mu_y)}{\sigma_x \sigma_y} \quad (4.12)$$

, where  $\mu_x, \mu_y$  and  $\sigma_x, \sigma_y$  are the means and standard deviations, respectively, of the random variables X and Y.

For each bone the correlation between all the endpoint variables are calculated in a correlation matrix R, in which element  $r_{ij}$  is the correlation between feature  $i$  and feature  $j$ . The correlation is a measure of the linear dependency between variables and it can therefore be applied to a pair of variables with different metrics (it is generally not a good idea to compare an area with a length).

The average correlation matrix for all bones is then calculated. It is seen in table C.1–C.3, a subset, which is discussed in this section, of the results is seen in table 4.3. The radiogrammetric measurements are not used in this analysis, since the result from the radiogrammetry module is a single value representing the measurements from the whole bone. The correlation between measured endpoint values and radiogrammetry is examined in section 4.4.2.

As seen in table 4.3 the correlation between the three methods of measuring the cortical thickness is acceptable. The hit method has the lowest correlation with the other methods since it is the method that is most sensitive to trabeculization and noise. In the following the sum method is used as the reference method for measuring cortical thickness. It is the most stable even though it is sensitive to the size of the intracortical porosities.

It is interesting to note that the outer slice width does not correlate well with any other geometric measurement. The cortical area of a slice has a correlation of 0.32 to the total slice width. That indicates that the outer diameter of the bone has little influence of the bone mass at the current site of the bone.

The ulnar cortical thickness is seen to correlate better with cortical area than the radial cortical thickness. This is probably due to the fact that the ulnar thickness includes the size of the extremity on the ulnar side, which accounts for some of the cortical area.

X	Y	cor(X,Y)
$w_{\text{sum,rad}}$	$w_{\text{trace,rad}}$	0.88
$w_{\text{sum,rad}}$	$w_{\text{hit,rad}}$	0.79
$w_{\text{trace,rad}}$	$w_{\text{hit,rad}}$	0.75
$w_{\text{total}}$	$A_{\text{res}}$	0.32
$w_{\text{sum,rad}}$	$A_{\text{res}}$	0.64
$w_{\text{sum,uln,max}}$	$A_{\text{res}}$	0.77

Table 4.3: Correlation between measured endpoint variables. The values are the average correlation for all bones. The data is subset of the data seen in table C.1–C.3.

## 4.4.2 Comparison of the Cortical Geometry of all Bones

The mutual relations between various measurements on all bones are analyzed in this section. The analyzed features are single features from each bone.

The cortical thickness and area are an average of the cortical thickness and area measured on the 9 slices placed where there is minimal outer diameter.

The age of the subjects were unknown for bone **r-s1**, **r-s2** and **r-s2**. The correlation between age and the other features is calculated from the remaining 14 bones.

### Correlation Analysis

The symbols  $X_i$  and  $Y_i$  will in this section be used to denote two variables from the same *bone*. Index  $i$  denotes the bone number. As an example  $X$  could be the radial cortical thickness measured by radiogrammetry ( $w_{\text{rad,RA}}$ ) and  $Y$  the area of cortex measured on the slices ( $A_{\text{res}}$ ).

A correlation matrix is calculated, the result is seen in table C.4–C.7. A set of the correlated variables are plotted in graphs that can be seen in figure C.18–C.37 on page 148–159. Some of the endpoint variables in the correlation matrix are explained in chapter 5 and 6. In the following a subset of the results seen in table C.4–C.7 is discussed. The subset of the results is seen in table 4.4.

By examining the plots it can be concluded that the radiogrammetry module has failed on bone **r-s2**, this lowers the correlation between the measured features.

The correlation between the radial cortical thickness measured on the slices and by radiogrammetry is very satisfactory (0.94). There is a very significant bias between the measurements but they have a strong linear dependency. The bias can be due to the x-ray projection distortion as explained in section 2.2.2, p. 17, or it can be an artifact introduced because of the lack of flesh on the bones. The correlation plot can be seen in figure 4.16. The bias is tested for significance in section 4.4.2. The ulnar cortical thickness measured by radiogrammetry correlates only moderately with the thickness measured on the slices. The ulnar thickness is the most difficult to measure with radiogrammetry, due to the the shape of the extremity (margo interosseus) on the ulnar side of the bone. Consequently great care should be taken when using the ulnar cortical thickness measured by radiogrammetry as a diagnostics feature.

The total slice width measured by radiogrammetry has an acceptable correlation with the width measured on the slices (it would be higher, if slice **r-s2** was removed from the study). The uncertainty of the measurement of the outer width is also due to the variation of the shape of margo interosseus.

As expected the correlation between the radial and ulnar thickness is moderate.

The ulnar cortical thickness has a small correlation with the outer width of the slice, while the radial thickness has no correlation with the outer width. The shape of the extremity of the ulnar side of the bone (margo interosseus) influences both the total slice width and the ulnar cortical thickness. This explains partially their noticeable correlation.

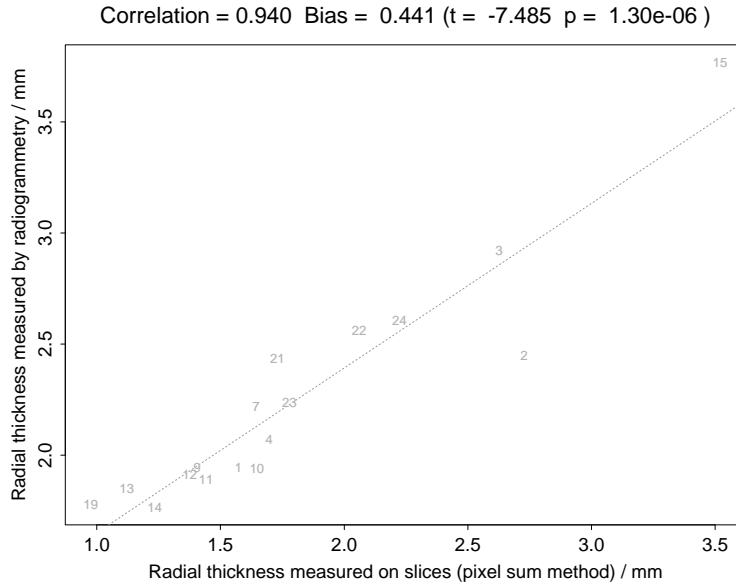


Figure 4.16: Radial thickness measured on slices and by radiogrammetry.

The cortical area correlates well with the radial thickness measured on the slices, moderately with the ulnar cortical thickness and very badly with the outer diameter of the bone. In the estimation of cortical bone mass via cortical cross-sectional area it is preferable to use the radial cortical thickness as the measured value.

The age of death of the subjects correlates well with the cortical area, which is expected since bone loss is accelerated after the menopause and all subjects have passed the menopause.

$X$	$Y$	$\text{cor}(X,Y)$
$w_{\text{sum,rad}}$	$w_{\text{rad,RA}}$	0.94
$w_{\text{sum,uln,max}}$	$w_{\text{uln,RA}}$	0.48
$w_{\text{total}}$	$w_{\text{total,RA}}$	0.71
$w_{\text{sum,rad}}$	$w_{\text{sum,uln}}$	0.56
$w_{\text{sum,rad}}$	$w_{\text{total}}$	-0.19
$w_{\text{sum,uln,max}}$	$w_{\text{total}}$	0.41
$w_{\text{sum,rad}}$	$A_{\text{res}}$	0.89
$w_{\text{rad,RA}}$	$A_{\text{res}}$	0.80
$w_{\text{sum,uln,max}}$	$A_{\text{res}}$	0.65
age	$A_{\text{res}}$	-0.76

Table 4.4: Correlation between features measured on the bones. The cortical thickness and area are an average of the cortical thickness and area measured on the 9 slices placed where there is minimal outer diameter. The data is subset of the data seen in table C.4–C.7 and the corresponding graphs are shown in figure C.18–C.37.

## Estimation of Bias

When two values of the same phenomenon is compared (as an example the radial thickness measured on slices and by radiogrammetry) a bias can be calculated. If one of the method can be regarded as a reference method the calculated bias is an estimation of the accuracy of the other method.

The bias is calculated as the mean of the differences of the features:

$$\bar{D} = \frac{1}{N} \sum_{i=0}^{N-1} D_i \quad (4.13)$$

, where  $D_i = X_i - Y_i$ .

The significance of the bias is tested by performing a paired t-test. Here it is assumed that [18, p.310–311]:

$$X_i \in N(\mu_i, \sigma_1^2) \quad (4.14)$$

$$Y_i \in N(\mu_i + \delta, \sigma_2^2) \quad (4.15)$$

,where  $\mu_i$  is the real value of the measured parameter for bone  $i$ . The parameter,  $\delta$  which is independent of the bone measured, is the bias of the used method.  $X_i$  is the values measured by the reference method.

From equation 4.13 we have

$$D_i \in N(\delta, \sigma_1^2 + \sigma_2^2) = N(\delta, \sigma^2) \quad (4.16)$$

$D_i$  is only dependent of the bias of the examined method.

So the test is

$$H_0 : \delta = 0 \quad \text{against} \quad H_1 : \delta \neq 0 \quad (4.17)$$

The test value is:

$$t = \frac{\bar{D}\sqrt{n}}{\sqrt{\sum(D_i - \bar{D})^2/(n-1)}} \quad (4.18)$$

, which is  $\in t(n-1)$  under  $H_0$ .

The p-value is the level of significance for which the observed test statistics value lies on the boundary between acceptance and rejection of the null hypothesis.

The results are shown in table 4.5 and they may be summarized as follows:

- The null hypothesis for the bias of the radial cortical thickness measured by radiogrammetry and on the slices is rejected for all levels greater than  $1.30e - 6$ .
- The null hypothesis for the bias of the ulnar cortical thickness measured by radiogrammetry and on the slices is rejected for all levels greater than 0.055.
- The null hypothesis for the bias of the total slice width measured by radiogrammetry and on the slices is rejected for all levels greater than 0.00118.

$X$	$Y$	$\text{cor}(X,Y)$	$\bar{D}/mm$	t	p
$w_{\text{sum,rad}}$	$w_{\text{rad,RA}}$	0.94	0.44	-7.48	1.30e-6
$w_{\text{sun,uln,max}}$	$w_{\text{uln,RA}}$	0.48	0.35	-2.07	0.055
$w_{\text{total}}$	$w_{\text{total,RA}}$	0.70	0.88	-3.94	0.00118

Table 4.5: Correlation between measured variables. The estimated bias  $\bar{D}$  and the significance of the bias.

## Chapter 5

# Measuring Endosteal Resorption

Endosteal resorption is characterized by irregularity of the inner boundary of the cortical shell.

In this thesis the endosteal surface is defined as the outer boundary of the medullary area of the bone. This definition is ambiguous since two processes has influence on the shape of the boundary, namely endosteal resorption and juxtaendosteal resorption. As explained in section 4.1.1, p. 46 a juxtaendosteal resorption space is considered as a part of the medullary area if there is a communication between the two. In figure 5.2(a) a part of a slice with a juxtaendosteal resorption space present is seen. After thresholding and isolation of the largest connected component the juxtaendosteal resorption space is considered as a part of the medullary area as seen in figure 5.2(b).

In this section methods of quantifying the smoothness of the endosteal surface is presented. In figure 5.1 a flowchart of the analysis is seen.

### 5.1 Tracing the Endosteal Surface

On a contact radiograph the endosteal surface of the bone is represented by the inner boundary of the cortical shell. As a shape description of the endosteal surface the traced inner boundary is used. It is traced as described in section 4.1.1, p. 46. The traced inner boundary of a part of a slice is seen in figure 5.2(c).

The traced inner boundary is represented by a vector of  $m$  points  $s_0, \dots, s_{m-1}$ .

From the tracing of the endosteal surface a feature that describes the boundary can be derived:

**Arclength** The arclength  $L_{a,\text{traced}}$  of the traced boundary  $L_{a,\text{traced}} = \sum_{i=1}^{m-1} \|s_i - s_{i-1}\|$ .

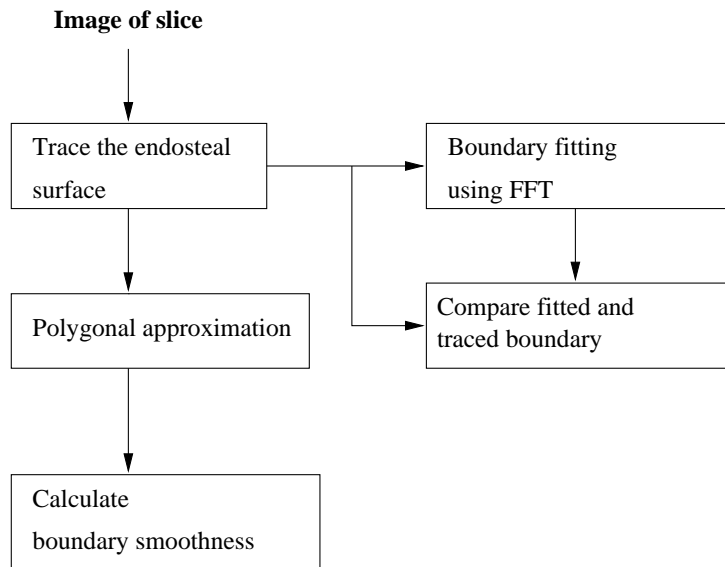


Figure 5.1: The algorithms used in the analysis of the endosteal resorption. The tracing of the endosteal surface is explained in section 5.1. Polygonal approximation is explained in section 5.2. Boundary smoothness is explained in section 5.3. Boundary fitting is explained in section 5.5. The comparison of the fitted and traced boundary is done in section 5.5.1.

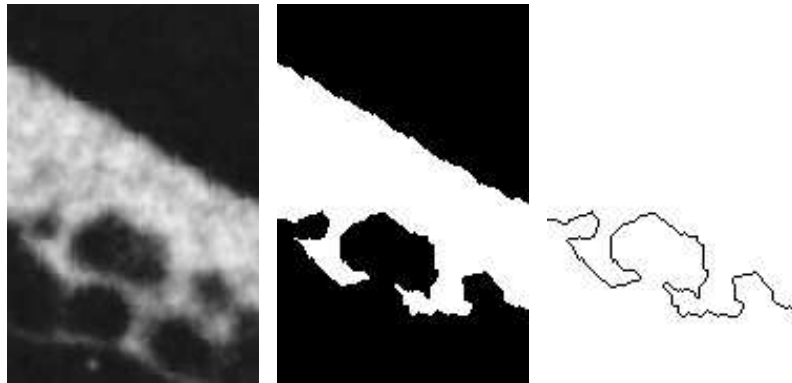
In the next section a method for simplification of the traced boundary is explained.

## 5.2 Polygonal Approximation

The traced boundary from the previous section has a high number of nodes, therefore there is a need for a simplification of the boundary. In this section a polygonal fitting algorithm is presented. The result of the algorithm is a vector of points. The full description of the algorithm can be found in [30, p.281–292].

### 5.2.1 A Suboptimal Line Fitting Algorithm

A group of points is approximated by a line, which is the line going through the two endpoints of the group. All points in the set is examined, and if a point in the set has a distance from the fitting line greater than a given value, two new lines are formed. As seen in figure 5.3 a fitting line from point A to point B is examined. The distance from point C to the line is greater than the maximum allowed distance and therefore two lines are formed, one from point A to point B and one from point B to point C. This process is recursively repeated until no point in the set has a greater distance than the allowed to the fitting line.



(a) A part of slice  $r-s1-20$ . A juxtaendosteal resorption space is seen.

(b) A part of the thresholded version of slice  $r-s1-20$ .

(c) The traced inner boundary of a part of slice  $r-s1-20$ .



(d) The polygonal approximation of the endosteal boundary.

Figure 5.2: A juxtaendosteal resorption space seen in a part of slice  $r-s1-20$ . After the thresholding the juxtaendosteal resorption area is considered as a part of the medullary area.



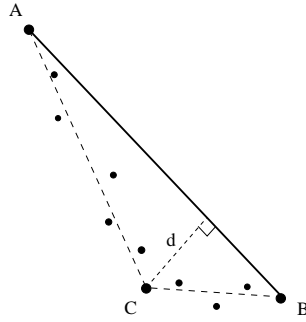


Figure 5.3: A set of points and the fitting line. The distance  $d$  from point C to the line is greater than the maximum allowed distance and therefore two lines are formed, one from point A to point B and one from point B to point C.

### 5.2.2 A Simple Polygon Fitting Algorithm

The line fitting algorithm is used in a polygon fitting algorithm. The algorithm examines groups of point for collinearity and keeps track of the returned fitting line. When two fitting lines have been found the mutual angle is calculated. If the mutual angle between the two lines are smaller than a given value the two lines are merged together as one. As seen on figure 5.4 where line 1 from point A to point B and line 2 from point B to point C is merged together as one line from A to C since the angle  $\theta$  is smaller than the given value (note that the angle shown in the image is exaggerated).

The result of the polygonal fitting algorithm is a vector of  $n$  points  $p_0, \dots, p_{n-1}$ .

### 5.2.3 Results and Discussion

In figure 5.2(d) the polygonal approximation of the boundary seen in figure 5.2(c) is seen. It is seen that the polygonal approximation gives a robust boundary description with a smaller number of nodes than the traced boundary. In this thesis the minimum distance is  $d = 1.0$  and the minimum mutual angle is  $\theta_{\min} = 5^\circ$ .

From the polygonal fit two features describing the boundary can be derived:

**Arclength** The arclength  $L_{a,\text{poly}}$  of the fitted boundary  $L_{a,\text{poly}} = \sum_{i=1}^{n-1} \|p_i - p_{i-1}\|$ .

**Points** The number of points (nodes) of the polygonal approximation of the boundary.

The prototype for the algorithm is seen in appendix E.4.

## 5.3 Boundary Smoothness

A measure of the smoothness of a line is the second derivative. The boundary  $b$  is represented by a vector of  $n$  points  $p_0, \dots, p_{n-1}$  connected by vertices. The

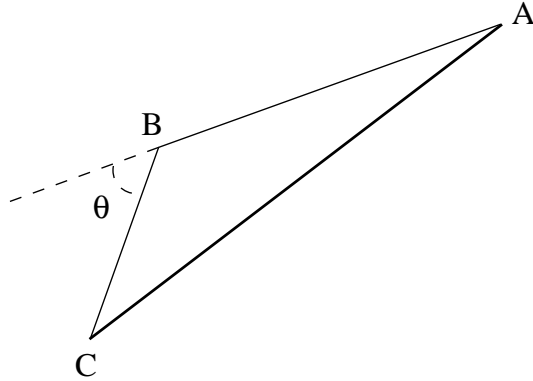


Figure 5.4: If the angle between two lines are smaller than a given value the two lines are merged together as one. Here line 1 from point A to point B and line 2 from point B to point C is merged together as one line from A to C since the angle  $\theta$  is smaller than a given value (note that the angle is exaggerated).

boundary representation is found by polygonal approximation as explained in section 5.2. From standard finite difference technique the approximation of the second derivative become:

$$b'' = p_{i-1} - 2p_i + p_{i+1} \quad (5.1)$$

The smoothness feature of the boundary is measured as the sum of squares of the second derivative:

$$S = \oint \|b''\|^2 \quad (5.2)$$

$$\approx \sum_{i=1}^{n-2} \|p_{i-1} - 2p_i + p_{i+1}\|^2 \quad (5.3)$$

The shape feature used in the shape analysis is:

**Smoothness** The boundary smoothness represented as the sum of squares of the second derivative of the polygonal approximation of the boundary  $S = \oint \|b''\|^2$ .

The prototype for the algorithm can be seen in appendix E.3.

## 5.4 Bending Energy

A definition of bending energy is found in [23, p. 203]. The bending energy is equivalent to the force necessary to bend a stiff object into the desired shape.

For each point on the boundary  $p_i$  the angle  $\theta_i$  is calculated as the angle between the line connecting the points  $p_{i-1}$  and  $p_i$  and the line connecting the points  $p_i$  and  $p_{i+1}$ .

The bending energy is defined as:

$$\text{BE} = \frac{1}{L_a} \sum_{i=0}^{N-1} \theta_i^2 \quad (5.4)$$

Where  $L_a$  is the arclength of the boundary.

The used boundary representation is the polygonal approximation as explained in section 5.2.

This feature is not used in the analysis since the boundary smoothness presented in the previous section proved to be superior.

## 5.5 Boundary Fitting Using the Fast Fourier Transform

A method of measuring the roughness of a line is to compute a smooth version of the line and compare it with the original. In this section a boundary description of the inner boundary is fitted by trigonometric functions by a fast Fourier transform.

The boundary description is the polar coordinates of the inner boundary sampled at a discrete set of angles (as described in section 3.5.3, p. 39, but with the inner boundary). The polar coordinate system is described in section 3.5.1, p. 36, the only difference is that origo is the center of mass of the traced inner boundary.

The points used in the analysis are found by calculating the interception of a line from the center of mass with the given angle and the traced inner boundary. Since the line can cross the boundary several times the interception point farthest away from origo is used.

A boundary description of the inner boundary seen in figure 5.5(a), is seen in figure 5.5(b). The outer boundary description is also seen in the graph.

The number of samples of the inner boundary is denoted  $N$ . The distance measured at angle  $\theta = \frac{k \cdot 360^\circ}{N}$  is denoted  $d_k$ . Since the distance series shall be used in a fast Fourier transform,  $N$  must be a power of 2. In this thesis  $N = 2^{10} = 1024$

The fast Fourier transform as described in [32, p. 496–510] has been implemented.

The Fourier transform is given as

$$D_n = \sum_{k=0}^{N-1} d_k e^{2\pi i k n / N}, \quad n = 0, \dots, N-1 \quad (5.5)$$

$D_n$  is the complex amplitude of the signal at frequency  $f_n = \frac{n}{N\Delta}$ . Where  $\Delta$  is the sampling interval which in this case is measured in degrees  $\Delta = \frac{360^\circ}{N}$ . The fourier transform maps the  $N$  numbers (the  $d_k$ 's) into  $N$  complex numbers (the  $D_n$ 's).

To apply a bandpass filter to the signal, the amplitude of the Fourier signal in a certain range is kept and all others are set to zero and the inverse transform is calculated.

$$D_n = 0, \quad b_l < n < b_h \quad (5.6)$$

, here  $b_l$  and  $b_h$  is the index of the low and high frequencies of the bandpass filter.

The formula for the discrete inverse Fourier transform which recovers the set of  $d_k$ 's exactly from the  $D_n$ 's is:

$$d_k = \frac{1}{N} \sum_{n=0}^{N-1} D_n e^{-2\pi i k n / N} \quad (5.7)$$

The result of the inverse Fourier transform is the bandpass filtered inner boundary description. In this thesis the filter used is a lowpass filter, where the frequency range kept is  $D_n$  where  $n \in [0, 6]$ .

### 5.5.1 Shape Features

For each point  $p_i$  in the traced inner boundary the distance  $r_i$  to the point in the fitted boundary with the same angle in the polar coordinate system is calculated. A residual  $\mathbf{r}$  vector consisting of these distances is created. On figure fig 5.6 the distance from a point on the traced boundary to the fitted boundary is seen.

The number of points of the traced boundary is  $N_t$ . The average residual value is:

$$\bar{r} = \frac{1}{N_t} \sum_{i=0}^{N_t-1} r_i \quad (5.8)$$

The shape features used in the shape analysis are:

**Mean residual** The average of the residuals,  $\bar{r}$ . The residuals are the distances between the traced boundary and the fitted boundary.

**Max residual** The maximum residual,  $\max(r)$ .

**Quantiles of the residual** A given quantile of the residuals (in this thesis the 95% quantile is used).

**Arclength fraction** The arclength of the traced inner boundary divided by the arclength of the fitted inner boundary  $\frac{L_{a, \text{traced}}}{L_{a, \text{fit}}}$ .

Fits of the inner boundary of a slice have been generated with different bandpass filter values. As seen in figure 5.7–5.10 the fit approximates the boundary better the more frequencies used.

The wanted boundary fit, is a fit that models the inner boundary but not the endosteal resorption spaces. Therefore a lowpass filter is used. In this thesis

a filter with highest frequency  $b_h = 6$  is used. The cutoff frequency is chosen based on the visual properties.

If the frequency of the endosteal resorption spaces were known a measure of the roughness of the inner boundary could be the summed powerspectrum of the frequencies of the endosteal resorption. This measure is not used since tests showed that the arclength fraction feature proved to be superior.

The power spectrum is estimated by

$$P(f_k) = |D_k|^2 \quad k = 1, 2, \dots, \left(\frac{N}{2} - 1\right) \quad (5.9)$$

The C++ class `CFourFeature` is explained in appendix E.10.

## 5.6 Results and Discussion

### 5.6.1 Comparison of Shape Features from All Bones

The mutual relations between various measurements on all bones are analyzed in this section. The analyzed features are single features from each bone.

The shape features are an average of the features calculated on all slices in the bone.

#### Scalloping Measured by Radiogrammetry

The radiogrammetric module developed at Torsana Osteoporosis Diagnostics calculates a scalloping measure. The measured value is a combination of the quantity of endosteal, juxtaendosteal, intracortical and periosteal resorption. In the following the measured scalloping is denoted **scalloping**.

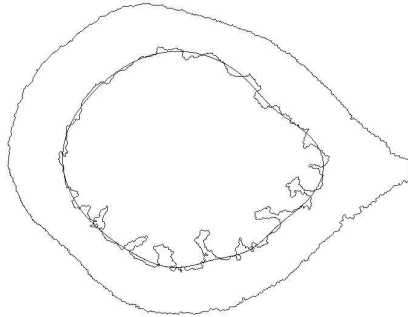
During the project period there has been some confusion regarding the term *scalloping*. Some people, including the author, have thought that scalloping was endosteal resorption, therefore the features that are compared to the scalloping measured by radiogrammetry are measures of the endosteal resorption.

If the definition of scalloping used in the radiogrammetric module should have been followed strictly, the values to be compared should be a combination of all types of resorption.

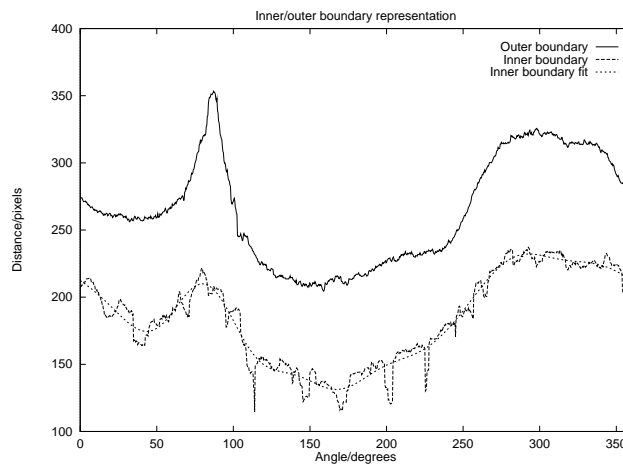
Under the assumption that there is a high correlation between endosteal resorption and intracortical resorption, this misinterpretation will not seriously degrade the results.

#### Bone Status Assessed by Visual Inspection of Radiographs

A subjective bone status measure has been generated for all bones by visual inspection. The gallery of slices seen in appendix B was presented to 4 persons. Each bone was classified to have a scalloping rating from 0 (no scalloping) to 10 (very scalloped). In the following the subjective bone status is denoted **status**.



(a) The inner and outer boundaries of slice **r-s1-14**. The fit to the inner boundary is also seen ( $N = 1024$ . Lowpass filtered  $n \leq 6$ ).



(b) The boundary description of slice **r-s1-14**. The fitting line for the inner boundary is also seen.

Figure 5.5: The boundaries of slice **r-s1-14** (a). The boundary shape description (b).

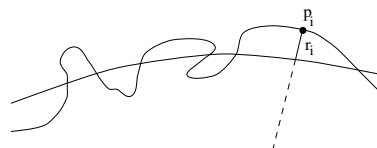


Figure 5.6: The distance  $r_i$  from a point  $p_i$  on the traced boundary to the fitted boundary.

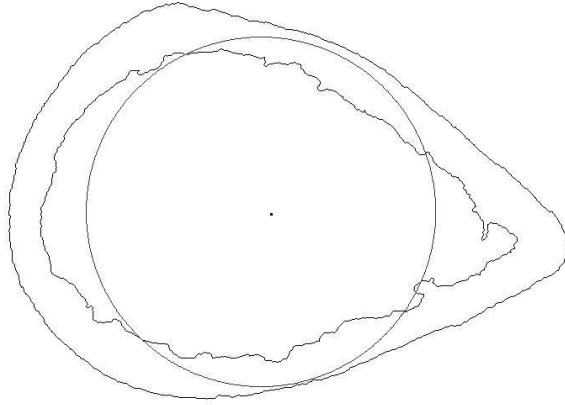


Figure 5.7: The fit of the inner boundary shown with the traced boundaries.  $N = 1024$ . Lowpass filtered  $n \leq 1$  (only the dc value). The point in the middle is the center of mass of the inner boundary. Slice r-s19-05.

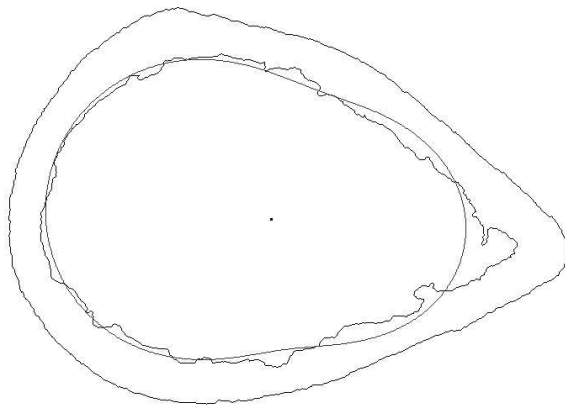


Figure 5.8: The fit of the inner boundary shown with the traced boundaries.  $N = 1024$ . Lowpass filtered  $n \leq 2$ . The point in the middle is the center of mass of the inner boundary. Slice r-s19-05.

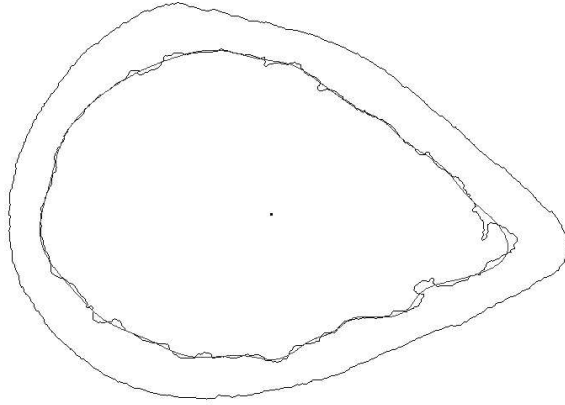


Figure 5.9: The fit of the inner boundary shown with the traced boundaries.  $N = 1024$ . Lowpass filtered  $n \leq 15$ . The point in the middle is the center of mass of the inner boundary. Slice r-s19-05.

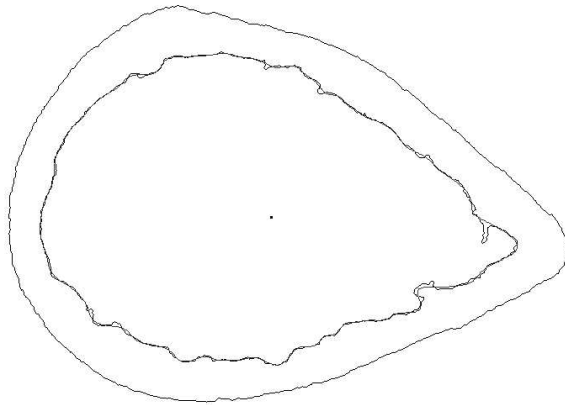


Figure 5.10: The fit of the inner boundary shown with the traced boundaries.  $N = 1024$ . Lowpass filtered  $n \leq 40$ . The point in the middle is the center of mass of the inner boundary. Slice r-s19-05.



## Correlation Analysis

The symbols  $X_i$  and  $Y_i$  will in this section be used to denote two variables from the same *bone*. Index  $i$  denotes the bone number.

A correlation matrix is calculated, the result is seen in table C.4–C.7. A set of the correlated variables are plotted in graphs that can be seen in figure C.18–C.37 on page 148–159. In the following a subset of the results seen in table C.4–C.7 is discussed. The subset of the results is seen in table 5.1.

As a measure of the scalloping of the slices the boundary arclength fraction feature found by the FFT-fit is used. In the following it is called the arclength fraction or just the scalloping measured on the slices.

The scalloping measured on the slices has a good correlation with the subjective bone status (0.90) (as seen in figure 5.11) while scalloping measured on *ordinary* radiographs correlates very badly with the subjective bone status (0.26). The subjective bone status is based on visual inspection of the slices and therefore it is natural that the scalloping measured on the slices has the good correlation while the scalloping measured by radiogrammetry correlates badly. On the other hand, is the scalloping measured by radiogrammetry supposed to give an impression of the scalloping in the bone, and therefore great care should be taken when scalloping is used as a diagnostic tool.

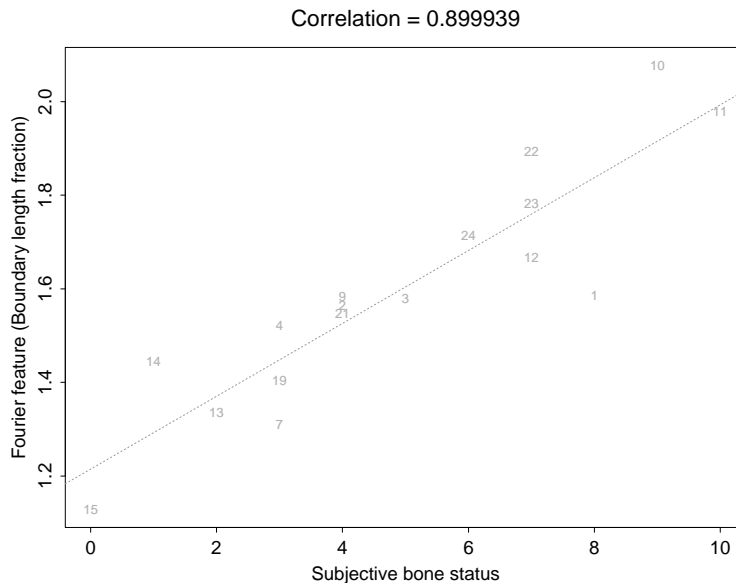


Figure 5.11: Subjective bone status and fourier feature (arclength fraction) measured on slices.

The correlation between the scalloping measured on the slices and the scalloping measured by radiogrammetry is not satisfactory (0.37). The reason could be that the radiogrammetric method measures both the intracortical porosity in the anterior and posterior sections of the cortical shell and the scalloping of

the endosteal surface. The scalloping measured on the slices quantifies only the endosteal resorption and not the intracortical porosities.

The age does not have a good correlation with any of the shape features. This is an indication of that scalloping contrary to bone loss is subject based and not age based. To prove this, a much larger study is needed.

While there is no correlation (0.007) between the scalloping measured on the slices and the area of the cortical shell, there is a correlation of -0.53 between the area of the cortical shell and the scalloping measured by radiogrammetry. This indicates that the radiogrammetric method is not as independent of the geometric properties of the bone as it is supposed to be.

$X$	$Y$	$\text{cor}(X,Y)$
$A_{\text{res}}$	scalloping	-0.53
status	$\frac{L_{a,\text{fit}}}{L_{a,\text{traced}}}$	0.90
status	scalloping	0.26
age	scalloping	0.21
age	$\frac{L_{a,\text{fit}}}{L_{a,\text{traced}}}$	0.16
$\frac{L_{a,\text{fit}}}{L_{a,\text{traced}}}$	scalloping	0.37

Table 5.1: Correlation between shape features measured on the bones. The shape features are an average of the features calculated on all slices in the bone. The data is subset of the data seen in table C.4–C.7 and the corresponding graphs are shown in figure C.18–C.37.

## Chapter 6

# Measuring the Endosteal Resorption Area

In this section the area of the bone that is occupied by endosteal resorption spaces is used as a measurement of the quantity of endosteal resorption.

Resorption spaces are classified as endosteal resorption if there is a communication between the resorption space and the medullary area.

The outer boundary of the resorption area is found with a special type of an active shape model, and active net.

Active nets have also been tested in the extraction of the inner boundary of the endosteal surface, but it proved that a more simple active contour was more robust.

In the next sections active nets and active contours are explained.

### 6.1 Active Nets

An active net is a special kind of a deformable template used for location and extraction of objects in noisy images. Active nets and its 3D equivalence active cubes have been described in [13],[14] where they are used for segmentation of objects in 3D data sets acquired by Computed Tomography (CT). In this thesis the 2D Active Net described in [13] is conceived as a lattice of nodes connected by springs.

#### 6.1.1 Matrix Representation

An active net is defined as a matrix  $\mathbf{A}$  with dimensions  $M \times N$  where element  $a_{ij} = (r(i, j), c(i, j))$  is a position in the image. The nodes of the net is described by the points in  $\mathbf{A}$ , so node  $(i, j)$  has position  $a_{ij}$  in the image.

Each node is connected to its 4 neighbours by a spring. Nodes in the middle of the net have four springs attached, boundary nodes three and corner nodes

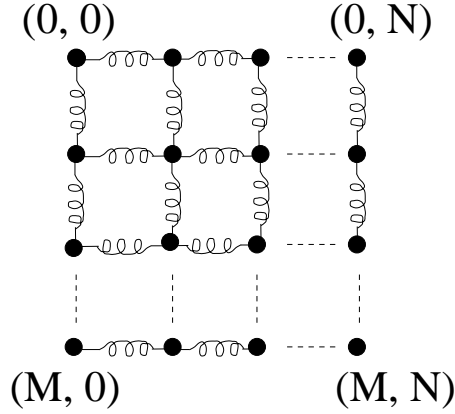


Figure 6.1: The physical model of the active net. Nodes are connected to their neighbours with springs.

have two neighbours as seen in figure 6.1. The spring connecting node  $(i, j)$  and  $(k, l)$  is denoted  $s_{(ij,kl)}$

### 6.1.2 Internal Energy

The spring energy of a node in the net is defined as the sum of the potential energies of the springs attached to the node.

$$E_{\text{spring}}(i, j) = \sum_{(k,l) \in N_4(i,j)} E_{\text{pot}}(s_{(ij,kl)}) \quad (6.1)$$

, where  $N_4(i, j)$  is the 4-neighbourhood of point  $(i, j)$ .

The force of a spring is given by Hookes law

$$F = k x \quad (6.2)$$

, where  $x$  is the length of the spring and  $k$  is a material constant [3]. The potential energy of the spring is  $E_{\text{pot}} = \frac{1}{2} k x^2$ . In the following the material constant  $k$  is neglected. In the matrix representation of the net, the potential energy of spring  $s_{(ij,kl)}$  is given as:

$$E_{\text{pot}}(s_{(ij,kl)}) = \|a_{ij} - a_{kl}\|^2 \quad (6.3)$$

To ensure smoothness and rigidity of the net a smoothness term is introduced. From standard finite difference technique the smoothness term become.

$$E_{\text{smooth}}(i, j) = \|a_{i-1j} - 2a_{ij} + a_{i+1j}\|^2 \quad (6.4)$$

$$+ \|a_{ij-1} - 2a_{ij} + a_{ij+1}\|^2 \quad (6.5)$$

$$+ 2 \|a_{i-1j} - a_{i-1j+1} - a_{ij} + a_{ij+1}\|^2 \quad (6.6)$$

The internal energy of a node is defined as the sum of the spring energy and the smoothness energy:

$$E_{\text{int}}(i, j) = \alpha E_{\text{spring}}(i, j) + \beta E_{\text{smooth}}(i, j) \quad (6.7)$$

,here  $\alpha$  and  $\beta$  are coefficients controlling the first and second order smoothness of the net.

### 6.1.3 External Energy

The external energy of a node is defined as external forces acting on the node. In this context the external energy is the pixel value at the node position plus the pixel values of the neighbour nodes weighted by their inverse distance.

$$E_{\text{ext}}(i, j) = \omega I(a_{ij}) + \rho \sum_{(k,l) \in N(i,j)} \frac{1}{\|a_{ij} - a_{kl}\|} I(a_{kl}) \quad (6.8)$$

, here  $I(a_{ij})$  is the image intensity at point  $a_{ij}$ . The image intensity is normally not the intensity in the original image but, the intensity in a preprocessed version of it. There is good sense in having two different input images each representing different features of the input image. Since the energy is a positive function of the image intensity, nodes are attracted to dark areas and repulsed from bright areas. If a dark object on a bright background is wanted for extraction, a good choice of input images could be that the energy of the internal nodes is based on a mean filtered version of the original image while the energy of the external nodes<sup>1</sup> is based either on an edge filtered version or an inverted version of the input image.

$$I(a_{ij}) = \begin{cases} I_{\text{mean}}(a_{ij}) & \text{for internal nodes} \\ I_{\text{invert}}(a_{ij}) & \text{for external nodes} \end{cases}$$

The reason that the neighbour nodes' image values are added to the energy of a node is that it allows image information to propagate through the net. This energy is according to [13] suggested by Yoshino and Kawashima in an Asian conference paper.

The total energy of the net is given as:

$$E_{\text{total}} = \sum_{(i,j) \in M \times N} E_{\text{int}}(i, j) + E_{\text{ext}}(i, j) \quad (6.9)$$

### 6.1.4 Energy Minimization

With the global and local energies defined a method for minimizing the energy is needed. An improved version of the brute force greedy algorithm is used, the method is adapted from [13]. Each node is visited in turn and the local energy

$$E_{\text{local}}(i, j) = E_{\text{int}}(i, j) + E_{\text{ext}}(i, j) \quad (6.10)$$

is minimized by moving the node to the pixel position in the 8-neighbourhood of the node that has the minimum energy.

Two improvements are added to the greedy algorithm. The first improvement is derived from the Iterated Conditional Modes algorithm and gives that the

---

<sup>1</sup>External nodes are nodes on the boundary of the net and corner nodes. Internal nodes are the nodes not on the boundary.

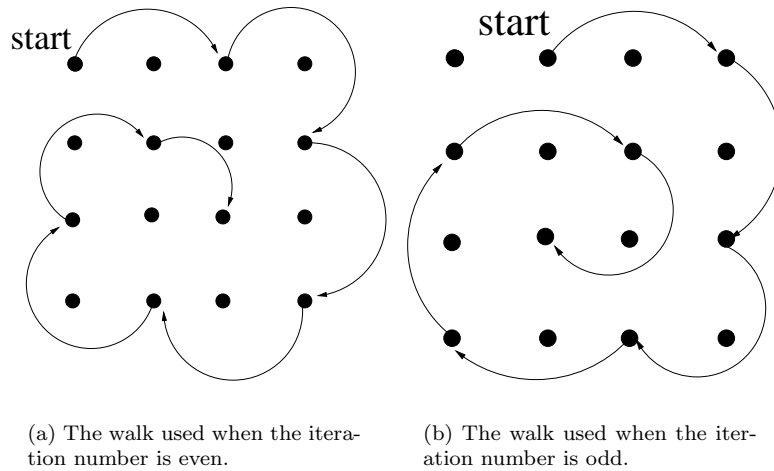


Figure 6.2: The walks used when minimizing the energy of the net.

nodes are visited in spiral manner inwards from the boundary jumping over every other node in each ring. A walk  $(i, j) = \mathbf{w}(n)$  is defined for the nodes. In this study two walks are used, one for odd iteration numbers and one for even. On figure 6.2(a) and 6.2(b) the two walks are shown, with  $M \times N = 4 \times 4$ .

The second improvement is inspired by Simulated Annealing. A node that is not moved during a visit, is moved with probability  $p$  to a randomly selected position in the 8-neighbourhood of the node. This could prevent nodes from falling in local minima.

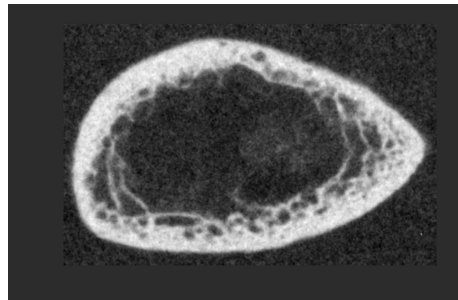
### 6.1.5 Results and Discussion

On figure 6.3(a) a slice is seen. On figure 6.3(b) the image used for internal node energy is seen (black = 0, white = 255). The image used for the external nodes are the inverse of the same figure. The medullary area is found by the method explained in section 4.1.1, p. 47.

This will cause the internal nodes to contract in the inside of the object while the outer nodes prefer to stay on the outside. The initial active net configuration is seen in figure 6.4(a). After 300 iteration the net has changed configuration but not reached minimal energy as seen in figure 6.4(b). The final shape of the active net can be seen in figure 6.4(c).

The net locates the outer boundary of the endosteal resorption area well and the intracortical porosities are outside the net as they should be. The result is satisfactory.

A C++ class CAnet has been developed. It is explained in appendix E.11.1.

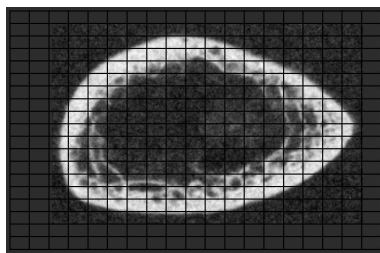


(a) Slice  $r-s11-03$ .

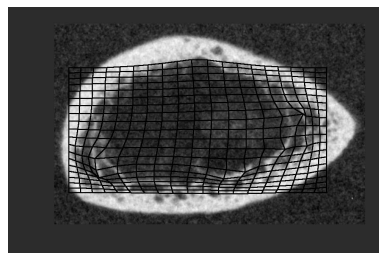


(b) The inner hole of  $r-s11-03$ . Used for calculating the internal and external node energies in the active net.

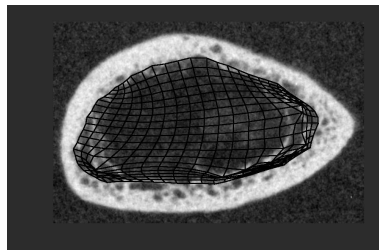
Figure 6.3: Slice  $r-s11-03$  and its medullary area used when calculating energies for the active net.



(a) The initial position of the active net.



(b) The active net after 300 iterations.  $\alpha = 4, \beta = 15, \omega = 30, \rho = 1, p = 5\%$ .



(c) The active net after 1500 iterations.  $\alpha = 4, \beta = 15, \omega = 30, \rho = 1, p = 5\%$ .

Figure 6.4: The active net locates the outer boundary of the endosteal resorption area of slice r-s11-03.



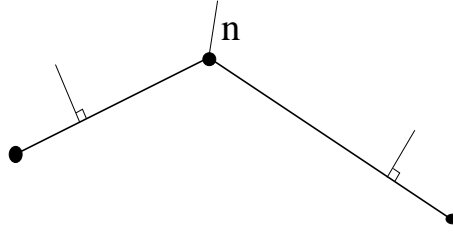


Figure 6.5: The normal of a node.

## 6.2 Active Nets Used as a Balloon Model

Instead of having a net contracting around a given object another method is developed and tested. The basic idea is that the net is initialized inside the given object and inflated until the borders are reached or the physical model reaches an equilibrium state.

A very simple approach is to reverse the sign of the coefficient  $\alpha$  that controls the contraction of the net. This causes the net to expand instead of contract, since the optimal position of the nodes will be infinitely away from each other. This method proved to be very unstable and required much fine tuning of the parameters for every image. Instead another physical model is tried.

### 6.2.1 Spring Force and Inflation Force

Another measure of internal node energy have been tested, it is inspired by [4].

The spring force exerted on node  $(i, j)$  by the spring linking node  $(i, j)$  and  $(k, l)$  can be expressed as  $\mathbf{r}_{((i,j),(k,l))} = a_{kl} - a_{ij}$ . The total spring force  $\mathbf{g}_{ij}$  a node receives is the vector sum of spring forces from all springs attached to it.

$$\mathbf{g}_{ij} = \sum_{(k,l) \in N_4(i,j)} \mathbf{r}_{((i,j),(k,l))} \quad (6.11)$$

To make the net expand, an inflating force is applied to the external nodes of the net. The inflation force a node receives takes the form of:

$$\mathbf{h}_{ij} = \gamma \mathbf{n}_{ij} \quad (6.12)$$

,where  $\gamma$  is the amplitude of the force and  $\mathbf{n}$  is the direction normal of the node. The direction normal is the average of the two normals from the two neighbours of the node as seen in figure 6.5. For internal nodes the inflating force is set to zero.

### 6.2.2 Internal Energy of the Balloon model

The total force acting on a node is the vector sum of the total spring force and the inflation force:

$$\mathbf{t}_{ij} = \mathbf{g}_{ij} + \mathbf{h}_{ij} \quad (6.13)$$

The potential energy of a node is defined as the potential energy of the total force acting on the node:

$$E_{\text{pot}}(i, j) = \|\mathbf{t}_{ij}\|^2 \quad (6.14)$$

The internal energy of a node is:

$$E_{\text{int}}(i, j) = \alpha E_{\text{pot}}(i, j) + \beta E_{\text{smooth}}(i, j) \quad (6.15)$$

, where the smoothness term is the same as the active nets smoothness term (equation 6.4.)

### 6.2.3 Results and Discussion

On figure 6.6(a) a slice is seen. On figure 6.6(b) the image used for internal node energy is seen. The image used for the external node energy is the inverse of the same figure. The initial active balloon configuration is seen in figure 6.7(a). After 200 iteration the balloon has changed configuration but not reached minimal energy as seen in figure 6.7(b). The final shape of the balloon can be seen in figure 6.7(c).

The results are not very satisfactory. The balloon model is box shaped since it is inherited from the active net, but it would be more obvious if it was circular. A circular net has been tested. The major change is that the smoothness term should not be calculated row and column wise. Instead the smoothness of each *ring* of the matrix is calculated. It proved very difficult to find parameters that would make the balloon work on all images.

The balloon model is not used further in this analysis even though it has some promising features.

A more simple active contour is developed. It is explained in the next section.

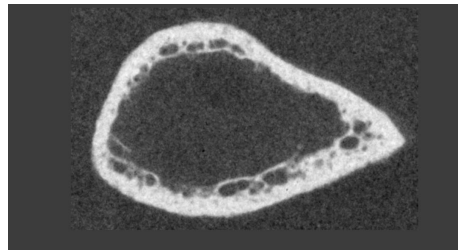
A C++ class CBalloon has been developed. It is explained in appendix E.11.2.

## 6.3 The Active Contour

In this section another type of an active shape model is used. It is a ring of nodes, where each node is connected to its two neighbours by a spring. On each node a blowforce is exerted, which will make the contour expand until an equilibrium state is reached.

### 6.3.1 Vector Representation

An active contour is represented as a vector  $\mathbf{C}$  of  $N$  nodes, each having a position in the image. Each node is connected to its two neighbours by a spring.

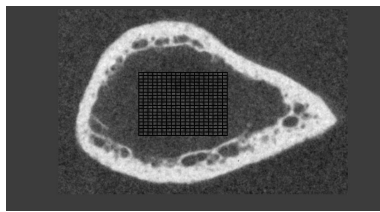


(a) Slice  $r-s14-03$ .

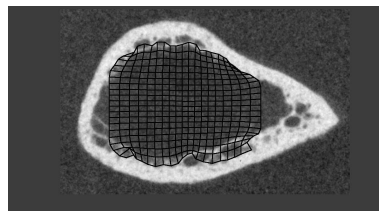


(b) The inner hole of  $r-s14-03$ . Used for calculating the internal and external node energies in the active balloon.

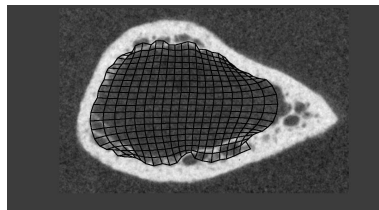
Figure 6.6: Slice  $r-s14-03$  and its medullary area used when calculating the energies in the active balloon.



(a) The initial position of the active balloon.



(b) The active balloon after 200 iterations.  $\alpha = 4, \beta = 15, \omega = 30, \rho = 1, p = 5\%, \gamma = 70$ .



(c) The active balloon after 1500 iterations.  $\alpha = 4, \beta = 15, \omega = 30, \rho = 1, p = 5\%, \gamma = 70$ .

Figure 6.7: The active balloon locates the inner boundary of the endosteal resorption area of slice r-s14-03.

### 6.3.2 Spring Force and Inflation Force

The spring force exerted on node  $i$  by the spring linking node  $i$  and  $j$  can be expressed as  $\mathbf{r}_{i,j} = c_i - c_j$ . The total spring force  $\mathbf{g}_i$  a node receives is the vector sum of spring forces from all springs attached to it:

$$\mathbf{g}_i = \sum_{j \in N_2(i)} \mathbf{r}_{i,j} \quad (6.16)$$

, where  $N_2(i)$  is the two neighbour nodes of node  $i$ .

To make the contour expand an inflating force is applied to the nodes of the contour. The inflation force a node receives takes the form of:

$$\mathbf{h}_i = \gamma \mathbf{n}_i \quad (6.17)$$

,where  $\gamma$  is the amplitude of the force and  $\mathbf{n}$  is the direction normal of the node. The direction normal is the average of the two normals from the two neighbours of the node as seen in figure 6.5.

### 6.3.3 Internal Energy of the Contour

The total force acting on a node is the vector sum of the total spring force and the inflation force:

$$\mathbf{t}_i = \mathbf{g}_i + \mathbf{h}_i \quad (6.18)$$

The potential energy of a node is defined as the potential energy of the total force acting on the node:

$$E_{\text{pot}}(i) = \|\mathbf{t}_i\|^2 \quad (6.19)$$

To ensure smoothness and rigidity of the contour a smoothness term is introduced. From standard finite difference technique the smoothness terms become.

$$E_{\text{smooth}}(i) = \|C_{i-1} - 2C_i + C_{i+1}\|^2 \quad (6.20)$$

The internal energy of a node is:

$$E_{\text{int}}(i) = \alpha E_{\text{pot}}(i) + \beta E_{\text{smooth}}(i) \quad (6.21)$$

,here  $\alpha$  and  $\beta$  are coefficients controlling the first and second order smoothness of the net.

### 6.3.4 External Energy of the Contour

The external energy of a node is defined as external forces acting on the node. In this context the external energy is the pixel value at the node position plus the pixel values of the neighbour nodes weighted by their inverse distance.

$$E_{\text{ext}}(i) = \omega I(C_i) + \rho \sum_{j \in N_2(i)} \frac{1}{\|C_i - C_j\|} I(C_j) \quad (6.22)$$

, here  $I(C_i)$  is the image intensity at point  $C_i$ . The image intensity is the intensity in a preprocessed version of the image as explained in section 6.1.3.

The total energy of the contour is given as:

$$E_{\text{total}} = \sum_{i \in N} E_{\text{int}}(i) + E_{\text{ext}}(i) \quad (6.23)$$

### 6.3.5 Energy Minimization

The minimization scheme used is explained in section 6.1.4. The only difference is that the walk used is simpler. In the active contour, nodes with odd number is visited when the iteration number is odd, and nodes with even numbers when the iteration number is even.

### 6.3.6 Results and Discussion

On figure 6.3(a) a slice is seen. On figure 6.3(b) the image used for external node energy is seen. The initial active contour configuration is seen in figure 6.8(a). The initial position is calculated in a way so the center of mass of the inner boundary is the center of a circle of nodes. The radius of the circle and the number of nodes can be given to the algorithm.

After 200 iteration the contour has changed configuration but not reached minimal energy as seen in figure 6.8(b). The final shape of the active contour can be seen in figure 6.8(c).

The contour fits the inner surface well. The fit could be smoother, but if the smoothness term  $\beta$  is increased the fit will not reach the boundary but tend to be more circular.

A C++ class CAContour has been developed. It is explained in appendix E.11.3.

## 6.4 Calculating the Resorption Area

When the inner and outer boundaries of the resorption area are located, the area is calculated. The inner and outer boundaries of the resorption area of a slice is seen in figure 6.9.

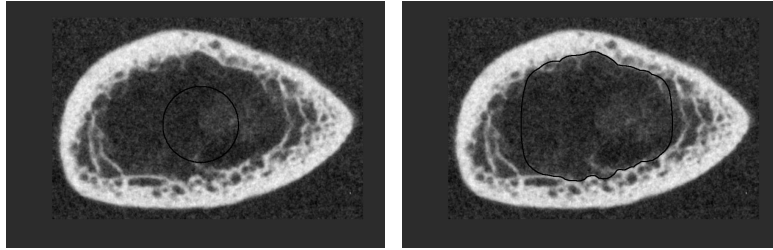
The area is calculated as the area of the fit of the outer boundary minus the area of the fit of the inner boundary.

The area feature is denoted  $\mathbf{A}_{\text{scalloping}}$ .

## 6.5 Results and Discussion

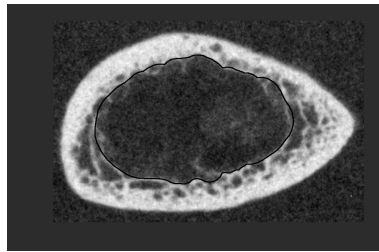
### 6.5.1 Comparison of Shape Features from All Bones

The mutual relations between various measurements on all bones are analyzed in this section. The analyzed features are single features from each bone.



(a) The initial position of the active contour.

(b) The active contour after 200 iterations.  $\alpha = 10, \beta = 200, \omega = 100, \rho = 5, p = 5\%, \gamma = 100$ .



(c) The active contour after 350 iterations.  $\alpha = 10, \beta = 200, \omega = 100, \rho = 5, p = 5\%, \gamma = 100$ .

Figure 6.8: The active contour locates the inner boundary of the endosteal resorption area of slice r-s11-03.

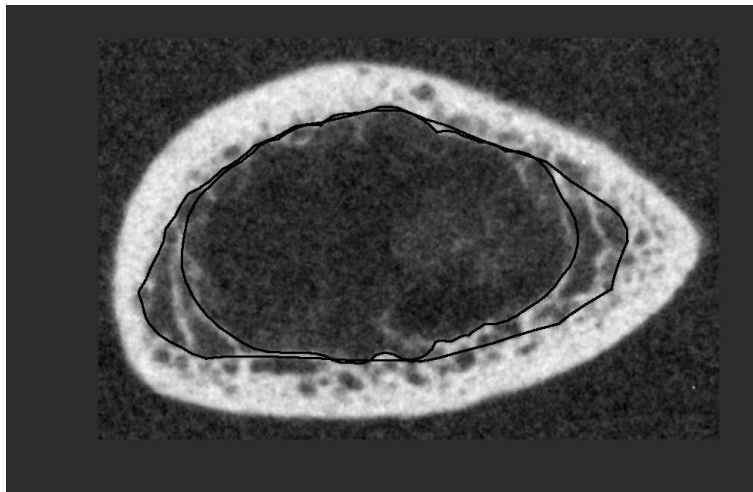


Figure 6.9: The outer and inner boundaries of the endosteal area of slice r-s11-03.

The shape features are an average of the features calculated on all slices in the bone.

### Correlation Analysis

The symbols  $X_i$  and  $Y_i$  will in this section be used to denote two variables from the same *bone*. Index  $i$  denotes the bone number.

A correlation matrix is calculated, the result is seen in table C.4–C.7. A set of the correlated variables are plotted in graphs that can be seen in figure C.18–C.37 on page 148–159. In the following a subset of the results seen in table C.4–C.7 is discussed. The subset of the results is seen in table 6.1.

The area feature measured with the active nets and contours has a good correlation with the subjective bone status (0.83) (as seen in figure 6.10) so the area of the endosteal resorption could be a good estimator for scalloping.

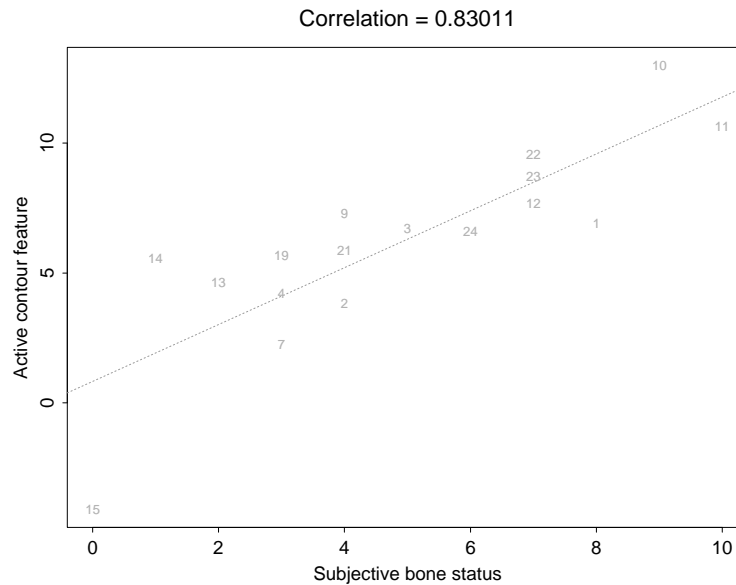


Figure 6.10: Subjective bone status and active contour feature on slices.

The age of death of the specimen has a low to moderate correlation with the active shape feature.

The active shape feature has a low correlation with scalloping measured by radiogrammetry (0.40). This is probably due to the fact that the radiogrammetric scalloping measure is a combination of all types of resorption, and the active shape feature only quantifies the endosteal resorption.



$X$	$Y$	$\text{cor}(X,Y)$
status	$A_{\text{scaloping}}$	0.83
age	$A_{\text{scaloping}}$	0.39
$A_{\text{scaloping}}$	scaloping	0.40

Table 6.1: Correlation between shape features measured on the bones. The shape features are an average of the features calculated on all slices in the bone. The data is subset of the data seen in table C.4–C.7 and the corresponding graphs are shown in figure C.18–C.37.

## Chapter 7

# Conclusion

The organization of this thesis represents roughly the nature of the practical and theoretical work, respectively, which has been carried out during the project period.

In the first practical part of the thesis, it is demonstrated, how a forearm bone is sectioned into bone slices and, how subsequent contact radiographs are produced from the resulting slices.

The second, more theoretical part of the thesis describes mainly the type of image processing that has been applied to the contact radiographs in order to provide information of the skeletal status of the bone. This information is used to evaluate a set of radiogrammetrical algorithms that have been used to analyze *ordinary* radiographs of the sectioned bones.

The developed protocol for making contact radiographs of slices of bones proved to give very valuable information regarding the status of the bone under examination.

The preparation and sectioning of bone is a very time consuming process and it is therefore worthy to consider alternative approaches that enable the same kind of 3-dimensional analysis of the inner structure of bone. An example of such an alternative and increasingly used method is micro-CT, which has some major advantages, compared to the sectioning approach. If a larger study of contact radiographs of slices of bone was needed, micro CT should be considered as an alternative image acquisition method, since it could provide the images without destroying the bone. In disfavor of micro-CT counts, that it does not have nearly the same resolution as the radiographs presented in this thesis, but it will certainly change with time.

The developed image class library works very well and compiles and runs under several environments. The object oriented paradigm provided by C++ is very suitable for the creation of complex data structures and data handling as demonstrated in the implementation of the active shape classes.

## Appendix A

### Photos



Figure A.1: Some of the materials used. The bone to the left is radius  $r-s1$ . The small mark on the distal end is the fixpoint. The anterior side is facing upwards.

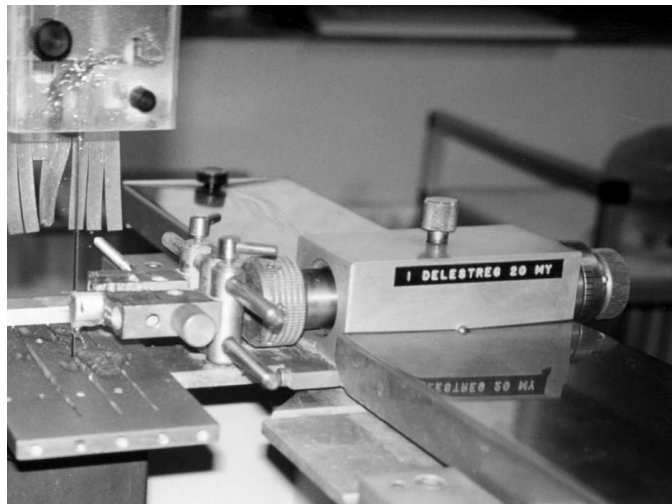


Figure A.2: The EXAKT diamant saw used for sectioning the bones. A segment of bone is mounted and a slice is cut half through.



Figure A.3: The hobby saw used for splitting the bone into a proximal and distal part. The bone being saw is an ulna used in the first pilot study to determine the minimal slice width. The ulna was cut into five smaller pieces.



Figure A.4: The slices are kept in labeled plastic bags. In the pilot study slices with a thickness of  $200\ \mu\text{m}$  were cut. These thin slices were kept in small plastic boxes. Some methods to make a water proof mark were tested as indicated by the bottle of nail polish. The best result was achieved with a water proof pen on dry bone.

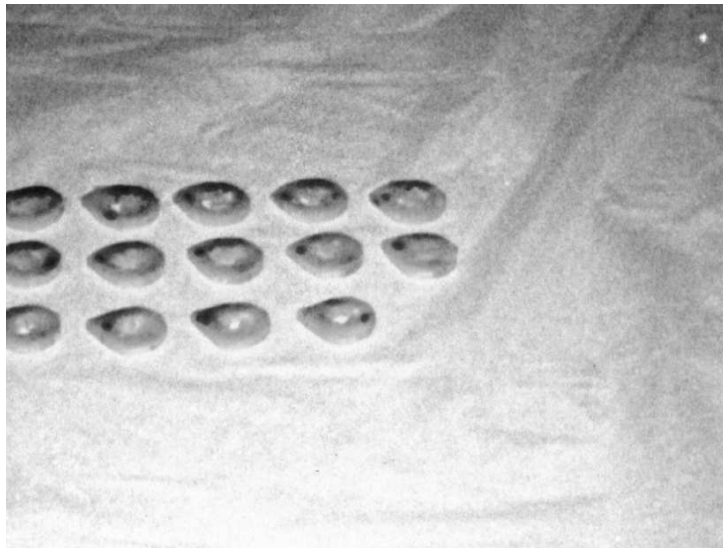


Figure A.5: The placement of slices when a contact radiograph was taken. Note that not all slices of the current bone have been placed.

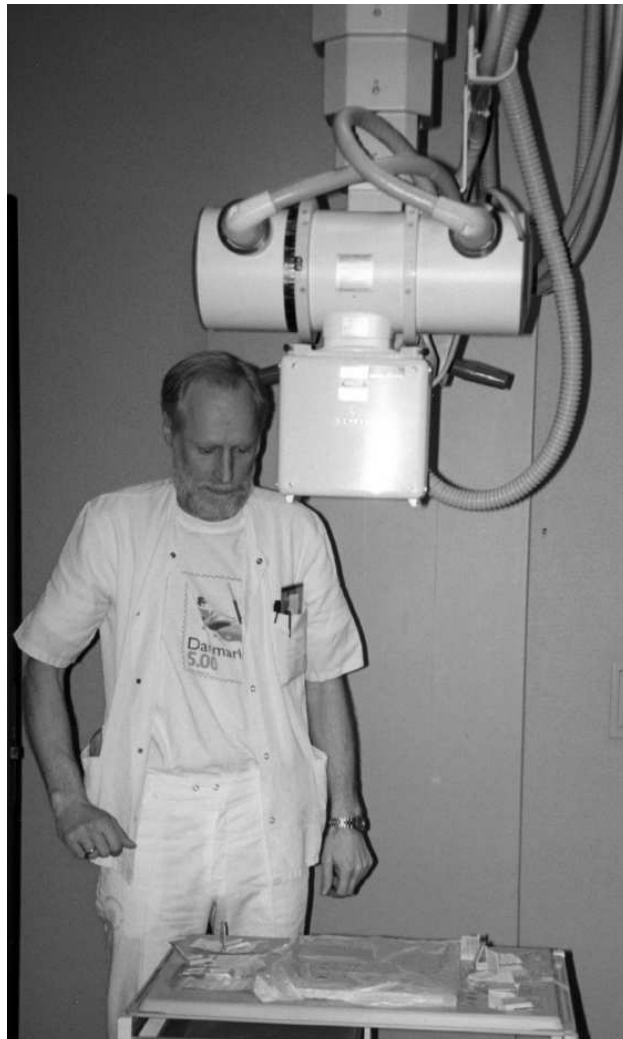


Figure A.6: The x-ray apparatus used. Jens Søgaard has everything under control.

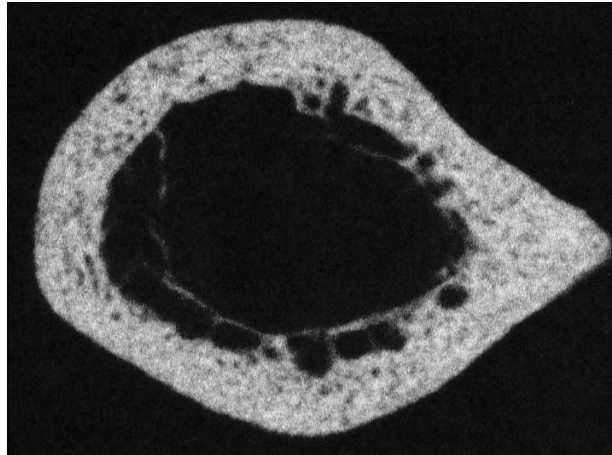


## Appendix B

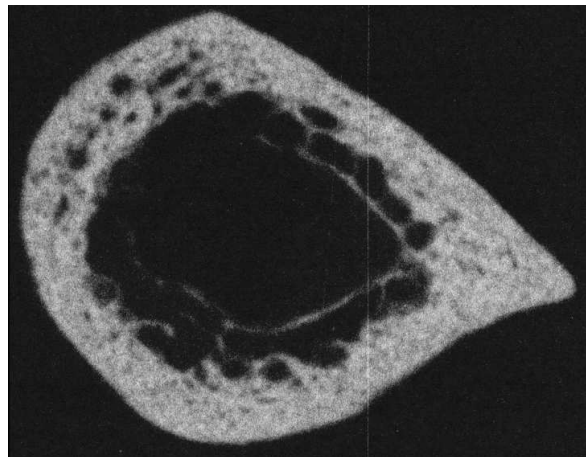
### A Gallery of Slices

From each radius over 20 slices has been cut and processed, therefore the entire image material consists of more than 350 images. Instead of including all images in the thesis, a gallery of slices is shown. Two slices from each radius, one from the distal part and one from the proximal part, is shown.

The slices are depicted with the distal side facing up, the ulnar side to the right, the radial side to the left, the posterior side up and the anterior down.

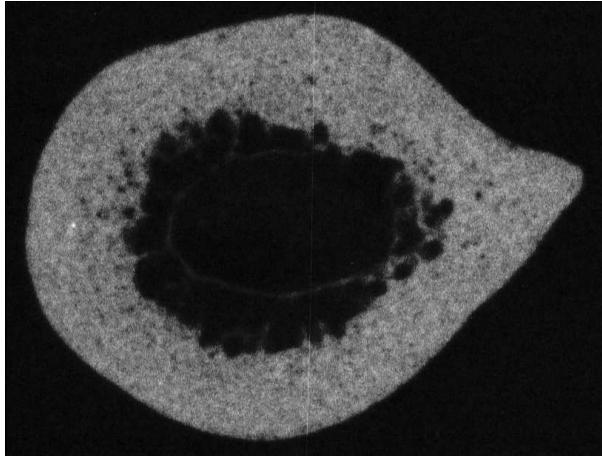


(a) A distal slice,  $r-s1-08$ .

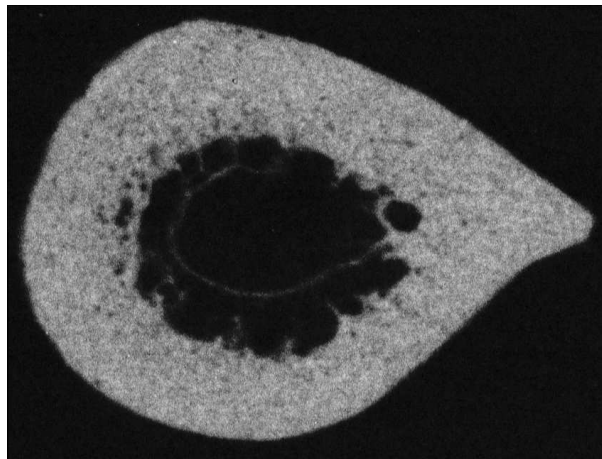


(b) A proximal slice,  $r-s1-19$ .

Figure B.1: Slices from  $r-s1$ .

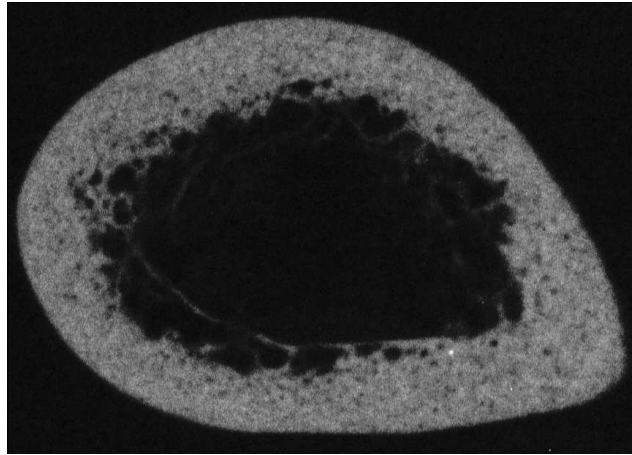


(a) A distal slice,  $r-s2-08$ .

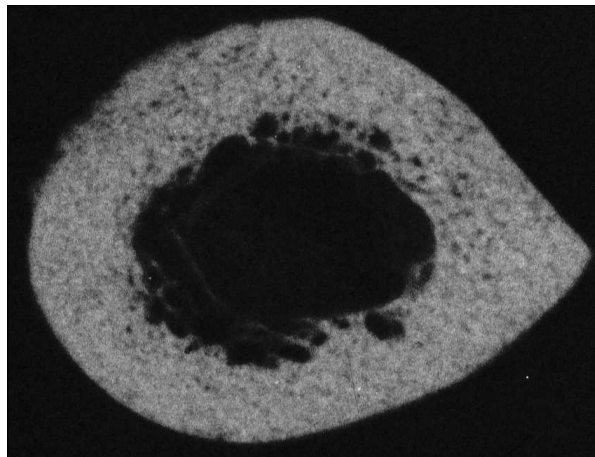


(b) A proximal slice,  $r-s2-19$ .

Figure B.2: Slices from  $r-s2$ .

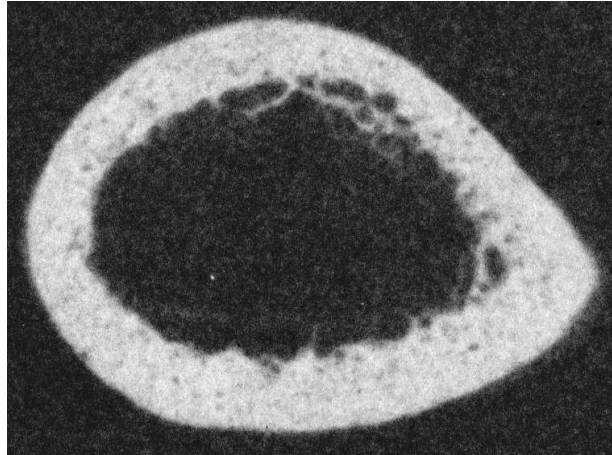


(a) A distal slice, *r-s3-08*.

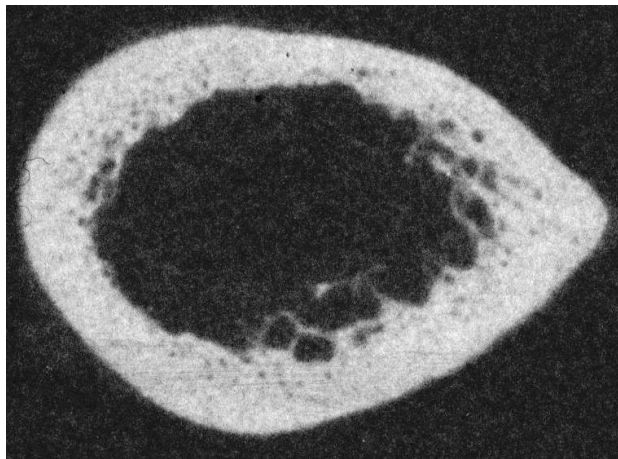


(b) A proximal slice, *r-s3-19*.

Figure B.3: Slices from *r-s3*.

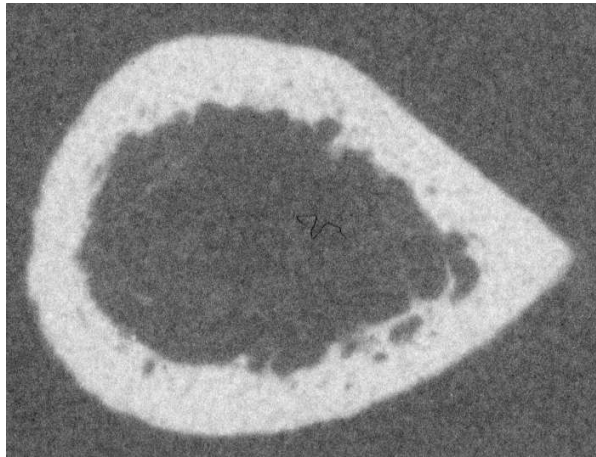


(a) A distal slice, *r-s4-08*.

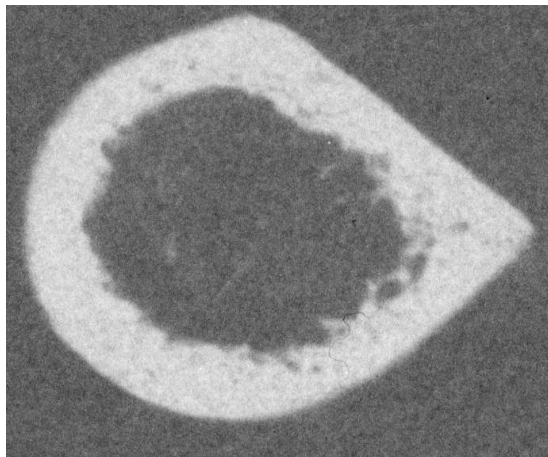


(b) A proximal slice, *r-s4-19*.

Figure B.4: Slices from *r-s4*.

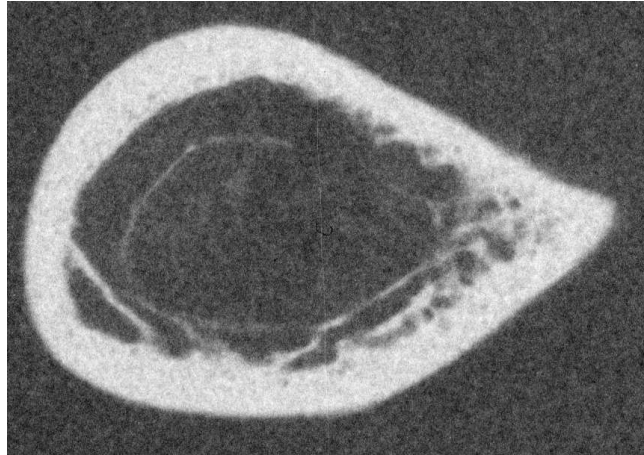


(a) A distal slice,  $r-s7-08$ .

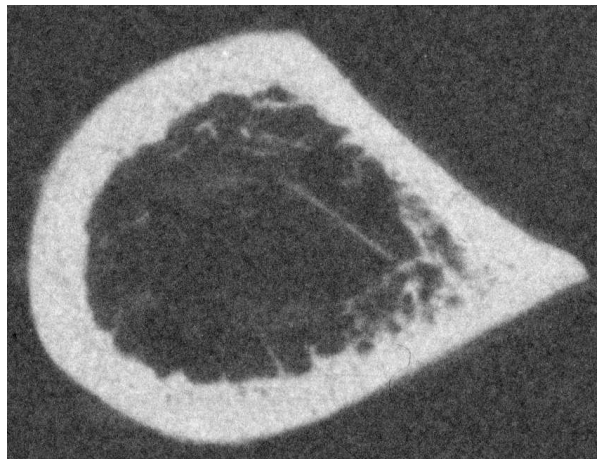


(b) A proximal slice,  $r-s7-19$ .

Figure B.5: Slices from  $r-s7$ .

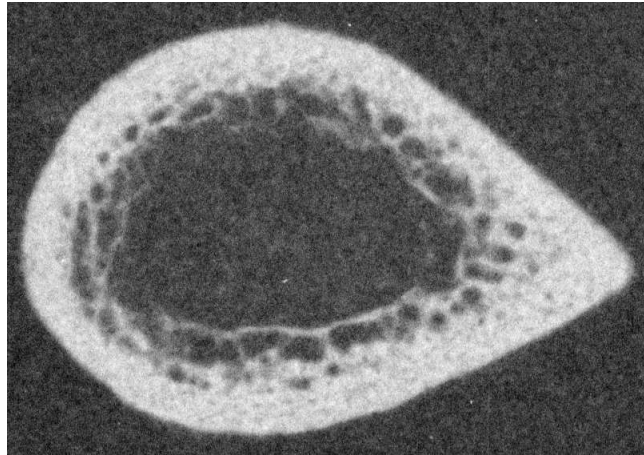


(a) A distal slice, *r-s9-08*.

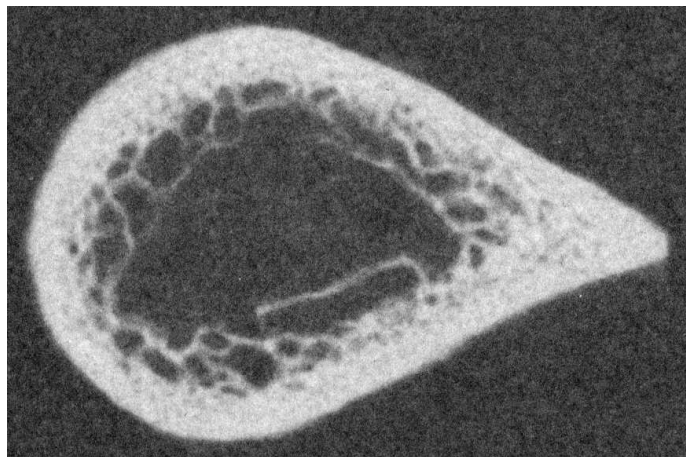


(b) A proximal slice, *r-s9-19*.

Figure B.6: Slices from *r-s9*.



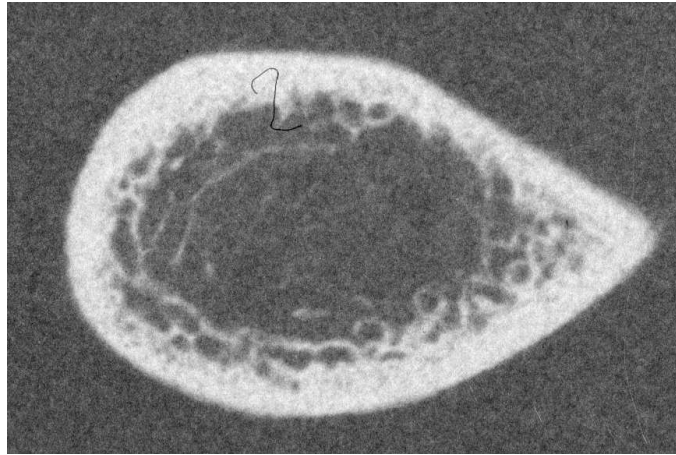
(a) A distal slice, r-s10-08.



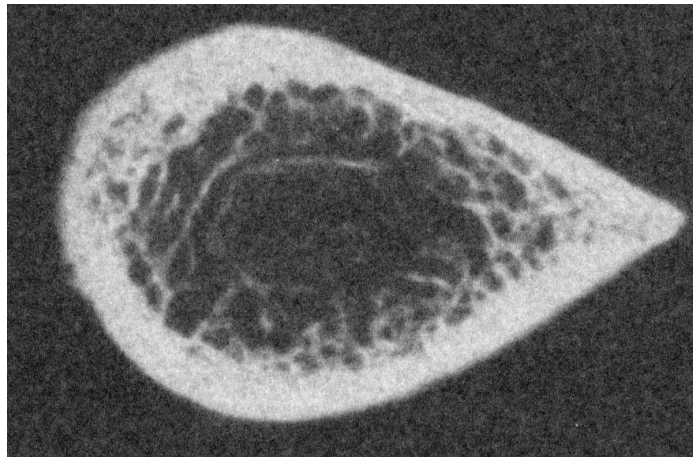
(b) A proximal slice, r-s10-19.

Figure B.7: Slices from r-s10.



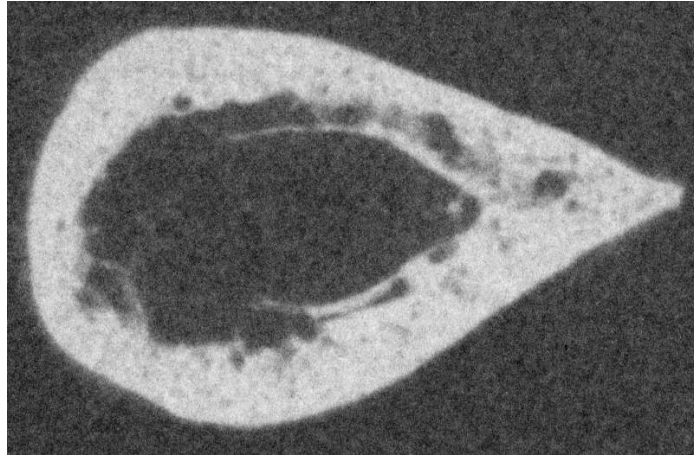


(a) A distal slice, r-s11-08.

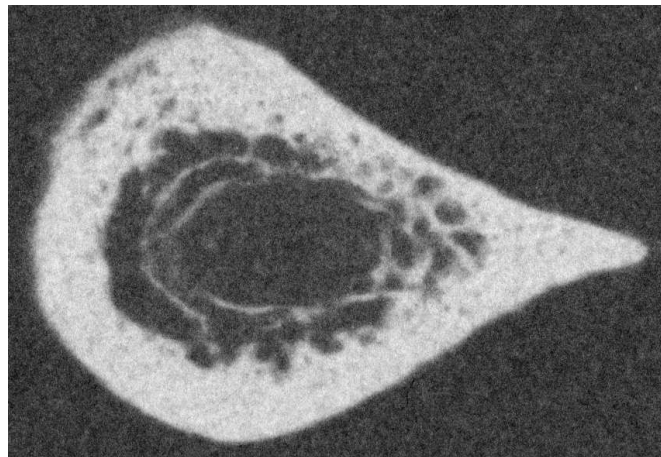


(b) A proximal slice, r-s11-19.

Figure B.8: Slices from r-s11.

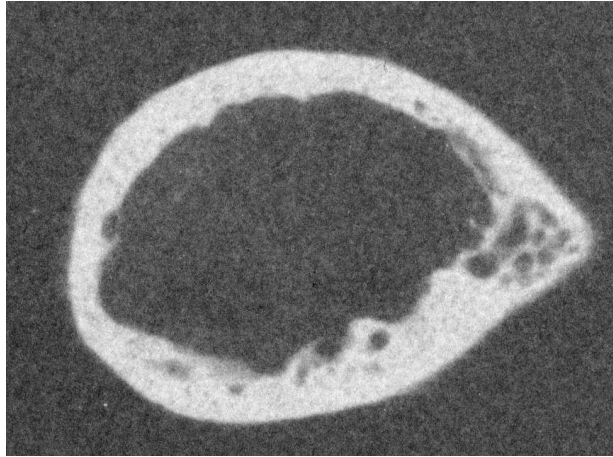


(a) A distal slice, r-s12-08.

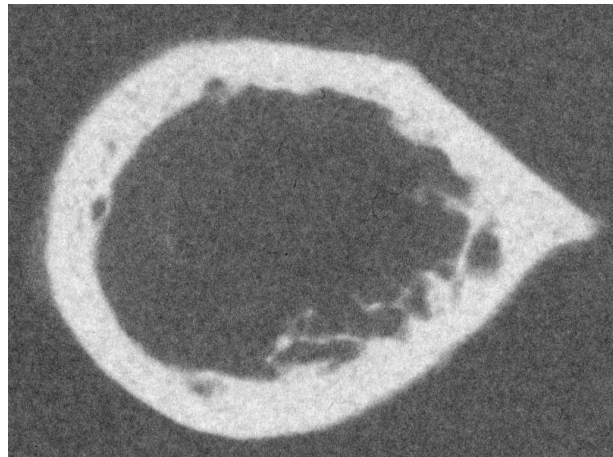


(b) A proximal slice, r-s12-19.

Figure B.9: Slices from r-s12.

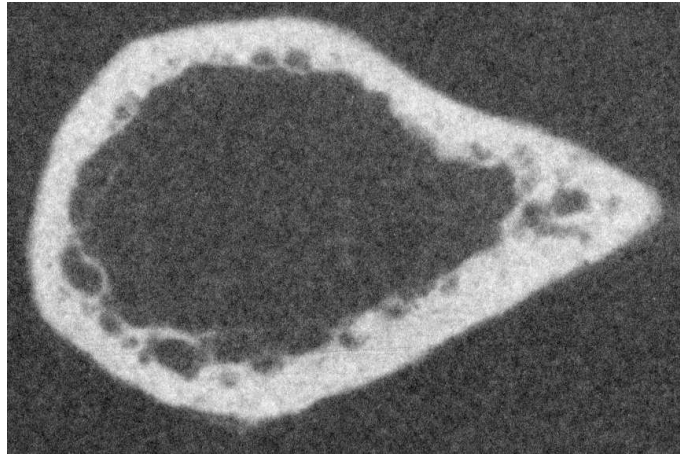


(a) A distal slice, r-s13-08.

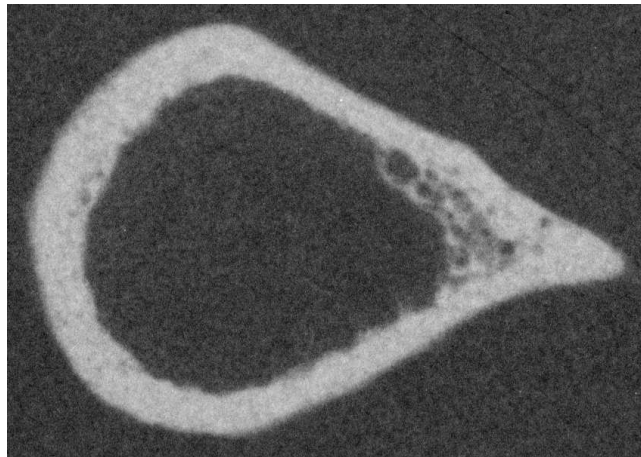


(b) A proximal slice, r-s13-19.

Figure B.10: Slices from r-s13.

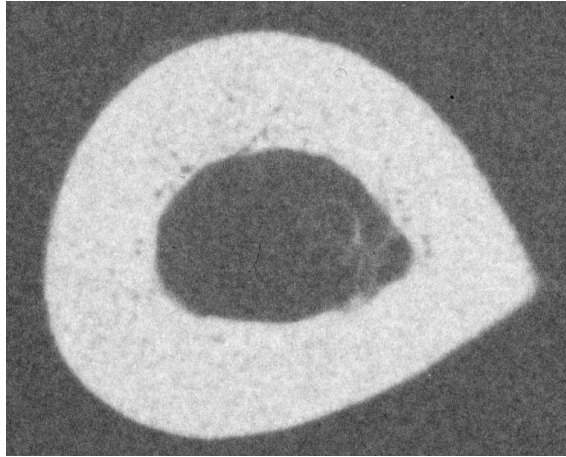


(a) A distal slice, r-s14-08.

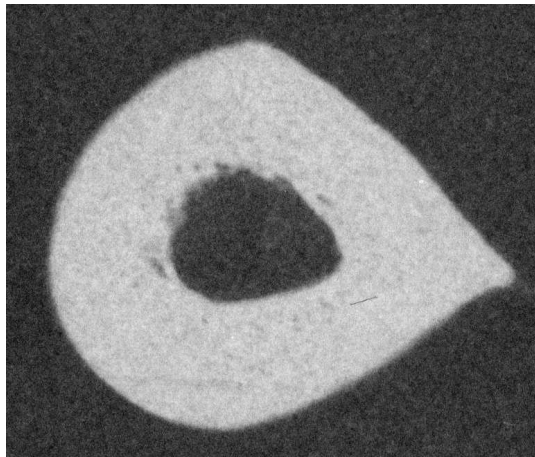


(b) A proximal slice, r-s14-19.

Figure B.11: Slices from r-s14.

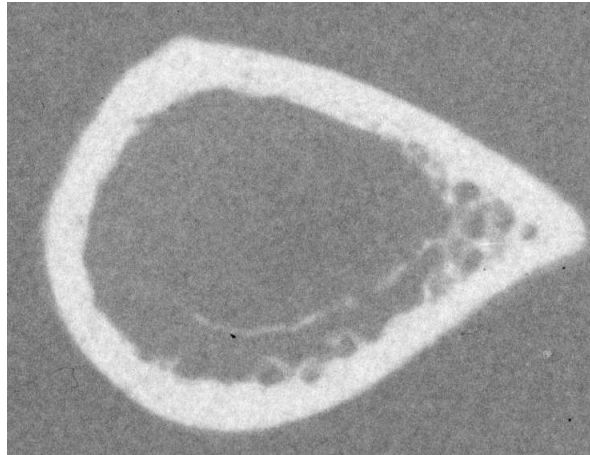


(a) A distal slice, r-s15-08.

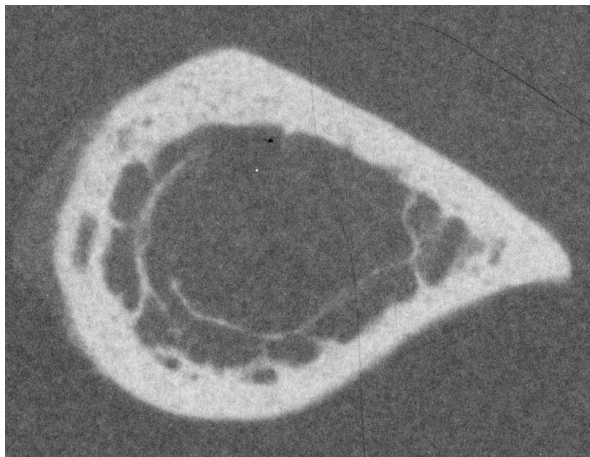


(b) A proximal slice, r-s15-19.

Figure B.12: Slices from r-s15.

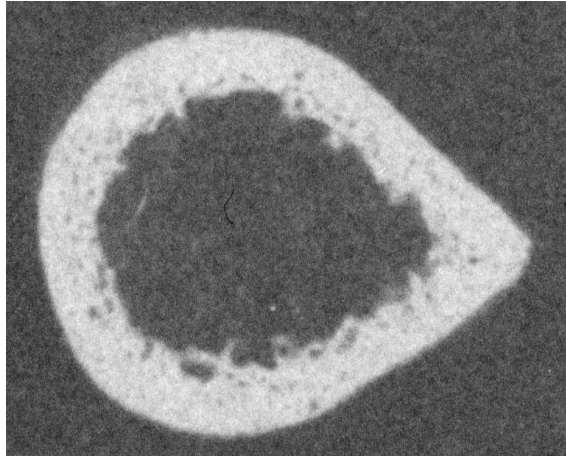


(a) A distal slice, r-s19-08.

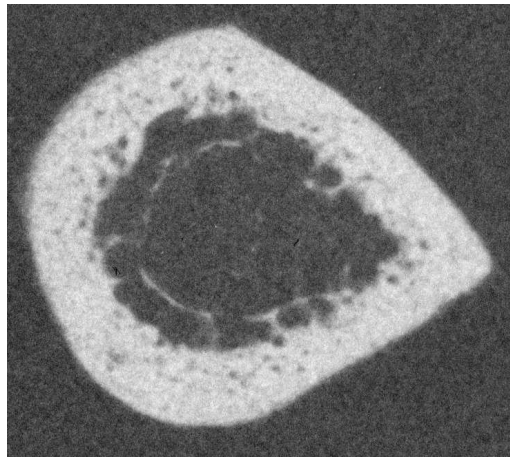


(b) A proximal slice, r-s19-19.

Figure B.13: Slices from r-s19.

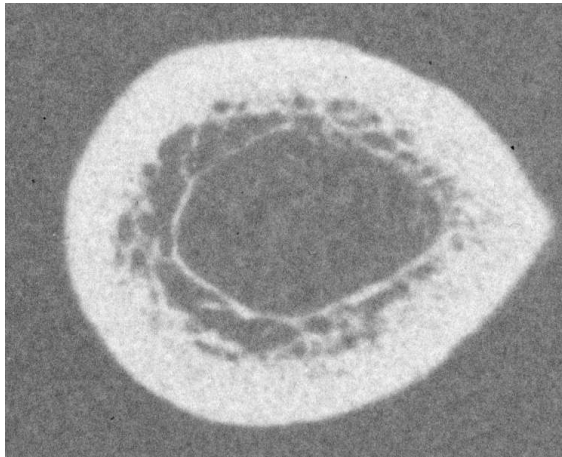


(a) A distal slice, r-s21-08.

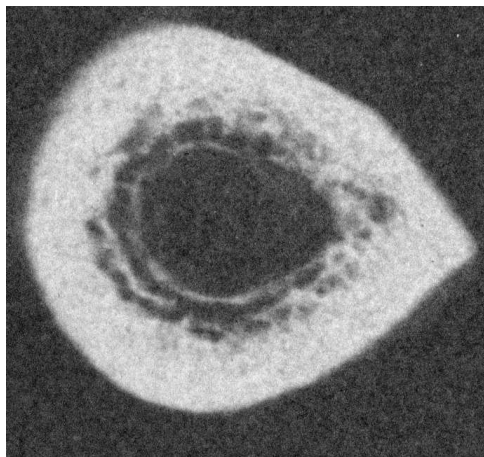


(b) A proximal slice, r-s21-19.

Figure B.14: Slices from r-s21.



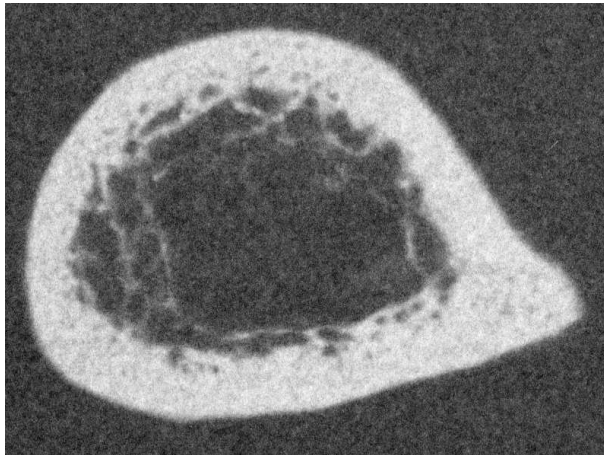
(a) A distal slice, r-s22-08.



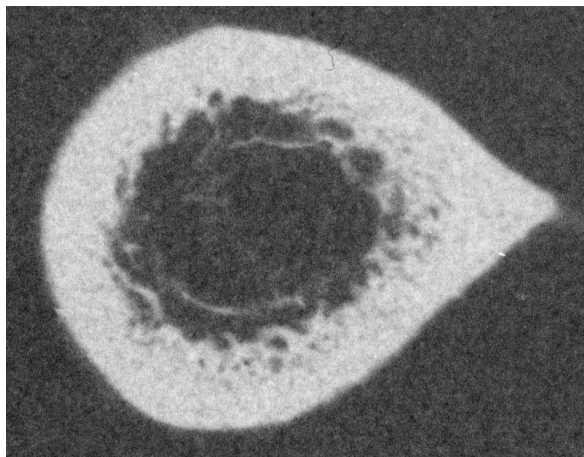
(b) A proximal slice, r-s22-19.

Figure B.15: Slices from r-s22.



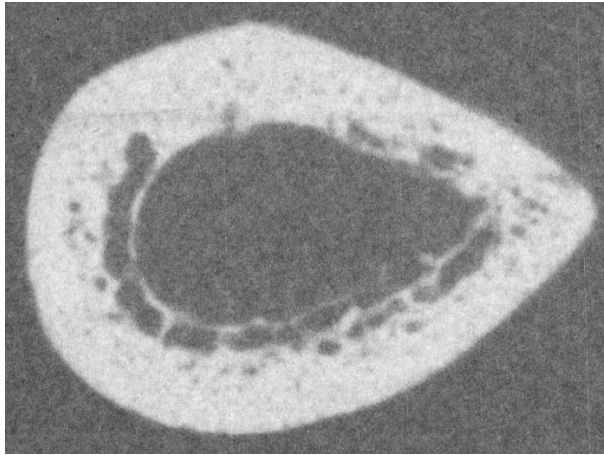


(a) A distal slice, r-s23-08.

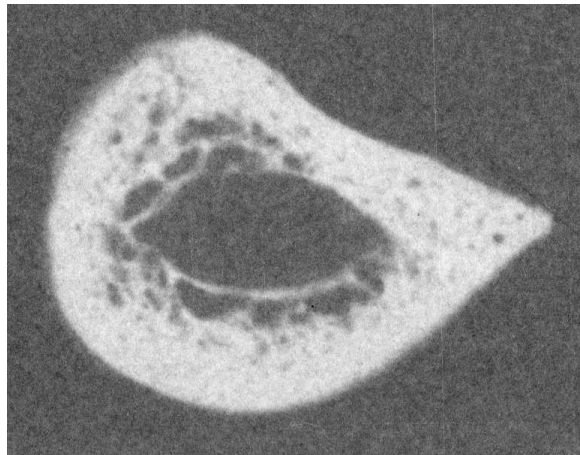


(b) A proximal slice, r-s23-19.

Figure B.16: Slices from r-s23.



(a) A distal slice, r-s24-08.



(b) A proximal slice, r-s24-19.

Figure B.17: Slices from r-s24.

# Appendix C

## Graphs and Tables

### C.1 Cortical Thickness on a Single Bone

#### C.1.1 Plots of cortical thickness

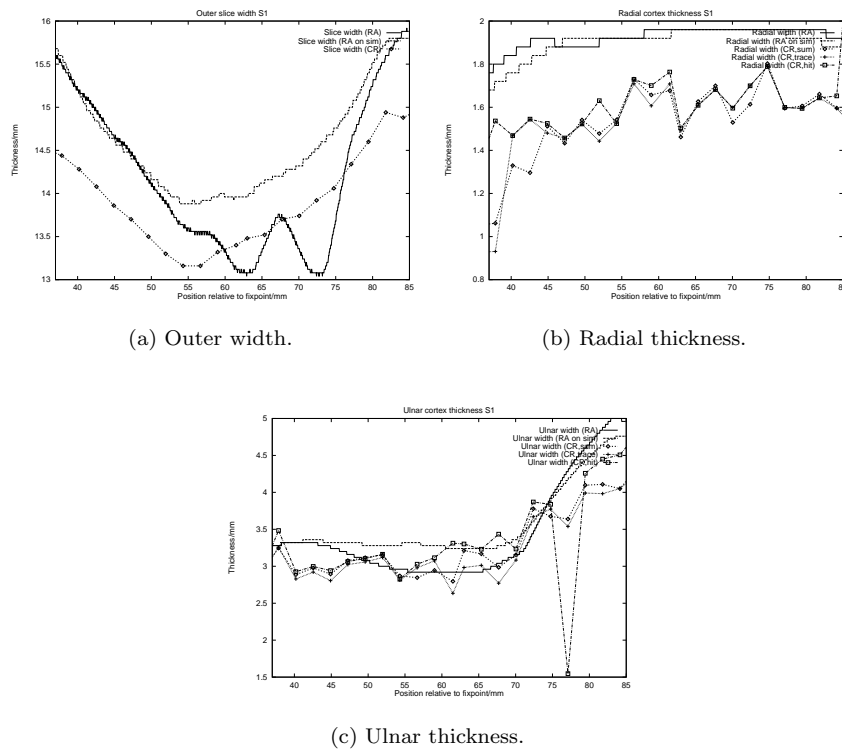
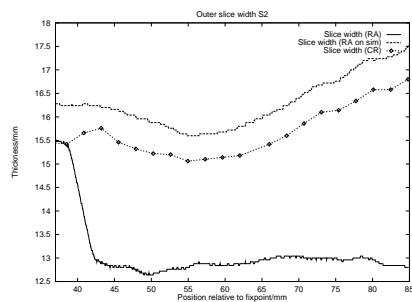
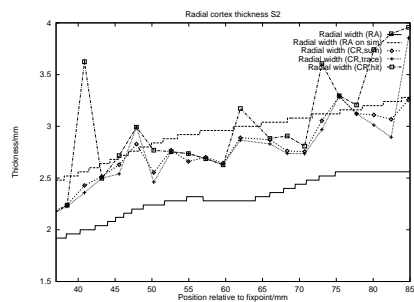


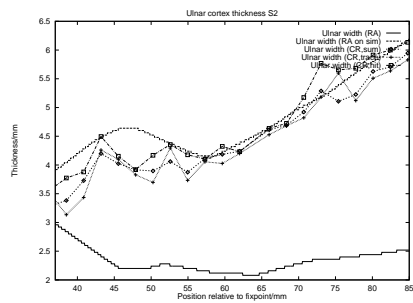
Figure C.1: Cortical Thickness of slice r-s1.



(a) Outer width.

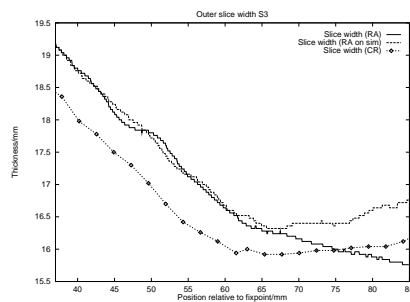


(b) Radial thickness.

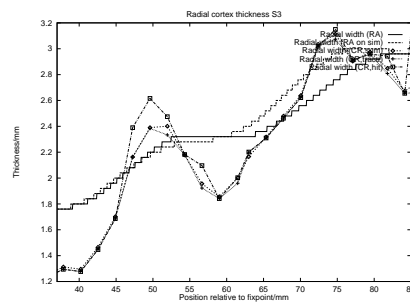


(c) Ulnar thickness.

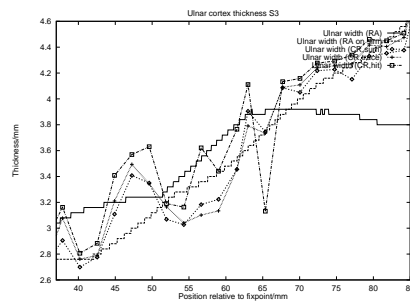
Figure C.2: Cortical Thickness of slice r-s2.



(a) Outer width.

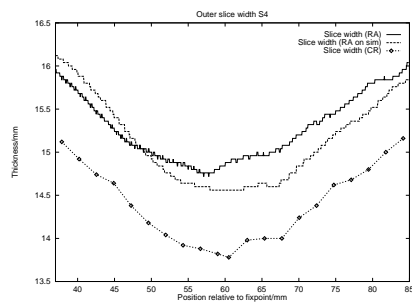


(b) Radial thickness.

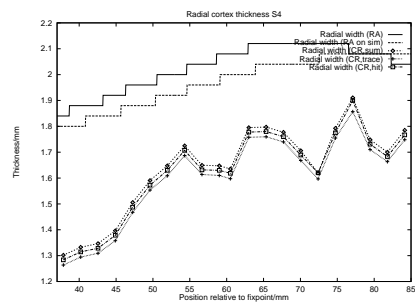


(c) Ulnar thickness.

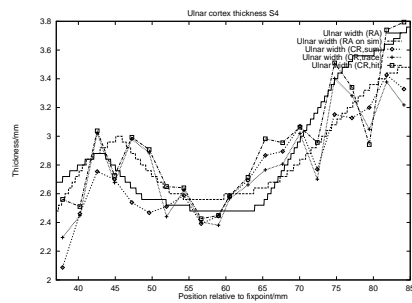
Figure C.3: Cortical Thickness of slice r-s3.



(a) Outer width.

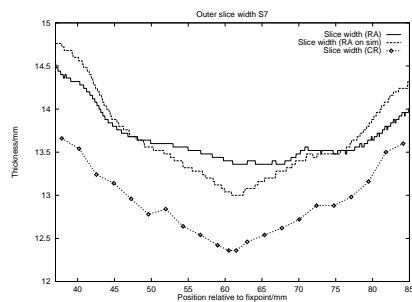


(b) Radial thickness.

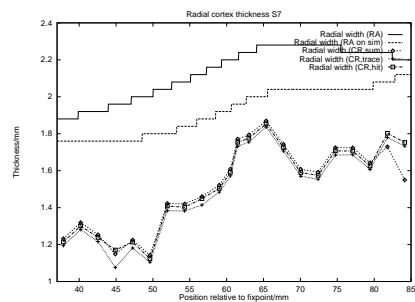


(c) Ulnar thickness.

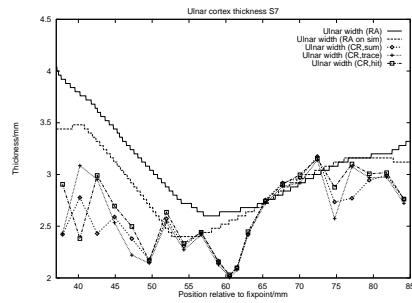
Figure C.4: Cortical Thickness of slice r-s4.



(a) Outer width.

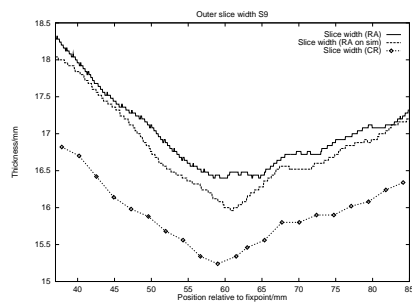


(b) Radial thickness.

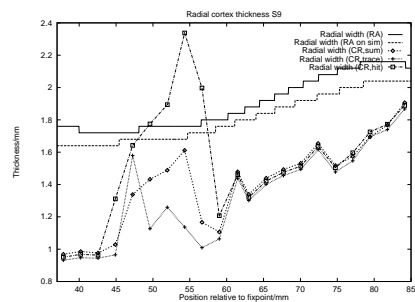


(c) Ulnar thickness.

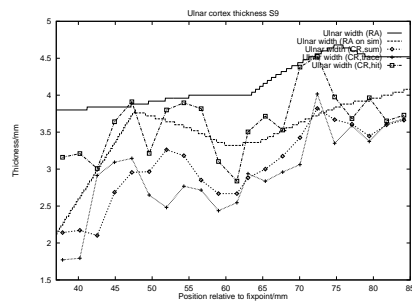
Figure C.5: Cortical Thickness of slice r-s7.



(a) Outer width.



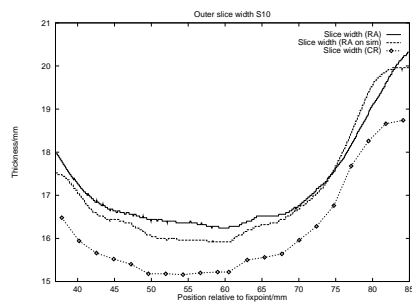
(b) Radial thickness.



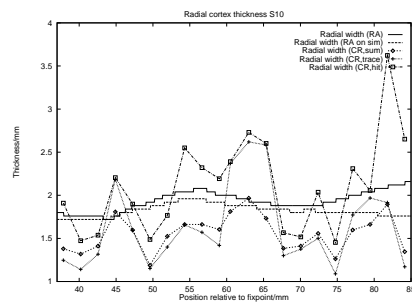
(c) Ulnar thickness.

Figure C.6: Cortical Thickness of slice r-s9.

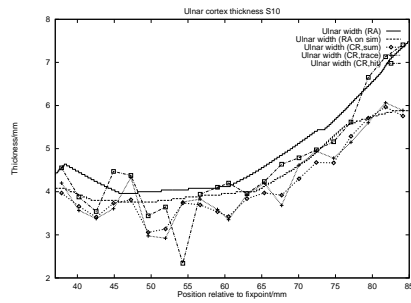




(a) Outer width.

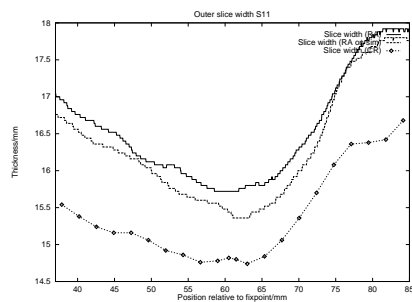


(b) Radial thickness.

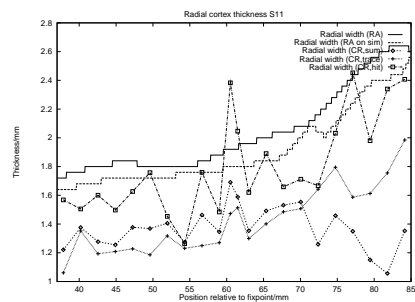


(c) Ulnar thickness.

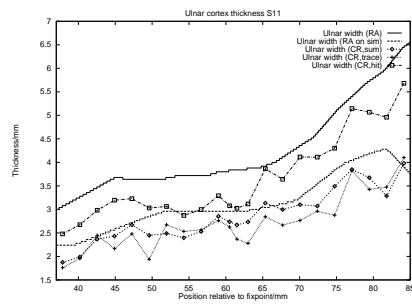
Figure C.7: Cortical Thickness of slice r-s10.



(a) Outer width.

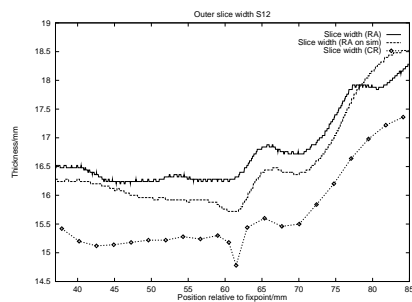


(b) Radial thickness.

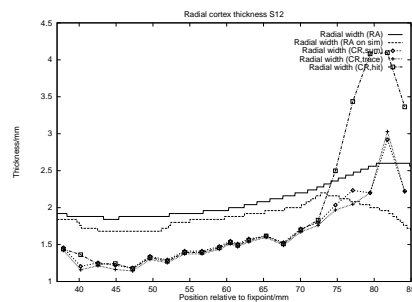


(c) Ulnar thickness.

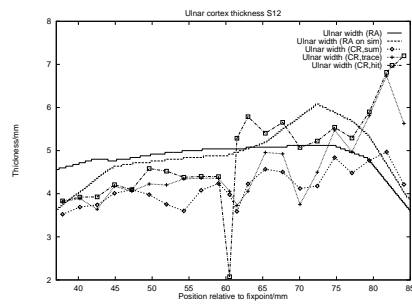
Figure C.8: Cortical Thickness of slice r-s11.



(a) Outer width.

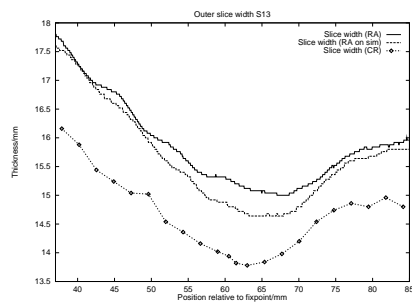


(b) Radial thickness.

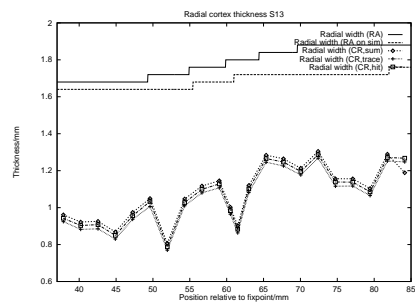


(c) Ulnar thickness.

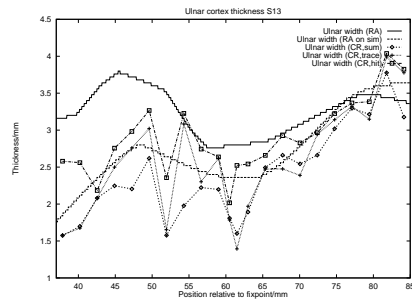
Figure C.9: Cortical Thickness of slice r-s12.



(a) Outer width.

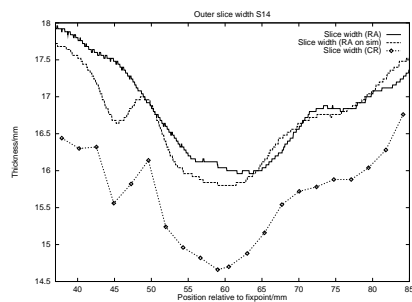


(b) Radial thickness.

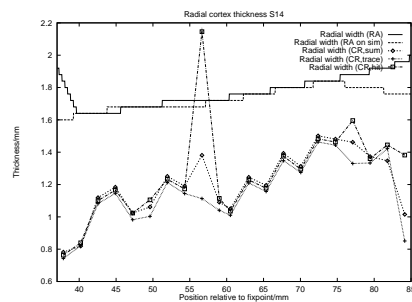


(c) Ulnar thickness.

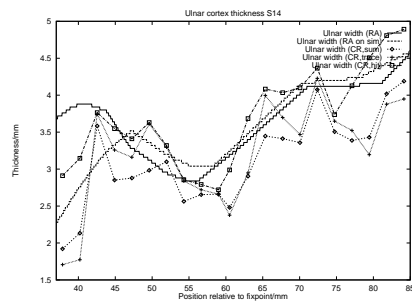
Figure C.10: Cortical Thickness of slice r-s13.



(a) Outer width.

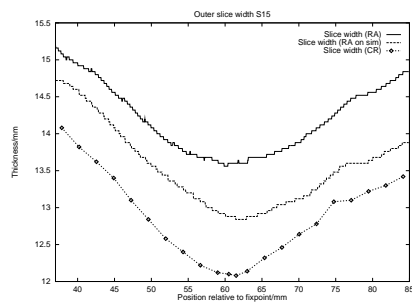


(b) Radial thickness.

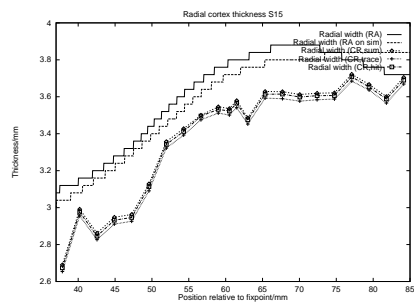


(c) Ulnar thickness.

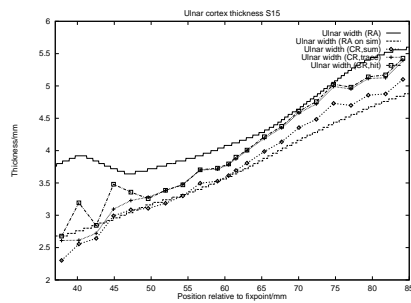
Figure C.11: Cortical Thickness of slice r-s14.



(a) Outer width.

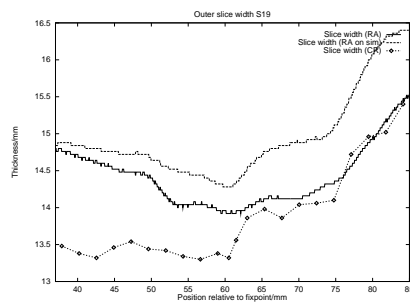


(b) Radial thickness.

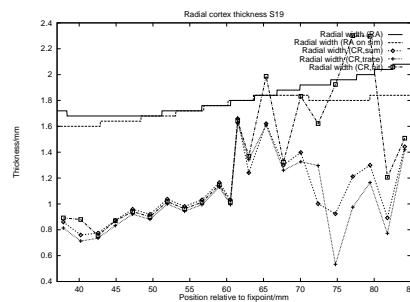


(c) Ulnar thickness.

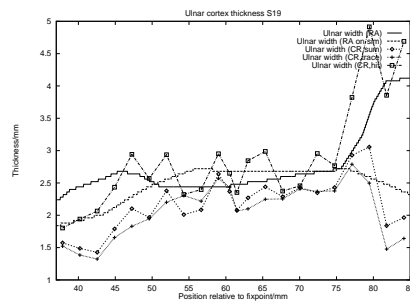
Figure C.12: Cortical Thickness of slice r-s15.



(a) Outer width.

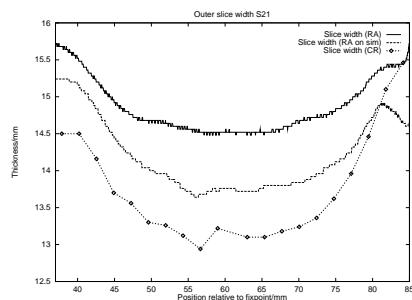


(b) Radial thickness.

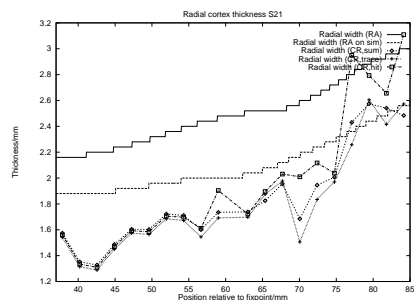


(c) Ulnar thickness.

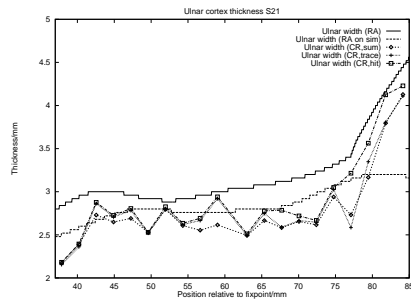
Figure C.13: Cortical Thickness of slice r-s19.



(a) Outer width.



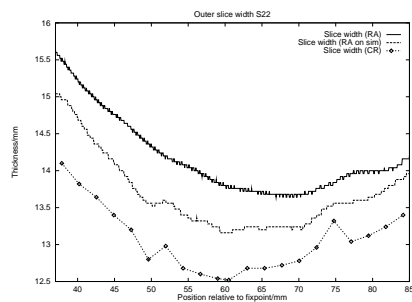
(b) Radial thickness.



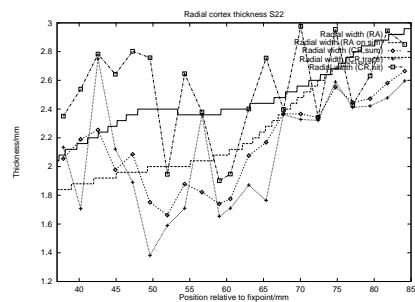
(c) Ulnar thickness.

Figure C.14: Cortical Thickness of slice r-s21.

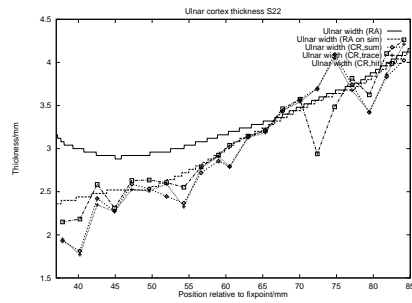




(a) Outer width.

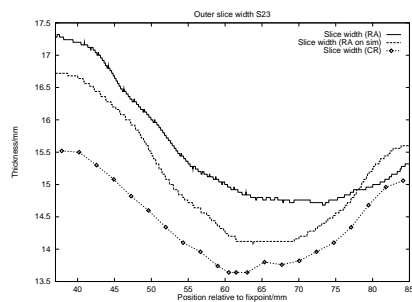


(b) Radial thickness.

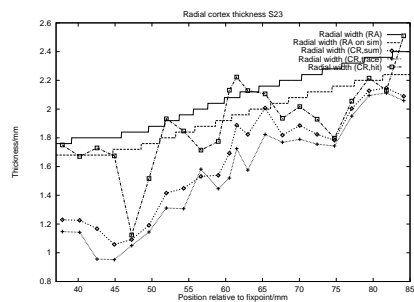


(c) Ulnar thickness.

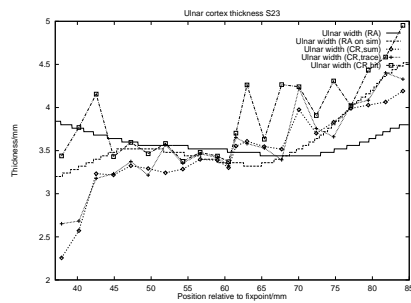
Figure C.15: Cortical Thickness of slice r-s22.



(a) Outer width.

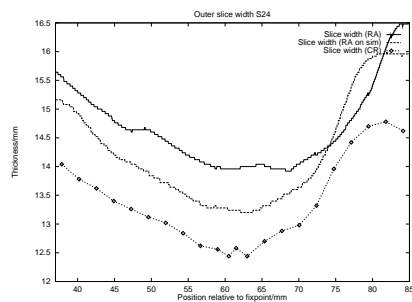


(b) Radial thickness.

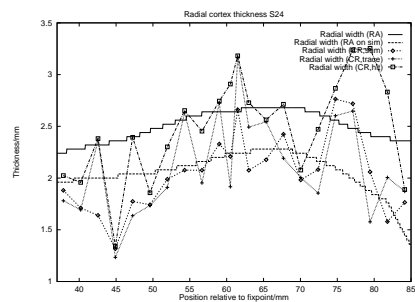


(c) Ulnar thickness.

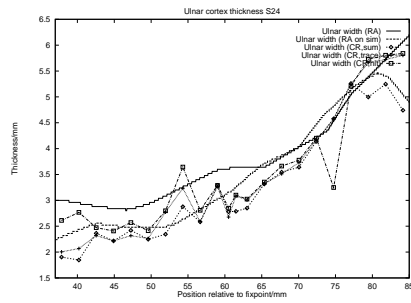
Figure C.16: Cortical Thickness of slice r-s23.



(a) Outer width.



(b) Radial thickness.



(c) Ulnar thickness.

Figure C.17: Cortical Thickness of slice r-s24.

## C.1.2 Correlation between endpoint variables

	<b>Place</b>	<b>w<sub>sum,pos</sub></b>	<b>w<sub>sum,ulh</sub></b>	<b>w<sub>sum,ant</sub></b>	<b>w<sub>sum,rad</sub></b>	<b>w<sub>sum,uln,max</sub></b>	<b>w<sub>trace,pos</sub></b>
<b>Place</b>	—	0.499	0.794	0.411	0.6797	0.836	0.463
<b>w<sub>sum,pos</sub></b>	0.499	—	0.523	0.416	0.4622	0.527	0.961
<b>w<sub>sum,ulh</sub></b>	0.794	0.523	—	0.409	0.6150	0.895	0.490
<b>w<sub>sum,ant</sub></b>	0.411	0.416	0.409	—	0.5176	0.396	0.398
<b>w<sub>sum,rad</sub></b>	0.680	0.462	0.615	0.518	—	0.589	0.437
<b>w<sub>sum,uln,max</sub></b>	0.836	0.527	0.895	0.396	0.5893	—	0.500
<b>w<sub>trace,pos</sub></b>	0.463	0.961	0.490	0.398	0.4369	0.500	—
<b>w<sub>trace,ulh</sub></b>	0.732	0.508	0.932	0.399	0.5719	0.844	0.482
<b>w<sub>trace,ant</sub></b>	0.350	0.419	0.397	0.859	0.4902	0.377	0.410
<b>w<sub>trace,rad</sub></b>	0.699	0.470	0.634	0.459	0.8824	0.602	0.426
<b>w<sub>trace,uln,max</sub></b>	0.772	0.529	0.857	0.384	0.5440	0.936	0.498
<b>w<sub>hit,pos</sub></b>	0.527	0.903	0.536	0.390	0.4269	0.536	0.856
<b>w<sub>hit,ulh</sub></b>	0.757	0.482	0.863	0.305	0.5055	0.809	0.448
<b>w<sub>hit,ant</sub></b>	0.327	0.320	0.350	0.674	0.4255	0.329	0.312
<b>w<sub>hit,rad</sub></b>	0.675	0.486	0.624	0.420	0.7901	0.625	0.458
<b>w<sub>hit,uln,max</sub></b>	0.760	0.501	0.784	0.275	0.4674	0.846	0.480
<b>w<sub>total</sub></b>	0.148	0.177	0.248	-0.195	-0.0934	0.290	0.163
<b>A<sub>res</sub></b>	0.682	0.699	0.769	0.524	0.6370	0.772	0.670
<b>A<sub>nores</sub></b>	0.710	0.691	0.781	0.545	0.6689	0.797	0.661

Table C.1: Correlation between measured endpoint variables. The values are the mean correlation for all bones.

	$W_{\text{trace,uln}}$	$W_{\text{trace,ant}}$	$W_{\text{trace,rad}}$	$W_{\text{trace,uln,max}}$	$W_{\text{hit,pos}}$	$W_{\text{hit,uln}}$
<b>Place</b>	0.732	0.350	0.6987	0.772	0.527	0.757
$W_{\text{sum,pos}}$	0.508	0.419	0.4696	0.529	0.903	0.482
$W_{\text{sum,uln}}$	0.932	0.397	0.6345	0.857	0.536	0.863
$W_{\text{sum,ant}}$	0.399	0.859	0.4593	0.384	0.390	0.305
$W_{\text{sum,rad}}$	0.572	0.490	0.8824	0.544	0.427	0.505
$W_{\text{sum,uln,max}}$	0.844	0.377	0.6016	0.936	0.536	0.809
$W_{\text{trace,pos}}$	0.482	0.410	0.4264	0.498	0.856	0.448
$W_{\text{trace,uln}}$	—	0.393	0.6002	0.898	0.507	0.803
$W_{\text{trace,ant}}$	0.393	—	0.4143	0.365	0.375	0.300
$W_{\text{trace,rad}}$	0.600	0.414	—	0.577	0.449	0.539
$W_{\text{trace,uln,max}}$	0.898	0.365	0.5765	—	0.537	0.783
$W_{\text{hit,pos}}$	0.507	0.375	0.4491	0.537	—	0.490
$W_{\text{hit,uln}}$	0.803	0.300	0.5392	0.783	0.490	—
$W_{\text{hit,ant}}$	0.330	0.557	0.3525	0.300	0.317	0.262
$W_{\text{hit,rad}}$	0.584	0.397	0.7477	0.576	0.465	0.537
$W_{\text{hit,uln,max}}$	0.756	0.273	0.5058	0.827	0.496	0.832
$W_{\text{total}}$	0.216	-0.120	-0.0193	0.304	0.204	0.387
$A_{\text{res}}$	0.752	0.529	0.6517	0.775	0.689	0.684
$A_{\text{nores}}$	0.749	0.539	0.6523	0.778	0.684	0.690

Table C.2: Correlation between measured endpoint variables. The values are the mean correlation for all bones.

Place	$w_{hit,ant}$	$w_{hit,rad}$	$w_{hit,uln,max}$	$w_{total}$	$A_{res}$	$A_{nores}$
<b>Place</b>	0.327	0.675	0.760	0.1485	0.682	0.710
$w_{sum,pos}$	0.320	0.486	0.501	0.1775	0.699	0.691
$w_{sum,uln}$	0.350	0.624	0.784	0.2476	0.769	0.781
$w_{sum,ant}$	0.674	0.420	0.275	-0.1950	0.524	0.545
$w_{sum,rad}$	0.426	0.790	0.467	-0.0934	0.637	0.669
$w_{sum,uln,max}$	0.329	0.625	0.846	0.2897	0.772	0.797
$w_{trace,pos}$	0.312	0.458	0.480	0.1634	0.670	0.661
$w_{trace,uln}$	0.330	0.584	0.756	0.2159	0.752	0.749
$w_{trace,ant}$	0.557	0.397	0.273	-0.1204	0.529	0.539
$w_{trace,rad}$	0.353	0.748	0.506	-0.0193	0.652	0.652
$w_{trace,uln,max}$	0.300	0.576	0.827	0.3037	0.775	0.778
$w_{hit,pos}$	0.317	0.465	0.496	0.2043	0.689	0.684
$w_{hit,uln}$	0.262	0.537	0.832	0.3868	0.684	0.690
$w_{hit,ant}$	—	0.367	0.246	-0.1186	0.467	0.472
$w_{hit,rad}$	0.367	—	0.544	0.0600	0.652	0.669
$w_{hit,uln,max}$	0.246	0.544	—	0.4054	0.696	0.701
$w_{total}$	-0.119	0.060	0.405	—	0.321	0.294
$A_{res}$	0.467	0.652	0.696	0.3209	—	0.985
$A_{nores}$	0.472	0.669	0.701	0.2941	0.985	—

Table C.3: Correlation between measured endpoint variables. The values are the mean correlation for all bones.

## **C.2 Comparison of features from all bones**

### **C.2.1 Correlation between endpoint variables**



	Age	Status	$w_{total}$	$w_{sum,pos}$	$w_{sum,uln}$	$w_{sum,ant}$	$w_{sum,rad}$
<b>Age</b>	—	0.1587	0.2030	-0.710	-0.26130	-0.7799	-0.700
<b>Status</b>	0.1588	—	0.2269	-0.188	0.30568	-0.0632	-0.191
$w_{total}$	0.2027	0.2269	—	-0.164	0.40938	-0.1304	-0.193
$w_{sum,pos}$	-0.7095	-0.1884	-0.1642	—	0.50291	0.8914	0.957
$w_{sum,uln}$	-0.2613	0.3057	0.4094	0.503	—	0.5666	0.560
$w_{sum,ant}$	-0.7799	-0.0632	-0.1304	0.891	0.56661	—	0.876
$w_{sum,rad}$	-0.7002	-0.1906	-0.1926	0.957	0.55978	0.8764	—
$w_{sum,uln,max}$	-0.4850	0.1593	0.3563	0.635	0.90618	0.7144	0.631
$A_{res}$	-0.7659	-0.0432	0.1459	0.934	0.65017	0.8732	0.894
$A_{nores}$	-0.7670	-0.0637	0.1389	0.936	0.63611	0.8690	0.896
$w_{total,RA}$	0.0849	0.1851	0.7075	-0.366	-0.00292	-0.2269	-0.418
$w_{uln,RA}$	-0.3793	0.2885	0.3046	0.147	0.35145	0.3203	0.113
$w_{rad,RA}$	-0.6789	-0.2939	-0.3732	0.944	0.32516	0.8420	0.940
$\sum s''$	0.3711	0.6957	0.6391	-0.495	0.01722	-0.4190	-0.516
$L_{a,traced}$	0.3965	0.7123	0.6170	-0.470	0.02887	-0.4106	-0.501
$L_{a,poly}$	0.4011	0.7123	0.6231	-0.471	0.03483	-0.4135	-0.500
<b>Nodes</b>	0.3586	0.7549	0.5340	-0.384	0.06817	-0.3245	-0.428
$\max(r)$	0.2739	0.6070	0.6365	-0.555	0.10977	-0.4347	-0.580
$\bar{r}$	0.0805	0.8087	0.4301	-0.330	0.26729	-0.1696	-0.314
$\frac{L_{a,fit}}{L_{a,traced}}$	0.1657	0.8999	0.3387	-0.187	0.29950	-0.0778	-0.190
95% quantile of $r$	0.0910	0.7018	0.5424	-0.448	0.19996	-0.2765	-0.453
<b>Scalloping</b>	0.2114	0.2641	-0.0766	-0.518	-0.34433	-0.4061	-0.447
$A_{scalloping}$	0.3911	0.8301	0.4469	-0.453	0.08270	-0.3779	-0.505

Table C.4: Correlation between measured endpoint variables. The values are the mean correlation for all bones.

	$W_{\text{sum,uln,max}}$	$A_{\text{res}}$	$A_{\text{nores}}$	$W_{\text{total,RA}}$	$W_{\text{uln,RA}}$	$W_{\text{rad,RA}}$	$\sum s''$
<b>Age</b>	-0.4850	-0.76590	-0.7670	0.0849	-0.379	-0.679	0.3711
<b>Status</b>	0.15935	-0.04317	-0.0637	0.18512	0.289	-0.294	0.6957
$w_{\text{total}}$	0.35631	0.14594	0.1389	0.70753	0.305	-0.373	0.6391
$w_{\text{sum,pos}}$	0.63476	0.93381	0.9362	-0.36617	0.147	0.944	-0.4948
$w_{\text{sum,uln}}$	0.90618	0.65017	0.6361	-0.00292	0.351	0.325	0.0172
$w_{\text{sum,ant}}$	0.71437	0.87318	0.8690	-0.22692	0.320	0.842	-0.4190
$w_{\text{sum,rad}}$	0.63147	0.89438	0.8964	-0.41821	0.113	0.940	-0.5160
$w_{\text{sum,uln,max}}$	—	0.76197	0.7494	0.07286	0.484	0.482	-0.0929
$A_{\text{res}}$	0.76197	—	0.9992	-0.16472	0.190	0.803	-0.2348
$A_{\text{nores}}$	0.74938	0.99924	—	-0.17704	0.172	0.807	-0.2496
$w_{\text{total,RA}}$	0.07286	-0.16472	-0.1770	—	0.641	-0.395	0.6722
$w_{\text{uln,RA}}$	0.48407	0.19000	0.1724	0.64096	—	0.171	0.2436
$w_{\text{rad,RA}}$	0.48169	0.80253	0.8068	-0.39491	0.171	—	-0.6055
$\sum s''$	-0.09293	-0.23484	-0.2496	0.67218	0.244	-0.605	—
$L_{a,\text{traced}}$	-0.08644	-0.21471	-0.2282	0.63729	0.218	-0.591	0.9926
$L_{a,\text{poly}}$	-0.08368	-0.21477	-0.2285	0.63812	0.217	-0.593	0.9934
<b>Nodes</b>	-0.03292	-0.14824	-0.1601	0.55998	0.231	-0.510	0.9545
$\max(r)$	0.00748	-0.33017	-0.3520	0.68162	0.346	-0.681	0.8501
$\bar{r}$	0.15898	-0.14268	-0.1710	0.51578	0.439	-0.424	0.8003
$\frac{L_{a,\text{fit}}}{L_{a,\text{traced}}}$	0.17698	0.00712	-0.0152	0.33983	0.286	-0.308	0.8102
95% quantile of $r$	0.11046	-0.23243	-0.2572	0.60043	0.401	-0.564	0.8088
<b>Scalloping</b>	-0.44482	-0.53181	-0.5475	0.27125	0.104	-0.445	0.4243
$A_{\text{scalloping}}$	-0.01546	-0.24157	-0.2615	0.48323	0.223	-0.579	0.9176

Table C.5: Correlation between measured endpoint variables. The values are the mean correlation for all bones.

	$L_{a,\text{traced}}$	$L_{a,\text{poly}}$	<b>Nodes</b>	$\max(r)$	$\bar{r}$	$\frac{L_{a,\text{fit}}}{L_{a,\text{traced}}}$
<b>Age</b>	0.3965	0.4011	0.3586	0.27390	0.080	0.16570
<b>Status</b>	0.7123	0.7123	0.7549	0.60703	0.809	0.89994
$w_{\text{total}}$	0.6170	0.6231	0.5340	0.63654	0.430	0.33873
$w_{\text{sum,pos}}$	-0.4699	-0.4714	-0.3843	-0.55458	-0.330	-0.18704
$w_{\text{sum,uln}}$	0.0289	0.0348	0.0682	0.10977	0.267	0.29950
$w_{\text{sum,ant}}$	-0.4106	-0.4135	-0.3245	-0.43465	-0.170	-0.07776
$w_{\text{sum,rad}}$	-0.5006	-0.4997	-0.4281	-0.57958	-0.314	-0.18973
$w_{\text{sum,uln,max}}$	-0.0864	-0.0837	-0.0329	0.00748	0.159	0.17698
$A_{\text{res}}$	-0.2147	-0.2148	-0.1482	-0.33017	-0.143	0.00712
$A_{\text{nores}}$	-0.2282	-0.2285	-0.1601	-0.35201	-0.171	-0.01524
$w_{\text{total,RA}}$	0.6373	0.6381	0.5600	0.68162	0.516	0.33983
$w_{\text{uln,RA}}$	0.2179	0.2174	0.2314	0.34561	0.439	0.28631
$w_{\text{rad,RA}}$	-0.5915	-0.5933	-0.5102	-0.68073	-0.424	-0.30824
$\sum s''$	0.9926	0.9934	0.9545	0.85008	0.800	0.81021
$L_{a,\text{traced}}$	—	0.9998	0.9791	0.83772	0.796	0.83871
$L_{a,\text{poly}}$	0.9998	—	0.9764	0.84093	0.798	0.83786
<b>Nodes</b>	0.9791	0.9764	—	0.77734	0.780	0.88322
$\max(r)$	0.8377	0.8409	0.7773	—	0.896	0.73970
$\bar{r}$	0.7955	0.7979	0.7805	0.89561	—	0.91005
$\frac{L_{a,\text{fit}}}{L_{a,\text{traced}}}$	0.8387	0.8379	0.8832	0.73970	0.910	—
95% quantile of $r$	0.7929	0.7954	0.7513	0.96564	0.958	0.80860
<b>Scalloping</b>	0.4040	0.4028	0.3614	0.42747	0.479	0.36612
$A_{\text{scalloping}}$	0.9310	0.9302	0.9377	0.85487	0.873	0.91541

Table C.6: Correlation between measured endpoint variables. The values are the mean correlation for all bones.

	95% quantile of $r$	Scalloping	$A_{\text{scalloping}}$
<b>Age</b>	0.091	0.2114	0.3911
<b>Status</b>	0.702	0.2641	0.8301
$w_{\text{total}}$	0.542	-0.0766	0.4469
$w_{\text{sum,pos}}$	-0.448	-0.5184	-0.4526
$w_{\text{sum,ulh}}$	0.200	-0.3443	0.0827
$w_{\text{sum,ant}}$	-0.276	-0.4061	-0.3779
$w_{\text{sum,rad}}$	-0.453	-0.4472	-0.5049
$w_{\text{sum,ulh,max}}$	0.110	-0.4448	-0.0155
$A_{\text{res}}$	-0.232	-0.5318	-0.2416
$A_{\text{nores}}$	-0.257	-0.5475	-0.2615
$w_{\text{total,RA}}$	0.600	0.2712	0.4832
$w_{\text{ulh,RA}}$	0.401	0.1045	0.2233
$w_{\text{rad,RA}}$	-0.564	-0.4452	-0.5786
$\sum s''$	0.809	0.4243	0.9176
$L_a, \text{traced}$	0.793	0.4040	0.9310
$L_a, \text{poly}$	0.795	0.4028	0.9302
<b>Nodes</b>	0.751	0.3614	0.9377
$\max(r)$	0.966	0.4275	0.8549
$\bar{r}$	0.958	0.4794	0.8734
$\frac{L_a, \text{fit}}{L_a, \text{traced}}$	0.809	0.3661	0.9154
95% quantile of $r$	—	0.4232	0.8514
<b>Scalloping</b>	0.423	—	0.3954
$A_{\text{scalloping}}$	0.851	0.3954	—

Table C.7: Correlation between measured endpoint variables. The values are the mean correlation for all bones.

## C.2.2 Correlation plots

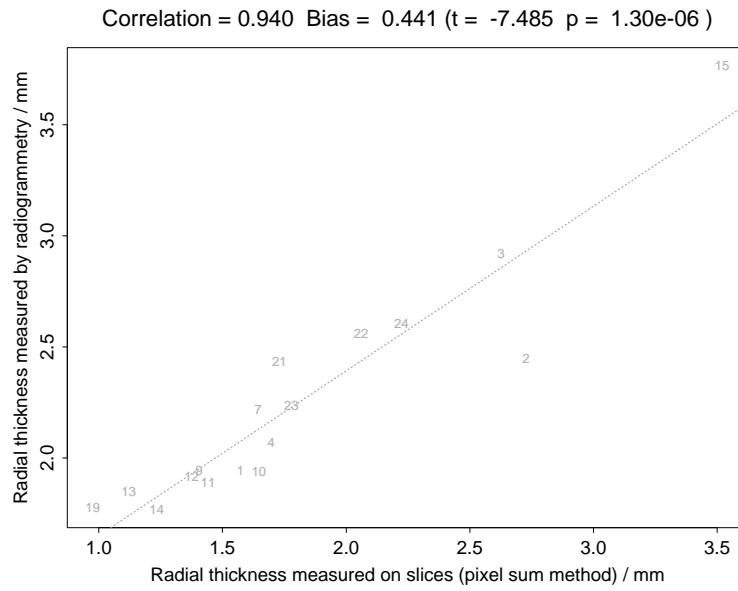


Figure C.18: Radial thickness measured on slices and by radiogrammetry.

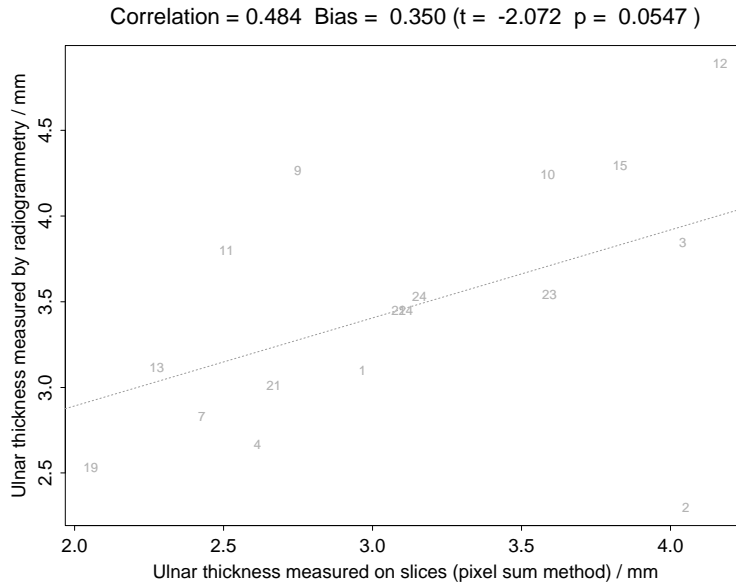


Figure C.19: Ulnar thickness measured on slices and by radiogrammetry.

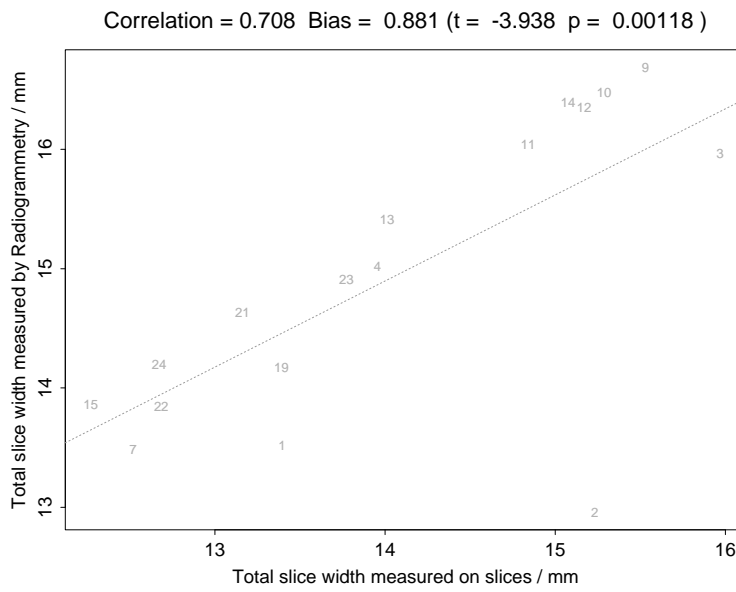


Figure C.20: Total slice width measured on slices and by radiogrammetry.

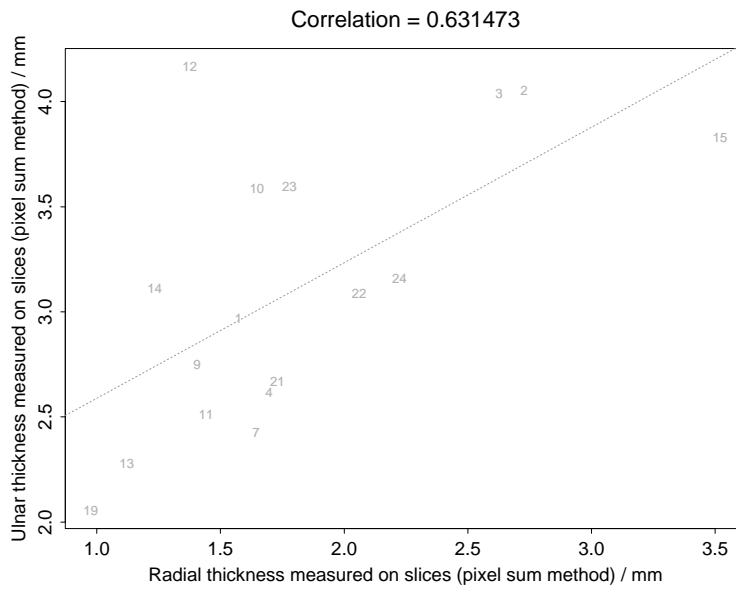


Figure C.21: Radial and ulnar thicknes measured on slices.

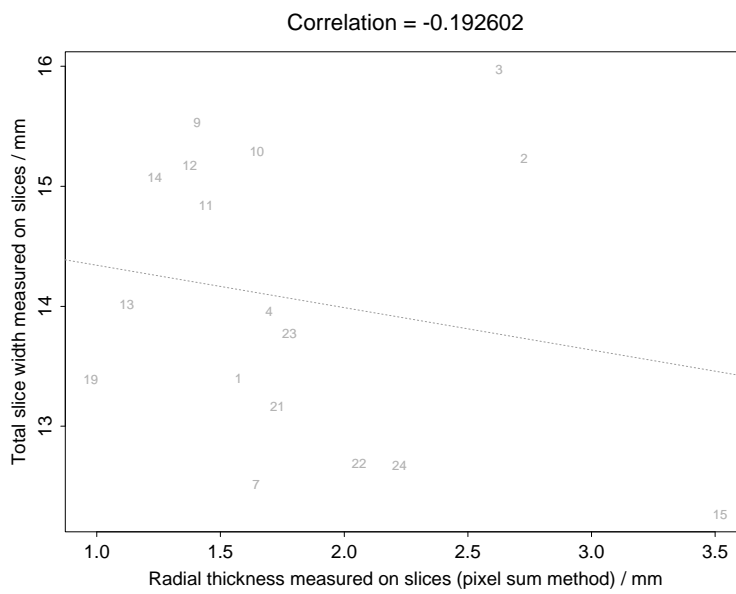


Figure C.22: Radial thicknes and total slice width measured on slices.

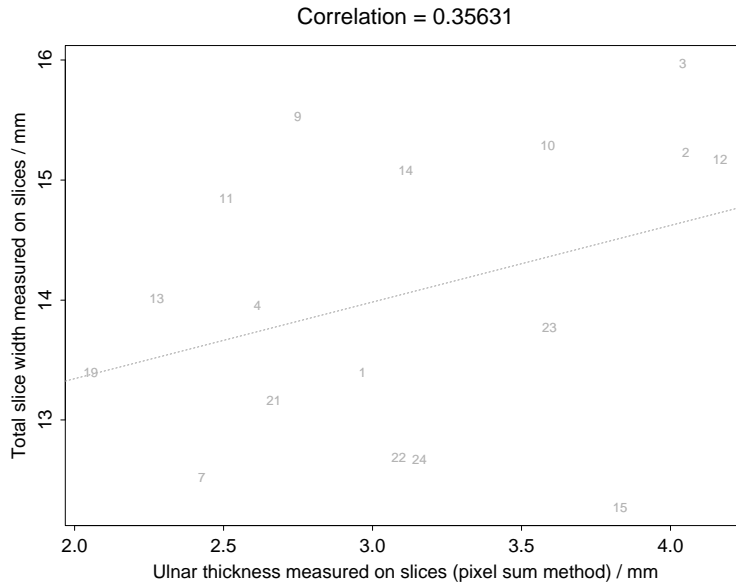


Figure C.23: Ulnar thicknes and total slice width measured on slices.

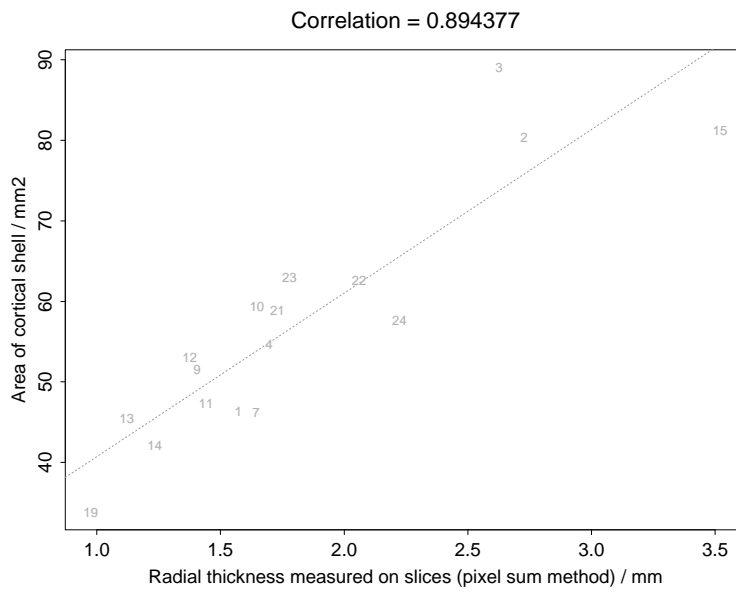


Figure C.24: Radial thicknes and cortical shell area measured on slices.



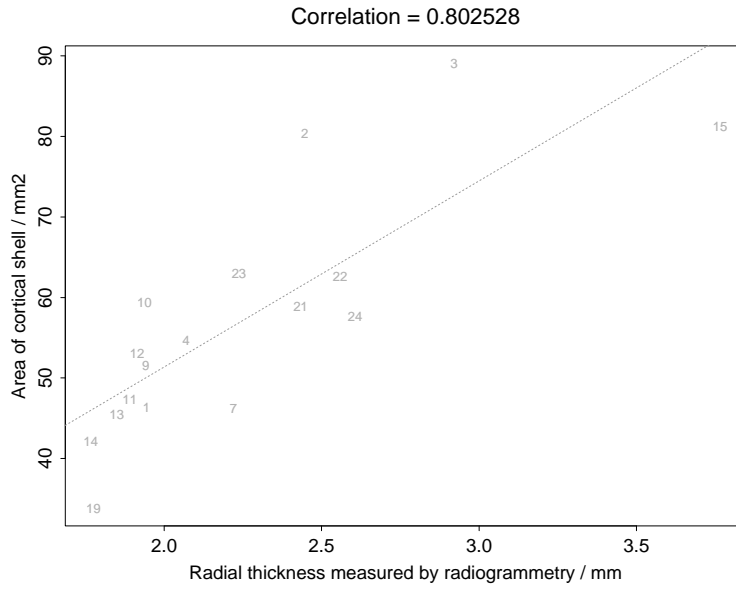


Figure C.25: Radial thicknes measured by radiogrammetry and cortical shell area measured on slices.

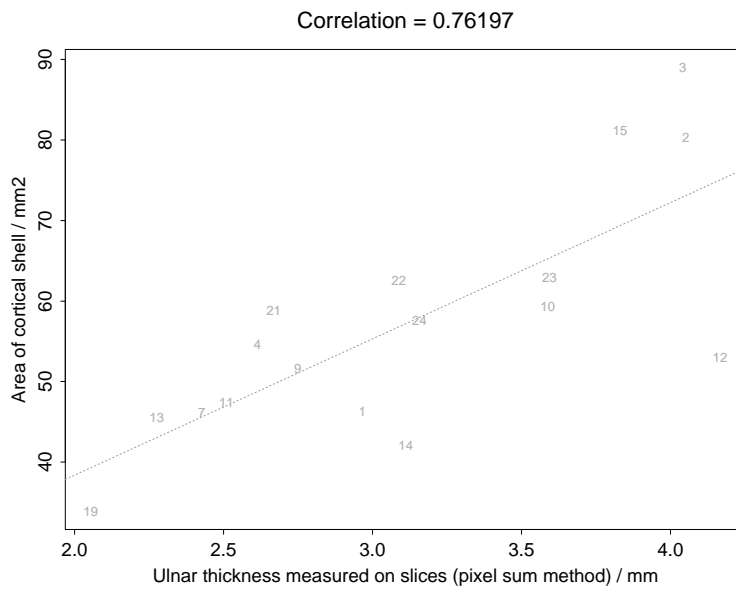


Figure C.26: Ulnar thicknes and cortical shell area measured on slices.

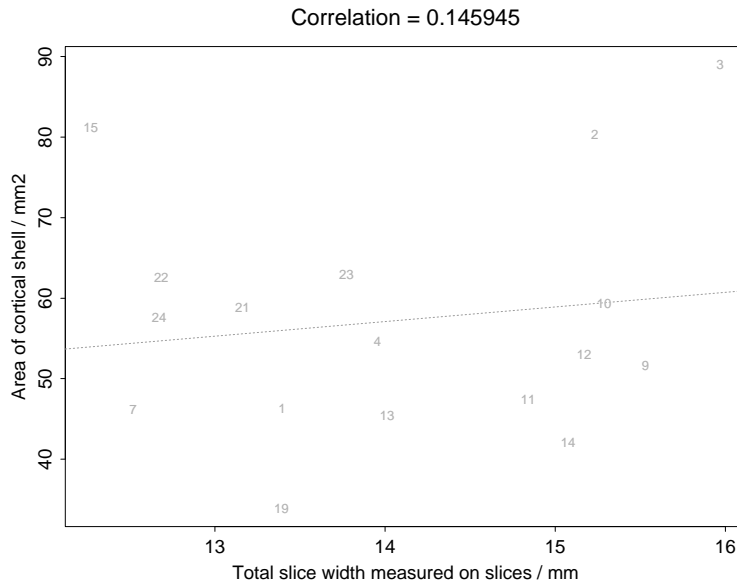


Figure C.27: Total slice width and cortical shell area measured on slices.

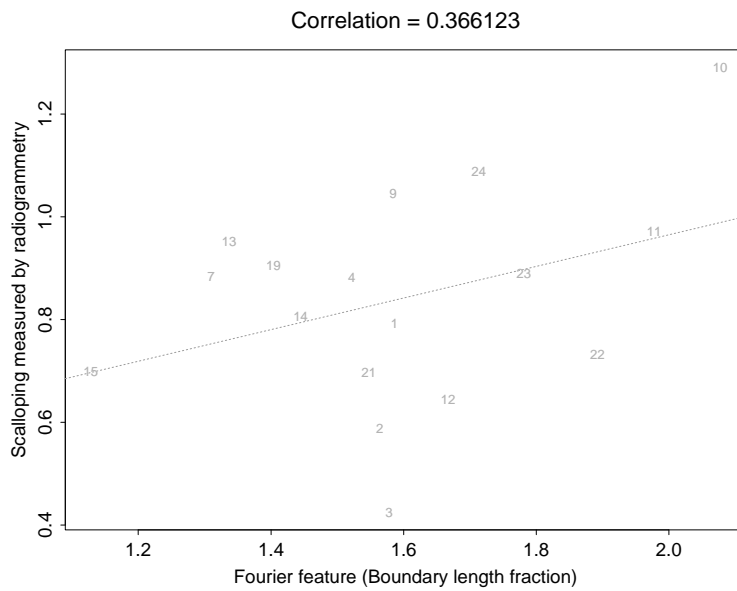


Figure C.28: Fourier feature (arlength fraction) measured on slices and scalping measured by radiogrammetry.

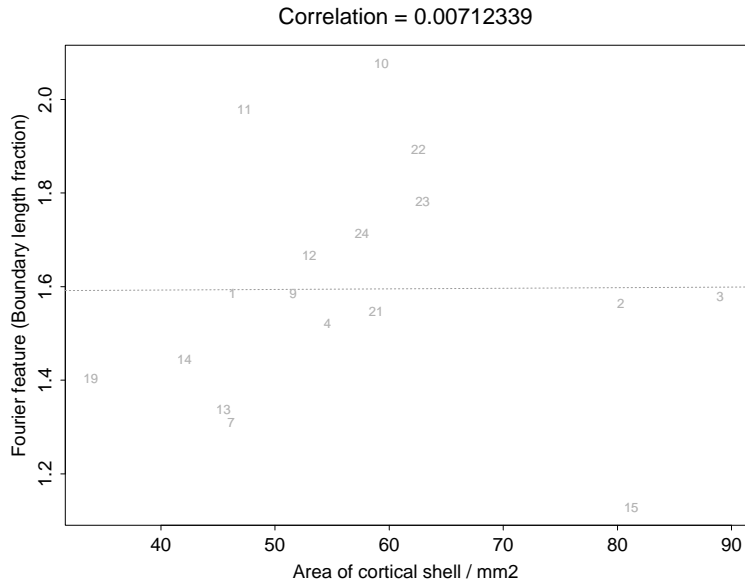


Figure C.29: Cortical shell area measured on slices and fourier feature (arclength fraction) measured on slices.

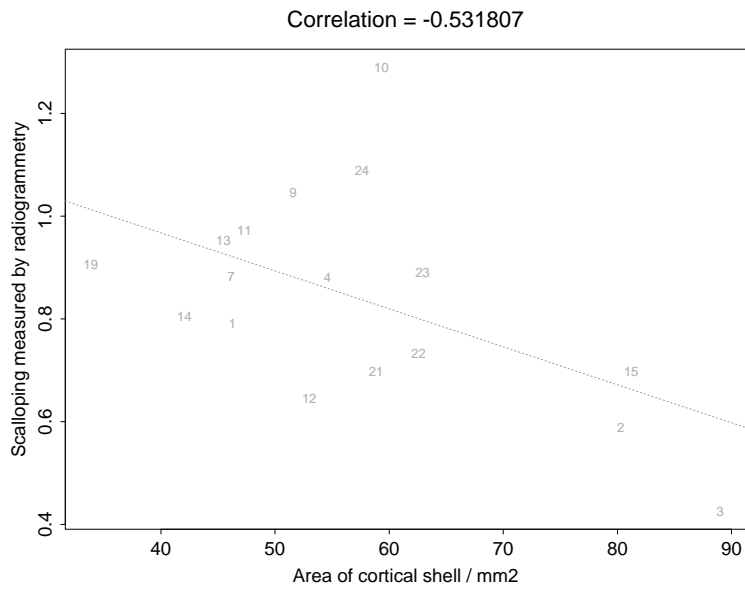


Figure C.30: Cortical shell area measured on slices and scalping measured by radiogrammetry.

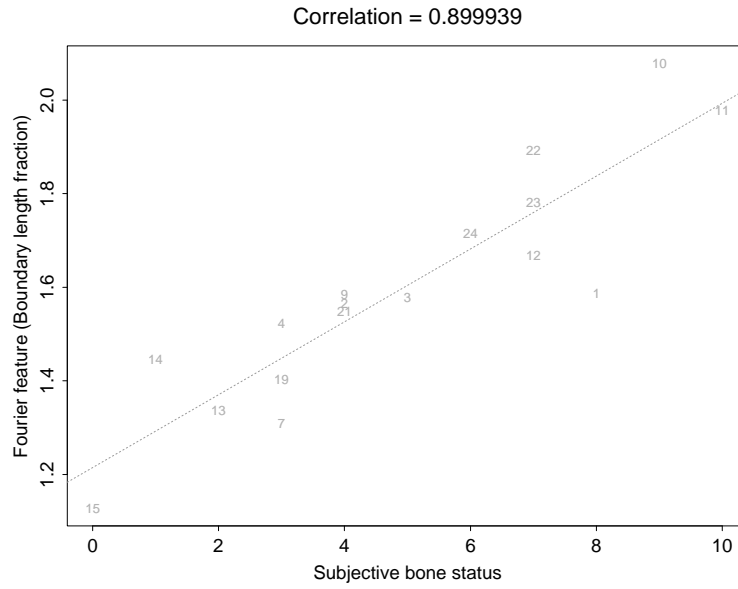


Figure C.31: Subjective bone status and fourier feature (arclength fraction) measured on slices.

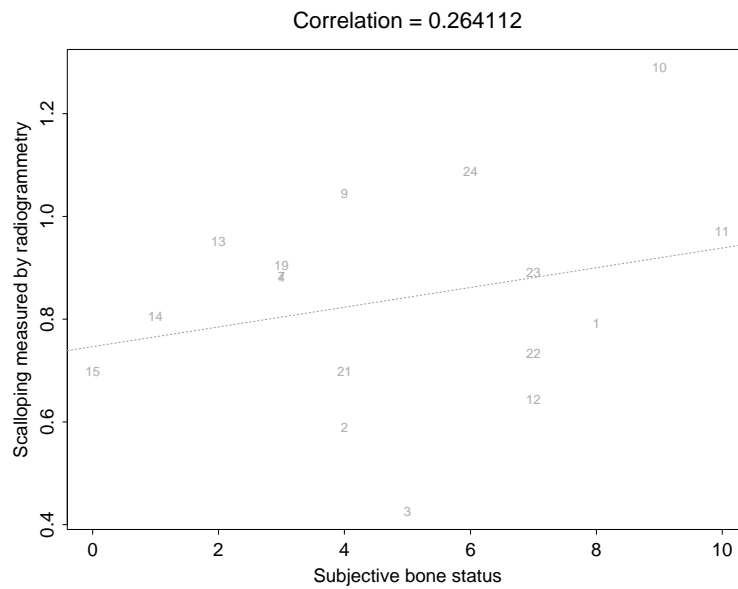


Figure C.32: Subjective bone status and scalping measured by radiogrammetry.

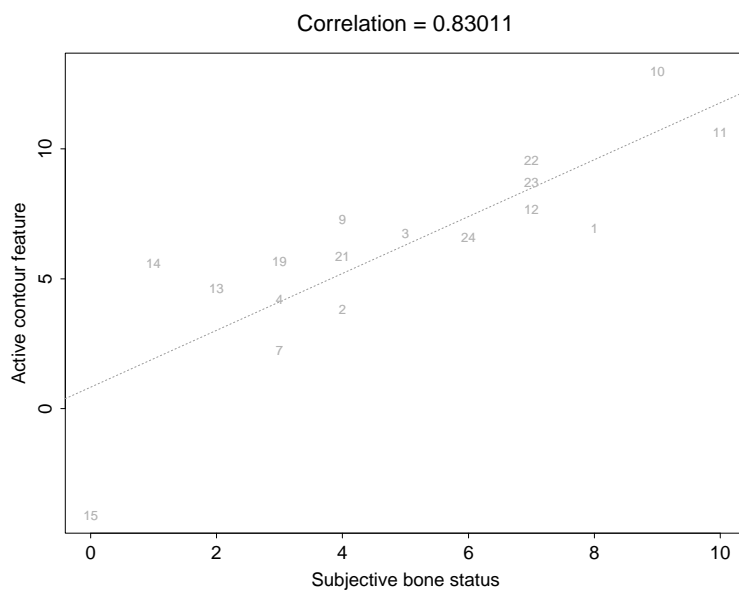


Figure C.33: Subjective bone status and active contour feature on slices.

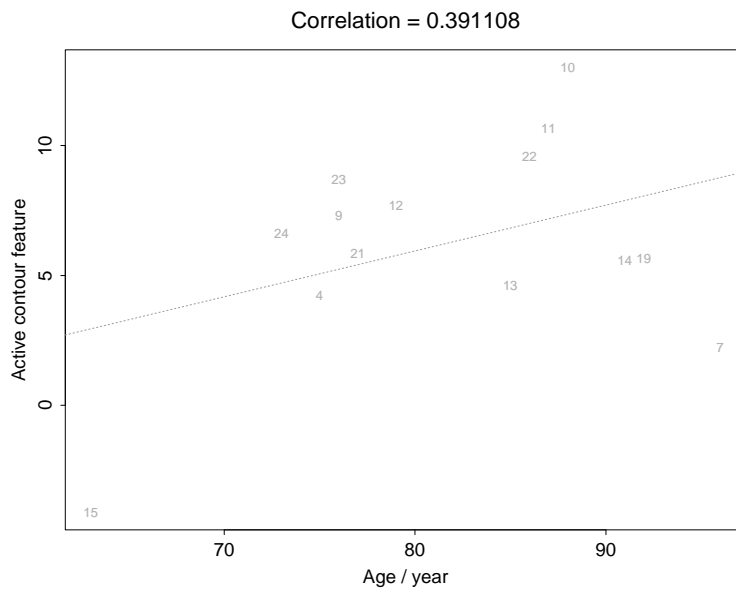


Figure C.34: Age and active contour feature on slices.

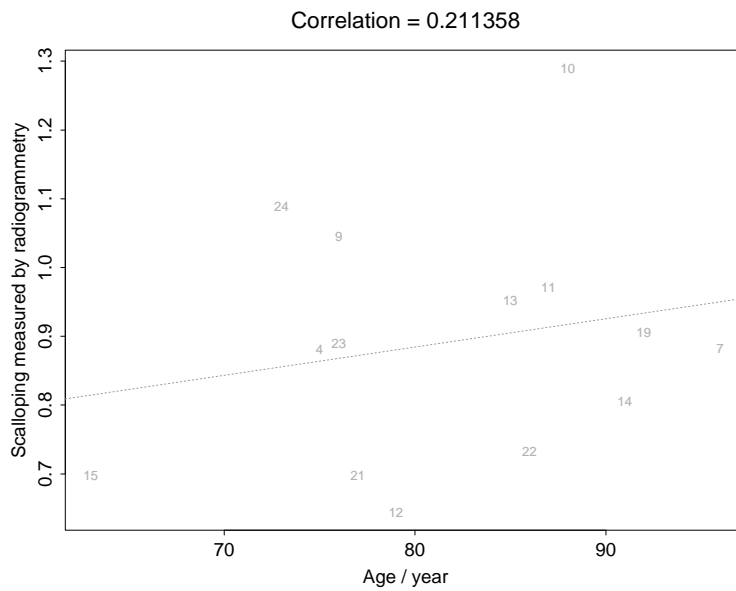


Figure C.35: Age and scalloping measured by radiogrammetry.

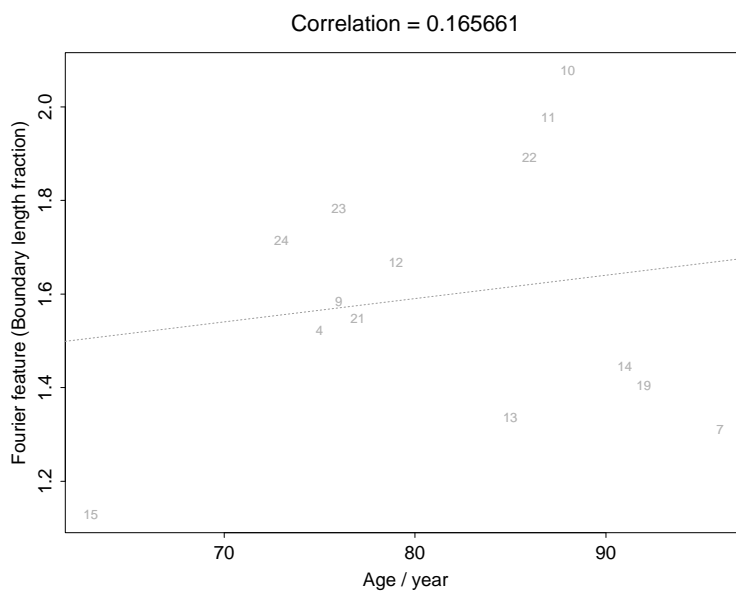


Figure C.36: Age and fourier feature (arlength fraction) measured on slices.

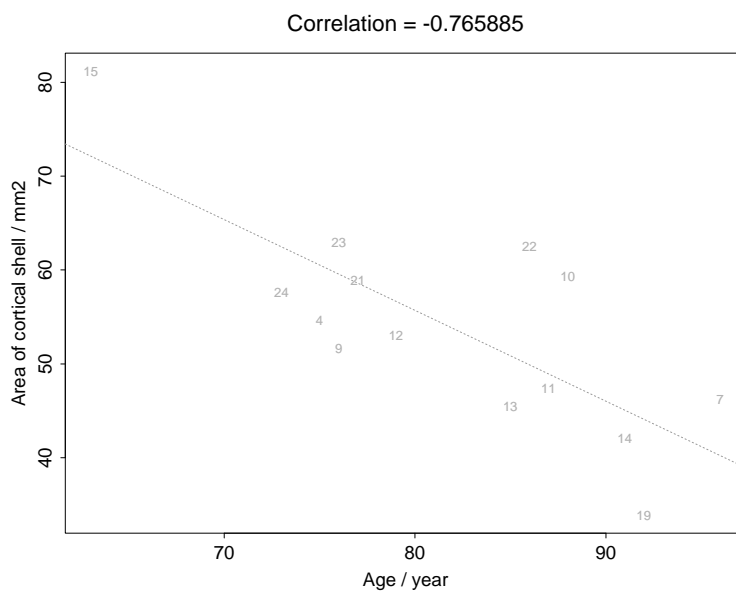


Figure C.37: Age and cortical shell area measured on slices.



## Appendix D

# C++ image class library

This appendix presents an image class library. Three types of images byte, int and float images are supported. The image classes support reading of images from file (HIPS1 and HIPS2 format) and writing of images to file.

The virtual base class `CImg` is inherited by the three derived classes `CImgByte`, `CImgInt` and `CImgFloat` as seen in figure D.1.

First the two tool classes `CImgLog` and `CImgExc` are described.

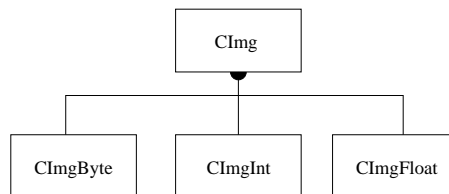


Figure D.1: The image classes.

### D.1 CImgLog

Communication class. Used for writing text messages. On UNIX and Windows 95 and Windows Nt consoles the messages are shown on `stderr`. In the MFC shell the messages are shown in a special window. A verbosity level is defined at construction time. When writing a message a verbosity level is given, the message is shown if the given level is below or equal to the current log verbosity.

#### D.1.1 Public member functions

```
CImgLog(int verbose = 2)
```

Constructs a log object.

```
Write(char * text, int level = 2)
```

Writes text if level is equal or lower than log verbosity level.

```
quiet()
```

All messages with verbosity level greater than 0 will be suppressed.

```
verbose()
```

The log verbosity level is set back to normal.

```
setlevel(int level)
```

Set log verbosity level.

### D.1.2 Example

```
#include "cimlog.h"
main()
{
    CImgLog Log(3);
    Log.Write("I will be shown\n",2);
    Log.Write("You can't see me\n",10);
    Log.setlevel(12);
    Log.Write("Now you can see me\n",10);
    Log.quiet();
    Log.Write("I'm invisible !\n",1);
}
```

## D.2 CImgExc

Exception class. Used for reporting program errors.

### D.2.1 Public member functions

```
CImgExc(char * cause)
```

Constructs an exception object.

### D.2.2 Public member variables

```
char m_cause[400];
```

Textual description of error encountered.

### D.2.3 Example

```
#include "cimglog.h"
#include "cimgexc.h"

main()
{
    CImgLog Log(10);

    try
    {
        Log->Write("You will see mee\n",2);

        throw CImgExc("I'm an exception");

        Log->Write("You will not see mee\n",2);
    }

    catch (CImgExc e)
    {
        Log.write("Error : ",0);
        Log.write(e.m_cause, 0);
        Log.write("\n", 0);
    }
}
```

## D.3 CImgByte

Byte image class. All errors encountered will be thrown as `CImgExc` exceptions.

### D.3.1 Public member functions

```
CImgByte(CImgLog * l = NULL);
```

Constructs image with no allocated image data. Use `ReadImg` to get image data.

```
CImgByte(char * imgname, CImgLog * l = NULL);
```

Constructs image and read image data from file.

```
CImgByte(int rows, int cols, CImgLog * l = NULL);
```

Constructs image with given size. Image data undefined.

```
CImgByte(CImgByte * img, CImgLog * l = NULL);
```

Constructs image from another byte image. Image data is copied.

```
CImgByte(CImgInt * img, CImgLog * l = NULL);
```

Constructs image from int image. Image data is converted and copied.

```
CImgByte(CImgFloat * img, CImgLog * l = NULL);
```

Constructs image from float image. Image data is converted and copied.

```
void s(int r, int c, BYTE val);
```

Set pixel value at position (r,c) to val.

```
BYTE v(int r, int c);
```

Get pixel value at position (r,c).

```
BYTE * getPixels();
```

Get pointer to pixels. This is a function made for backward compatibility. Should not be used in newer programs.

```
BYTE ** getMatrix();
```

Get pointer to pixel lookup table as defined by Anders Rosholm. This is a function made for backward compatibility. Should not be used in newer programs.

```
void WriteImg(char * imgname);
```

Writes image to file. Supported format: HIPS.

```
int cols();
```

Get number of columns of image.

```
int rows();
```

Get number of rows of image.

```
void ReadImg(char * imgname);
```

Read image from file. Image data is converted. Supported format: HIPS.

### D.3.2 Example

```
#include "cimlog.h"
#include "cimgexc.h"
#include "cimbyte.h"

main()
{
    CImgLog Log(10);

    try
    {
        // Construct integer image and read it from file
        CImgInt img1("test.hips", &Log);

        // Construct byte image from integer image
        CImgByte img2(&img1, &Log);

        // invert image
        for (int r = 0; r < img2.rows(); r++)
            for (int c = 0; c < img2.cols(); c++)
                img2.s(r, c, 255-img2.v(r,c));

        // write it to file
        img2.WriteImg("test.inv.hips");
    }
    // catch exception and write message on the log
    catch (CImgExc e)
    {
        Log.write("Error : ",0);
        Log.write(e.m_cause, 0);
        Log.write("\n", 0);
    }
}
```

## D.4 CImgFloat

Float image class. All errors encountered will be thrown as `CImgExc` exceptions.

### D.4.1 Public member functions

```
CImgFloat(CImgLog * l = NULL);
```

Constructs image with no allocated image data. Use `ReadImg` to get image data.

```
CImgFloat(char * imgname, CImgLog * l = NULL);
```

Constructs image and read image data from file.

```
CImgFloat(int rows, int cols, CImgLog * l = NULL);
```

Constructs image with given size. Image data undefined.

```
CImgFloat(CImgFloat * img, CImgLog * l = NULL);
```

Constructs image from another float image. Image data is copied.

```
CImgFloat(CImgInt * img, CImgLog * l = NULL);
```

Constructs image from int image. Image data is converted and copied.

```
CImgFloat(CImgByte * img, CImgLog * l = NULL);
```

Constructs image from byte image. Image data is converted and copied.

```
void s(int r, int c, float val);
```

Set pixel value at position (r,c) to val.

```
float v(int r, int c);
```

Get pixel value at position (r,c).

```
float * getPixels();
```

Get pointer to pixels. This is a function made for backward compatibility. Should not be used in newer programs.

```
float ** getMatrix();
```

Get pointer to pixel lookup table as defined by Anders Rosholm. This is a function made for backward compatibility. Should not be used in newer programs.

```
void WriteImg(char * imgname);
```

Writes image to file. Supported format: HIPS.

```
int cols();
```

Get number of columns of image.

```
int rows();
```

Get number of rows of image.

```
void ReadImg(char * imgname);
```

Read image from file. Image data is converted. Supported format: HIPS.

## D.4.2 Example

```
#include "cimlog.h"
#include "cimgexc.h"
#include "cimgfloat.h"

main()
{
    char names[ ][100]= {
        "test1.hips",
        "test3.hips",
        "test3.hips"};

    CImgLog Log(10);

    try
    {
        // Read 3 images with given names
        // Construct and destruct images dynamically
        for (int i = 0; i < 3; i++)
            CImgFloat img(name[i], &Log);
    }
    // catch exception and write message on the log
    catch (CImgExc e)
    {
        Log.write("Error : ",0);
        Log.write(e.m_cause, 0);
        Log.write("\n", 0);
    }
}
```

## D.5 CImgInt

Int image class. All errors encountered will be thrown as `CImgExc` exceptions.

### D.5.1 Public member functions

```
CImgInt(CImgLog * l = NULL);
```

Constructs image with no allocated image data. Use `ReadImg` to get image data.

```
CImgInt(char * imgname, CImgLog * l = NULL);
```

Constructs image and read image data from file.

```
CImgInt(int rows, int cols, CImgLog * l = NULL);
```

Constructs image with given size. Image data undefined.

```
CImgInt(CImgInt * img, CImgLog * l = NULL);
```

Constructs image from another int image. Image data is copied.

```
CImgInt(CImgFloat * img, CImgLog * l = NULL);
```

Constructs image from float image. Image data is converted and copied.

```
CImgInt(CImgByte * img, CImgLog * l = NULL);
```

Constructs image from byte image. Image data is converted and copied.

```
void s(int r, int c, int val);
```

Set pixel value at position (r,c) to val.

```
int v(int r, int c);
```

Get pixel value at position (r,c).

```
int * getPixels();
```

Get pointer to pixels. This is a function made for backward compatibility. Should not be used in newer programs.

```
int ** getMatrix();
```



Get pointer to pixel lookup table as defined by Anders Rosholm. This is a function made for backward compatibility. Should not be used in newer programs.

```
void WriteImg(char * imgname);
```

Writes image to file. Supported format: HIPS.

```
int cols();
```

Get number of columns of image.

```
int rows();
```

Get number of rows of image.

```
void ReadImg(char * imgname);
```

Read image from file. Image data is converted. Supported format: HIPS.

## D.5.2 Example

```
#include "cimlog.h"
#include "cimgexc.h"
#include "cimgint.h"

main()
{
    CImgLog Log(10);

    try
    {
        // Construct int image with dimensions (300,200)
        CImgInt img2(300,200, &Log);

        // call old style function
        // oldfunc(int * img, int rows, int cols);

        oldfunc(img2.getPixels(), img2.rows(), img2.cols());

        // call AR style function
        // ARfunc(int ** img, int rows, int cols);

        ARfunc(img2.getMatrix(), img2.rows(), img2.cols());
    }
    // catch exception and write message on the log
    catch (CImgExc e)
    {
        Log.write("Error : ",0);
        Log.write(e.m_cause, 0);
        Log.write("\n", 0);
    }
}
```

## Appendix E

# Developed Software

All software has been developed using C++. All image handling is done with the image classes described in chapter D.

Traditionally all image handling at IMM were done with the HIPS program library. This is a library of standard C routines and a library of image handling procedures.

A typical HIPS programs reads one or more images and returns one image. The programs are then combined into organized structures by Unix shell scripts.

Allocating and reading images from a HIPS program requires over 10 calls to the library.

The C++ language has some properties that are very suitable for constructing image based programs. As explained in the previous section an image is born as a natural C++ object.

Some of the advantages over standard HIPS (standard c) programming is:

- Object oriented programming.
- Easier error handling with C++ exceptions.
- Inheritance.
- Compiles well under UNIX and Windows NT,95.
- Read and write HIPS format images without needing the HIPS library.
- Creates, reads and writes image in a single line of code.
- Is not forced to be a collection of routines controlled by UNIX shell scrips.

Disadvantages

- Not possible to pipe images in and out of the programs. This is due to the structure of the image classes. The classes could be rewritten to make it possible, but since another program structure is chosen this is not optimal.

- Forced to compile the program when a change is made. On modern computer the compile time is around 5 seconds so this is not a major disadvantage.

Instead of describing algorithms and classes with a man page the prototypes and class declarations are explained.

All programs have been compiled successfully under Red Hat Linux 4.2 on a Pentium II, 300 Mhz with gcc version 2.7.2.1.

## E.1 Thresholding

### E.1.1 Source

The source files are:

- `h_authresh.h`
- `h_authresh.cpp`

### E.1.2 Prototypes

```
void meanThreshold(CImgLog * log, CImgByte * iimg,
                  CImgByte * oimg);
```

Calculates the iterative optimal threshold of image `iimg`. The thresholded image is returned in `oimg`.

```
void minObjThreshold(CImgLog * log, CImgByte * iimg,
                    CImgByte * oimg,
                    int nthresh, int method, int adjust);
```

Calculates `nthresh` thresholds in the input image `iimg`. The method is either minimum interclass variance (0) or minimum interclass sum of squares (1). `adjust` is a boolean that indicates whether recursive adjustment of thresholds should be applied each time a new threshold is added. The thresholded image is returned in `oimg`.

```
void minHistThreshold(CImgLog * log, CImgByte * iimg,
                     CImgByte * oimg);
```

Calculates the threshold as the histogram value with minimum between the two peaks in a bimodal histogram. Input image is `iimg` The thresholded image is returned in `oimg`.

## E.2 Connected Component Labeling

### E.2.1 Source

The source files are:

- `h_concomp.h`
- `h_concomp.cpp`

### E.2.2 Prototypes

```
void returnLargest(CImgLog * log, int **imgi, int **imgo,  
                 int nr, int nc,  
                 int *nclass, int con);
```

Returns the largest connected component of the input image `imgi`. Note that it is not an image class but an image matrix that is required, therefore the rows and columns of the image is needed. The parameter `con` determines if 4- or 8-connectivity shall be used. The number of classes in the image is returned.

```
void return2Largest(CImgLog * log, int **imgi, int **imgo,  
                  int nr, int nc,  
                  int *nclass, int con);
```

Returns the second largest connected component of the input image `imgi`.

```
void enumerateComponents(CImgLog * log, int **imgi,  
                        int **imgo, int nr, int nc,  
                        int *nclass, int con, int mincount,  
                        int * cr, int * cc, double * ncount);
```

Returns all connected components of the image, together with the number of classes found. The number of pixels in each class `ncount` and the upper left hand corner of the components `cr, cc` is also returned. A minimum size of the returned objects can be given.

## E.3 Boundary Tracing

### E.3.1 Source

The source files are:

- `h_traco.h`
- `h_traco.cpp`

### E.3.2 Prototypes

```
void traceObject(CImgLog * log, CImgByte * imgi,  
                CImgByte * imgo, int label, int mark, int * length);
```

Trace the outer boundary of the object (with label `label`) in the input image `imgi`. In the output image `imgo` the boundary is marked with pixel value `mark`. The length of the found boundary is returned.

```
void traceObjectPoly(CImgLog * log, CImgByte * imgi,  
                    CImgByte * imgo,  
                    int label, int mark, int * nodes,  
                    double * ArcLength,  
                    double * PolyArcLength,  
                    double * suma, double * BE, int stepsize,  
                    double maxd, double maxa);
```

Trace the outer boundary of the object (with label `label`) in the input image `imgi`. In the output image `imgo` the boundary is marked with pixel value `mark`. The polygonal approximation of the boundary is returned together with the sum of the second derivatives (boundary smoothness). `stepsize` is the number of points of the boundary used in each step of the polygonization, `maxd` is the max residual and `maxa` is the minimum angle two lines can have if they shall not be joined.

```
void traceObjectReturnArray(CImgLog * log, CImgByte * imgi,  
                            int label, CPtrArray * parray);
```

Trace the outer boundary of the object (with label `label`) in the input image `imgi`. The boundary is returned as a `CPtrArray` object.

### E.3.3 Point Class

A point class which stores a 2D position `CPoint` is implemented.

#### Source

The sourcefile is:

- `h_utility.h`

#### Public Member Functions

```
CPoint();
```

Default constructor. Creates a point with position (0,0).

```
CPoint(int tr, int tc);
```

Constructor. Creates a point with position (tr,tc).

### E.3.4 Point Array Class

A point array class `CPointArray` is implemented.

Points can be stored in the array which can be indexed as a normal array. The size of the array is dynamically changed if the current limit of points is exceeded.

If an error occurs a `CImgExc` exception is thrown.

#### Source

The source files are:

- `h_parray.h`
- `h_parray.cpp`

#### Public Member Functions

```
CPointArray(int size = 1000);
```

The array constructor. The initial size of the array can be given as parameter.

```
void setPoint(int n, const CPoint & p);
```

Sets the point at position `n` to a new value. If `n` is out of current array bounds the array is reallocated.

```
CPoint getPoint(int n);
```

Returns the point at position `n`. If `n` is out of array bounds an exception is thrown.

```
CPoint popPoint();
```

Returns the last point in the array. The number of points in the array is decreased by one. If the array is empty an exception is thrown.

```
void pushPoint(const CPoint & p);
```

Push a point on the array. If the array is too small it is reallocated and resized.

```
int last();
```

Return index of the last point in the array.

```
double ArcLength();
```

Calculate the arclength of the vector of points in the array.

## E.4 Polygonal Approximation

### E.4.1 Source

The source files are:

- `h_traco.h`
- `h_traco.cpp`

### E.4.2 Prototypes

```
void Polyfit(CImgLog * Log, CArray * ar, CArray * aro,  
            int stepsize, double maxd, double maxa)
```

Performs a polygonization of the points in the array `ar`, returns the result in `aro`. `stepsize` is the number of points of the boundary used in each step of the polygonization, `maxd` is the max residual and `maxa` is the minimum angle two lines can have if they shall not be joined.

## E.5 Cubic Convolution

### E.5.1 Source

The source files are:

- `h_warp.h`
- `h_warp.cpp`

### E.5.2 Prototypes

```
void Warp(CImgLog * Log, CImgFloat * imgi,  
         CImgFloat * imgo,  
         double theta, double transr, double transc, int pad);
```

Warp the input image `imgi`, return the result in `imgo`. The warping parameters are angle `theta`, translation `transr`, `transc`. The `pad` value shall also be given.

```
void MoveCenterOfMass(CImgLog * Log, CImgByte * imgi,  
                    CImgByte * imgo,  
                    int cmr, int cmc, int pad);
```

Translate the input image `imgi` with center of mass `cmr`, `cmc` so the center of mass is in the middle of the image. Return the result in `imgo`.

## E.6 Alignment by Steepest Descent

Note this algorithm is written in standard C.

- `h_regsteep.h`
- `h_regsteep.c`

### E.6.1 Prototypes

```
void Regsteep(struct report * rpt, float **imgi1,
              float **imgi2, float **imgo,
              int nr, int nc);
```

Uses a reference image `imgi1` and a source image `imgi2` the result is `imgo` which are the source image aligned with the reference image. The report struct is used for error reporting.

## E.7 Alignment with Boundary Descriptions

### E.7.1 Source

The source file is:

- `outline.cpp`

### E.7.2 Prototypes

```
void WarpSlices(CImgLog * Log)
```

This function is a part of a larger collection of routines called from the main program `outline`.

## E.8 Measuring Cortical Thickness

### E.8.1 Source

The source files are:

- `h_anglesp.h`
- `h_anglesp.cpp`



## E.8.2 Prototypes

```
void calcAngles(CImgLog * Log, CImgByte * img,
               int cmr,int cmc,
               double sa, double ea, int na,
               double *idar, double *odar);
```

Calculates the cortical thickness as the distance between the traced inner and outer boundaries of the cortical shell. The input image is `img` with center of mass `cmr,cmc`. Start angle `sa`, end angle `ea`, number of angles `na`. The distance from center of mass to the inner and outer boundary at the different angles are returned in two arrays `idar,odar` with length `na`.

```
void calcSumPixelAngles(CImgLog * Log, CImgByte * img,
                       int cmr,int cmc,
                       double sa, double ea, int na,
                       double *w);
```

Calculates the cortical thickness as the number of object pixels a line encounters from the center of mass to the boundary of the image. The input image is `img` with center of mass `cmr,cmc`. Startangle `sa`, endangle `ea`, number of angles `na`. The cortical width is returned in an array `w` with length `na`.

```
void calcHitAngles(CImgLog * Log, CImgByte * img,
                  int cmr,int cmc,
                  double sa, double ea, int na,
                  double *idar, double *odar);
```

Calculates the cortical thickness as the distance between the first and last object pixel hit by a line from the center of mass of the image.. The input image is `img` with center of mass `cmr,cmc`. Startangle `sa`, endangle `ea`, number of angles `na`. The distance from center of mass to the inner and outer boundary at the different angles are returned in two arrays `idar,odar` with length `na`.

## E.9 Simulated Radius

### E.9.1 The Simulated Profile Class

A C++ class `profileMatrix` for creating simulated radius from images of contact radiographs.

#### Source

The source files are:

- `h_simproj.h`
- `h_simproj.cpp`
- `simproj.cpp`

## Public Member Functions

```
profileMatrix(int nimg, int maxcol = 1000,  
             CImgLog * Log = NULL);
```

Creates a profile matrix. The parameters are the number of slices in the bone, the number of columns to be simulated and a Log object for writing messages.

```
void setVal(int img, int pos, double val);
```

Sets profile value for a given slice image and column position.

```
double getVal(int img, int pos);
```

Returns the profile value for a given slice image and column position.

```
void WriteProjektion(int n, char * fname);
```

Writes the computed projektion of an image slice to a file.

```
void DrawProjektion(int n, CImgByte * img, int mark);
```

Draws the computed projection of an image slice on an image.

```
void SimulatedProjektion(CImgByte * img, int n, double pos);
```

Computes the simulated projection of an image. Store it in the storage matrix at position defined by the image number `n` and column position `pos`.

```
void CreateRadius(CImgFloat * img, double startsim);
```

Creates a simulated radius. The starting position is determined by `startsim`. No interpolation between slices.

```
void CreateInterpolatedRadius(CImgFloat * img,  
                             double startsim, int markslice = 0);
```

Creates a simulated radius. The starting position is determined by `startsim`. Interpolation between slices. If `markslice` is equal to 1 the position of the slices are marked on the resulting simulated image.

## Example

In this example a series of 22 images named `slice0.hips` - `slice21.hips` are used to make a simulated radius. The routine is also given an array `place` with the vertical position relative to the fixpoint (in mm) of the slices.

```
// nslice : number of slices in serie
// lpmm : resolution of images, lines per mm
void CreateRadius(int nslice, int lpmm, double * place)
{
    // Create a log
    CImgLog Log(2);

    try
    {
        // get first image from serie
        // use it to get image dimensions
        CImgByte test("slice0.hips", &Log);

        profileMatrix pM(nslice, test.cols(), &Log);

        // run through all images in serie
        for (int i = 0; i < nslice; i++)
        {
            // create file name dynamically
            sprintf(name,"slice%d.hips", i);

            // read image from file
            CImgByte slice(name, Log);

            // create the simulated projektion from the slice
            pM.SimulatedProjektion(&slice, i, place[i]);

            // create file name dynamically
            sprintf(name,"slice%d.dat", i);

            // write projektion data to file
            pM.WriteProjektion(i, name);

            // draw the projektion on the original slice
            // with color number 10
            pM.DrawProjektion(i, &slice, 10);

            // write the image with the drawn projektion
            // to a file
            sprintf(name,"slice%d.proj.hips", i);
            slice.WriteImg(name);
        }

        // determine dimension of output image
        // start 25.0 mm from fixpoint
        // end 95.0 mm from fixpoint
        double start = lpmm*25.0;
        double end = lpmm*95.0;

        // create the output image
        CImgFloat sim((int)(end-start), test.cols(), &Log);

        // create the interpolated radius
        pM.CreateInterpolatedRadius(&sim, start/lpmm, 0);

        // Write the simulated projektion to file
        sim.WriteImg("simproj.hips");
    }

    // if anything goes wrong the error is
    // caught here
    catch (CImgExc e)
    {
        Log.write("Error : ",0);
        Log.write(e.m_cause, 0);
        Log.Write("\n", 0);
    }
}
```

```

    }
}

void main(void)
{
    // position of slices
    double place[22];

    //
    // create the place
    // this routine is trivial and is not shown
    calculatePlaces(22, place);

    // create the radius
    CreateRadius(22, 50, place);
}

```

## E.10 Boundary fitting by the Fast Fourier Transform

### E.10.1 The Fourier Feature Class

A C++ class `CFourFeature` that does Fourier transform and the inverse of a series of polar coordinates of a boundary. The class can also calculate several features from the Fourier series. If an error occurs in any of the functions in the class a `CImgExc` exception is thrown.

#### Source

The source files are:

- `h_fourtr.hpp`
- `cfourfeat.hpp`
- `cfourfeat.cpp`
- `cortex.cpp`
- `fourdemo.cpp`

#### Public Member Functions

```

CFourFeature(CImgByte * inner, CImgByte * total,
             CImgByte * inhole, CImgLog * Log,
             int low = 1, int high = 6);

```

Constructor. Creates an instance of a `CFourFeature` object. The images needed are the traced medullary area (`inner`) the traced endosteal and periosteal surface (`total`) and the medullary area as one connected component. A log is used for messages to the user. The low and high frequencies of the bandpass filter can be given. The Fourier series is calculated and the bandpass filtered version of the boundary description is also calculated here. The residual between the traced boundary and the bandpass filtered boundary is also calculated.

```
void WriteFourier(char * name);
```

Writes the powerspektrum of the Fourier series to a file.

```
void WriteSeries(char * name);
```

Writes the representation of the inner and outer boundary and the bandpass filtered inner boundary representation to a file.

```
void ShowSeries(CImgByte * img, int mark1, int mark2,  
               int mark3, int mark4);
```

The boundary description and the bandpassed inner boundary description is shown on the supplied image. Four colours shall be given.

```
void WriteResiduals(char * name);
```

Writes the residuals of the original and fitting line to a file.

```
double MeanResidual();
```

The mean of the residuals

```
double MaxResidual();
```

Max residual.

```
double ResidualFractile(double fract);
```

Fractile of residual.  $\text{fract} \in [0, 1[$

```
double ArcLengthFraction();
```

Arclength of the traced inner boundary divided by the arclength of the Fourier fitted inner boundary.

### **Example**

In this example the Fourier fitted boundary of an image is computed and the calculated features are shown to the user.

```

#include <stdio.h>
#include <stdlib.h>
#include "cimgexc.h"
#include "cimglog.h"
#include "cimgbyte.h"
#include "cfourfeat.hpp"

// The demo assumes that three images have been precalculated
// by other programs:
//
// The traced inner boundary (inner.hips)
// The traced inner and outer boundary (total.hips)
// The medullary area as one connected component (inhole.hips)

void FourierDemo(CImgLog * Log)
{
    // Read the traced inner boundary from file
    CImgByte inner("inner.hips", Log);

    // Read the traced inner and outer boundary from file
    CImgByte total("total.hips", Log);

    // Read the medullary area image from file
    CImgByte inhole("inhole.hips", Log);

    // Construct CFourFeature object and
    // Calculate fourier features
    CFourFeature fourfeature(&inner, &total, &inhole, Log);

    // Calculate the fourier features
    double maxres = fourfeature.MaxResidual();
    double meanres = fourfeature.MeanResidual();
    double ALfrac = fourfeature.ArcLengthFraction();
    double Fract95 = fourfeature.ResidualFractile(0.95);

    char buf[200];
    // Write the calculated features
    sprintf(buf, "maxres %5.3f meanres %5.3f ALfrac %5.3f Fractile(95) %5.3f\n",
            maxres, meanres, ALfrac, Fract95);
    Log->write(buf,1);

    // Write found series to data file
    fourfeature.WriteSeries("fourierseries.dat");

    // Create clean image with the same dimensions as inner.hips
    CImgByte show(inner.rows(), inner.cols(), Log);

    // show the found series on image.
    // with colors 255,160,200 and 255
    fourfeature.ShowSeries(&show, 255,150,200,255);

    // Write this image to file
    show.WritImg("fouriershow.hips");
}

main(void)
{
    // Create log for writing messages
    CImgLog Log(3);

    // Use exception handling to catch errors
    try
    {
        FourierDemo(&Log);
    }
    catch (CImgExc e)
    {
        Log.write("Error : ",0);
        Log.write(e.m_cause, 0);
        Log.write("\n",0);
    }
}

```

## E.11 Active nets, Balloons and Contours

In this section the three different active contour models implementation are documented.

### E.11.1 The Active Net Class

An active net C++ class `CAnet` has been developed. The class contains all information of the net. The net is initialized when an instance of the class is constructed. An iteration of the net is performed when the member function `MinizeEnergy` is called. If an error occurs in any of the functions in the class, a `CImgExc` exception is thrown.

#### Source

The source files are:

- `h_anet.h`
- `h_anet.cpp`
- `actnetdemo.cpp`
- `actnet.cpp`

#### Public Member Functions

```
CAnet(const CPoint &UL, const CPoint &LR, const int &nr,  
      const int &nc, CImgByte * inner, CImgByte * outer,  
      double alpha, double beta, double omega,  
      double rho, int prob, CImgLog * Log = NULL);
```

Constructor. The arguments are the upper left corner and lower right corner of the initial position of the net, the number of vertical and horizontal nodes, the image used for calculating the energies of the inner nodes and the image used for calculating the energies of the outer nodes. The remaining parameters are explained in section 6.1.

```
virtual void ShowNet(CImgByte &img, const int &mark);
```

Shows the net on the input image with the given color.

```
virtual void ShowNetOutline(CImgByte &img, const int &mark);
```

Shows the outline of the net on the input image with the given color.

```
double OuterBoundaryLength();
```

Calculates the arclength of the outer boundary of the net.

```
int MinimizeEnergy();
```

Performs one iteration of the minimization of the energi of the net. If no change in energy is noted the result is (0) else it is (1).

## Example

In this example an active net is used to locate the outer boundary of an object. The example assumes that an image of the medullary area `inner.hips` and the original image `original.hips` are present.

```
#include "cimgbyte.h"
#include "cimgexc.h"
#include "cimglog.h"
#include "h.anet.h"

void makeActiveNet(CImgLog * Log)
{
    // show that we are alive
    Log->write("makeActiveNet\n",2);

    // read image with medullary area
    CImgByte inner("inner.hips", Log);

    // and invert it.
    inner.Invert();

    // read image with medullary area
    CImgByte outer("inner.hips", Log);

    // parameters used
    double alpha = 4;
    double beta = 15;
    double omega = 30;
    double rho = 1;
    int prob = 5;

    // construct active net object
    CAnet anet(CPoint(10, 10),
              CPoint(inner.rows()-10, inner.cols()-10),
              20, 20,
              &inner, &outer,
              alpha, beta, omega, rho, prob, Log);

    // iterate 1500 times or until no change in energy
    int ok = 0;
    for (int it = 0; it < 1500 && !ok; it++)
    {
        ok = !anet.MinimizeEnergy();
    }

    // read original image
    CImgByte org("original.hips", Log);

    // show the net on the original
    anet.ShowNet(org, 0);

    // write the net image
    org.Writelmg("net.hips");
}

main(void)
{
```



```

CImgLog Log(2);

try
{
    makeActiveNet(&Log);
}
catch (CImgExc e)
{
    Log.write("Error : ",0);
    Log.write(e.m_cause, 0);
    Log.write("\n",0);
}
}

```

### E.11.2 The Active Balloon Class

An active balloon C++ class `CBalloon` has been developed. The class is inherited from the active net class explained in the previous section and therefore have the same public member functions. The balloon is initialized when an instance of the class is constructed. An iteration of the balloon is performed when the member function `MinizeEnergy` is called. If an error occurs in any of the functions in the class a `CImgExc` exception is thrown.

#### Source

The source files are:

- `h_balloon.h`
- `h_balloon.cpp`
- `actnet.cpp`

#### Public Member Functions

The only difference of the public member functions from the active nets is the constructor that takes an additional parameter the blowforce  $\gamma$ .

```

CBalloon(const CPoint &UL, const CPoint &LR, const int &nr,
         const int &nc, CImgByte * inner, CImgByte * outer,
         double alpha, double beta, double omega,
         double rho, int prob, double blowforce,
         CImgLog * Log = NULL);

```

Constructor. The arguments are the upper left corner and lower right corner of the initial position of the balloon, the number of vertical and horizontal nodes, the image used for calculating the energies of the inner nodes and the image used for calculating the energies of the outer nodes. The remaining parameters are explained in section 6.2.

## Example

The example from the active net can be used directly with the balloon.

### E.11.3 The Active Contour Class

An active contour C++ class `CAContour` has been developed. The class contains all information of the contour. The contour is initialized when an instance of the class is constructed. An iteration of the contour is performed when the member function `MinimizeEnergy` is called. If an error occurs in any of the functions in the class a `CImgExc` exception is thrown.

#### Source

The source files are:

- `h_actcont.h`
- `h_actcont.cpp`
- `actnet.cpp`

#### Public Member Functions

```
CAContour(const CPoint &center, const int& radius,  
          const int &np, CImgByte * inner,  
          double alpha, double beta, double omega,  
          double rho, int prob, double blowforce,  
          CImgLog * Log = NULL);
```

Constructor. The arguments are the center of the contour, the radius of the initial positions of the nodes, the number of nodes and the image used for calculating the energies of the nodes. The remaining parameters are explained in section 6.3.

```
virtual void ShowNet(CImgByte &img, const int &mark);
```

Shows the contour on the input image with the given color.

```
double OuterBoundaryLength();
```

Calculates the arclength of the contour.

```
int MinimizeEnergy();
```

Performs one iteration of the minimization of the energy of the contour. If no change in energy is noted the result is (0) else it is (1).

## Example

The example from the active net can be used directly with the contour.

# Bibliography

- [1] F. Cosman B. Herrington S. Himmelstein R. Lindsay. Radiographic absorptiometry: a simple method for determination of bone mass. *Osteoporosis Int.*, 2:34–38, 1991.
- [2] T. H. Cormen C. E. Leiserson R. L. Rivest. *Introduction to Algorithms*. The MIT Press, McGraw-Hill Book Company, 1980.
- [3] G. Christiansen E. Both P. Ø. Sørensen. *Mekanik*. Laboratoriet for Teknisk Fysik, Danmarks Tekniske Højskole, 1990.
- [4] Yang Chen Gérard Medioni. Description of complex objects from multiple range images using an inflating balloon model. Technical report, ?, ?
- [5] H. E. Meeama H. Meindok. Advantages of peripheral radiogrammetry over dual-photon absorptiometry of the spine in the assesment of prevalence of osteoporotic vertebral fractures in women. *Journal of Bone Mineral Research*, 7:897–903, 1992.
- [6] H. W. Wahner I. Fogelman. *The evaluation of osteoporosis: Dual energy X-ray absorptiometry in clinical practice*. Martin Dunitz, 1994.
- [7] P. E. Frandsen K. Jonasson O. Tingleff. *Unconstrained Optimization*. Institute of Mathematical Modelling (IMM), Technical University of Denmark, 1997.
- [8] K. M. Fox K. Powell-Threets C. C. Plato. Radial and ulnar cortical thickness of the second metacarpal. *Journal of Bone Mineral Research*, 10:1930–1934, 1995.
- [9] C. C. Johnston Jr. L. Joseph Melton III. Bone densitometry. In B. Lawrence Riggs L. Joseph Melton III, editor, *Osteoporosis. Etiology, Diagnosis, and Management*, chapter 12, pages 275–297. Lippincott-Raven, 1995.
- [10] T. Derisquebourg P. Dubois J. P. Devogelaer. Automated computerized radiogrammetry of the second metacarpal and its correlation with absorptiometry of the forearm and the spine. *Calcif Tissue Int*, 54:461–465, 1994.
- [11] M. Fukunaga T. Tomomitsu N. Otsuka H. Imai R. Morita Y. Nishii. Indexes of bone mineral content on second metacarpal bone roentgenogram analyzed by digital image processing: A comparison with other bone mass quantifying methods. *Radiat Med*, 8:230–235, 1990.

- [12] P. W. Karlsson V. L. Hansen. *Matematisk Analyse 2: Funktioner af flere reelle variable*. Matematisk Institut, Danmarks Tekniske Højskole, Lyngby., 2 edition, 1993.
- [13] M. Bro-Nielsen. Active nets and cubes. Technical Report 13, Institute of Mathematical Modelling, Technical University of Denmark, 1994.
- [14] M. Bro-Nielsen. Modelling elasticity in solids using active cubes. Technical Report 14, Institute of Mathematical Modelling, Technical University of Denmark, 1994.
- [15] H. Brockstedt. *Cortical bone structure and remodeling*. PhD thesis, Aarhus Bone and Mineral Research Group, University Department of Endocrinology and Metabolism and University Department of Pathology, Aarhus Amtssygehus, Denmark, ?
- [16] J. M. Carstensen. Indledende billedbehandling, note 3, 1996. IMM, DTU.
- [17] K. Conradsen. *En introduktion til statistik, bind 2B*. IMSOR, Danmarks Tekniske Højskole, 4 edition, 1984.
- [18] K. Conradsen. *En introduktion til statistik, bind 1B*. IMM,DTU, 6 edition, 1995.
- [19] D. W. Dempster. Bone remodeling. In B. Lawrence Riggs L. Joseph Melton III, editor, *Osteoporosis. Etiology, Diagnosis, and Management*, chapter 3, pages 67–91. Lippincott-Raven, 1995.
- [20] Imation. *Imation Trimax FM Film, Technical Information Sheet*.
- [21] The Bone Measurement Institute. An overview of bone mass measurements technology, 1996.
- [22] J.A. Kanis. *Textbook of Osteoporosis*. Blackwell Science, 1996.
- [23] V. Hlavac R. Boyle M. Sonka. *Image Processing, Analysis and Machine Vision*. Chapman and Hall, 1993.
- [24] H. E. Meeama. Radiographically detectable intracortical porosity, the dimensions and frequencies of its components in hand bones of normal men and women. *Acta Radiologica Diagnosis*, 27:165–172, 1986.
- [25] H. E. Meeama. Radiologic study of endosteal, intracortical, and periosteal surfaces of hand bones in metabolic bone diseases. *Hand Clinics*, 7:37–51, 1991.
- [26] L. Mosekilde. *Knoglevævets biologi. Fysiologiske, kliniske og farmakologiske aspekter af relationerne mellem struktur og funktion*. Ciba-Geigy A/S, 1988.
- [27] W. Niblack. *An Introduction to Digital Image Processing*. Prentice-Hall, 1986.
- [28] U. Olesen. Segmentation of hand x-rays. Master's thesis, Department of Mathematical Modelling, Technical University of Denmark, July 1998.

- [29] A. M. Parfitt. Morphologic basis of bone mineral measurements: Transient and steady state effects of treatment in osteoporosis. *Mineral Electrolyte Metab.*, 4:273–287, 1980.
- [30] T. Pavlidis. *Algorithms for Graphics and Image Processing*. Springer-Verlag, 1982.
- [31] K. Petersen. Analysis of dental radiographs. Master's thesis, Department of Mathematical Modelling, Technical University of Denmark, July 1997.
- [32] W. T. Vetterling B. P. Flannery W. H. Press, S. A. Teukolsky. *Numerical Recipes in C. The art of Scientific Computing. Second Edition*. Cambridge university press, 1992.